IMPERIAL COLLEGE LONDON

EFFICIENT NUMERICAL MODELLING OF THE ULTRASONIC SCATTERING FROM COMPLEX SURFACE-BREAKING DEFECTS

by

Richard Andrew Phillips

A thesis submitted to Imperial College London for the degree of

Doctor of Engineering

Department of Mechanical Engineering

Imperial College London

London SW7 2BX

February 2019

‘Essentially, all models are wrong, but some are useful.’

George Box

Declaration

I herewith certify that all material in this dissertation which is not my own work has been properly acknowledged.

Richard Andrew Phillips

Copyright Declaration

The copyright of this thesis rests with the author and is made available under a Creative Commons Attribution Non-Commercial No Derivatives licence. Researchers are free to copy, distribute or transmit the thesis on the condition that they attribute it, that they do not use it for commercial purposes and that they do not alter, transform or build upon it. For any reuse or redistribution, researchers must make clear to others the licence terms of this work.

Abstract

Ultrasonic testing is routinely used in the nuclear power generation industry to assess the structural integrity of plant components. The regulatory nature of the industry means that ultrasonic inspection procedures require substantiation through experimental trials and semi-analytical simulation, which can be costly and time-consuming. Furthermore, due to the complex defect and component geometries that are commonly encountered in the industry, the generation of evidence that accurately represents real inspections can be challenging. Numerical modelling techniques offer an effective alternative for substantiating inspections as they can accurately simulate the ultrasonic scattering from complex geometries, yet such techniques lead to increased computational cost. Hybrid techniques, which combine both semi-analytical and numerical methods, offer an approach to rapidly simulate an entire ultrasonic inspection whilst maintaining the ability to simulate the scattering from complex defects. However, there is a lack of experimental validation for extant hybrid techniques, particularly for three-dimensional simulations, and they have not been widely applied to the simulation of surface-breaking defect inspections, which are commonly encountered in both manufacturing and in-service inspections.

This thesis has extended the functionality of a three dimensional hybrid technique to simulate the inspection of surface-breaking defects. Validation evidence demonstrates that the hybrid model accurately predicts the ultrasonic scattering from a well-characterised reflector. An arbitrary transduction system has been incorporated to the model, enabling the model to be more broadly applied to the simulation of ultrasonic inspections of plant components. Furthermore, validation on a real defect provides a high level of confidence that the model can be used to assess and quantify the performance of inspections where qualification becomes challenging. This work has made a clear step forward in the use of simulation for inspection qualification and further work is required to fully optimise the simulation methodology.

Acknowledgment

I would like to express thanks to my supervisors Prof. Mike Lowe, Dr Peter Huthwaite and Dr Dave Duxbury. Thank you for being patient and for providing clear and thorough advice throughout my project.

I am grateful to the Engineering and Physical Research Sciences Council, the UK Research Centre for Non-Destructive Evaluation and the Ministry of Defence for their financial support for this project.

I would like to thank the members of the NDE group at Imperial College for many interesting and informative discussions, both in the lab and at the local, and for helping me get up to speed with ultrasonic modelling. I am grateful to all the people I have worked with at Rolls-Royce Submarines. In particular, I would like to acknowledge Mike, Misty, Josh, Chris G and Chris R for putting up with my constant questioning and for creating a great environment to work in. I would also like to thank the EngD 2013 cohort and all my friends in Derby for creating great memories over the last 5 years.

Finally, I would like to thank my family for their continued support, patience and encouragement during my doctorate. I would like to give special thanks to Laura; her support and dedication throughout my EngD has been invaluable.

Contents

1 Introduction **16**

1.1 Industrial Context 16

1.2 Personal Context 18

1.3 Thesis Structure 19

2 Ultrasonic Testing & Inspection Modelling **21**

2.1 Introduction 21

2.2 Ultrasonic Inspection of Surface-breaking Defects 24

2.2.1 Angled Shear Wave Inspection 25

2.2.2 Time of Flight Diffraction 29

2.2.3 Longitudinal Creeping Wave Inspection 32

2.2.4 Ultrasonic Array Inspections 34

2.2.5 Summary 36

2.3 Semi-Analytical Models 36

2.3.1 Born Approximation 37

2.3.2 Kirchhoff Approximation 39

2.3.3 Extended Methods for Surface-Breaking Defects 41

2.3.4 Summary 43

2.4 Numerical Models 43

2.4.1 Finite Difference 44

2.4.2 Finite Volume 46

2.4.3 Boundary Element Method 46

2.4.4 Finite Elements 47

2.4.5 Summary 51

2.5 Hybrid Methods 51

2.5.1 CIVA Athena 52

2.5.2 Finite Element Local Scattering . . . 52
2.5.3 Generic Domain-Linking Scheme . . . 54
2.5.4 Summary . . . 57

3 Ultrasonic Beam Model 58
3.1 Introduction . . . 58
3.2 Huygens-Fresnel Beam Model . . . 59
3.3 Finite Element Point Source Simulation . . . 61
3.3.1 Shear Wave Point Source . . . 62
3.3.2 Results . . . 65
3.3.3 Discussion . . . 67
3.3.4 Longitudinal Wave Point Source . . . 69
3.4 Beam Model Validation . . . 70
3.4.1 Normal Incidence Longitudinal Wave . . . 71
3.4.2 Normal Incidence Shear Wave . . . 74
3.4.3 Angled Incidence Shear Wave . . . 78
3.5 Conclusions . . . 80

4 A Hybrid Method for Surface-Breaking Defects 82
4.1 Introduction . . . 82
4.2 Hybrid Model Methodology . . . 83
4.2.1 Defect Domain . . . 83
4.2.2 Backward Process . . . 84
4.3 Numerical Verification . . . 87
4.3.1 Smooth Notch . . . 89
4.3.2 Rough Notch . . . 91
4.4 Experimental Validation . . . 92
4.4.1 Experiment . . . 92
4.4.2 Hybrid Simulation . . . 93
4.4.3 Discussion . . . 96
4.5 Attenuation due to Roughness . . . 99
4.5.1 Results and Discussion . . . 101
4.6 Conclusions . . . 102

5 Simulating the Ultrasonic Response from a Thermal Fatigue Defect 104

5.1 Introduction 104

5.2 Experimental Data Collection 106

5.3 XCT Imaging and Mesh Generation 109

5.3.1 XCT Imaging 109

5.3.2 Image Segmentation 111

5.3.3 Mesh Generation 115

5.4 Hybrid Simulation 120

5.5 Results and Discussion 123

5.6 Influence of Tip Shape 128

5.6.1 Simulation Methodology 129

5.6.2 Results and Discussion 132

5.7 Conclusions 134

6 Conclusions 136

6.1 Summary 136

6.2 Further Work 139

References 141

List of Figures

2.1 A wire-frame sketch of a pipe section containing a surface-breaking defect located on the inner diameter. A typical angled beam ultrasonic inspection technique is also illustrated. 25

2.2 A plane longitudinal wave at oblique incidence on an infinite planar boundary between two materials. The direction of each transmitted and reflected wave type is shown by an arrow and the boundary normal is shown using a dashed line. Reflected Shear (RS), Reflected Longitudinal (RL), Transmitted Shear (TS) and Transmitted Longitudinal (TL) waves are labeled on the figure. 26

2.3 Schematic of the corner echo scattering from a surface-breaking defect. 27

2.4 A polar plot of the coefficient of reflection of longitudinal and shear waves from a 90° corner. The incident angle is varied between 0° and 90°. 28

2.5 For a ray normally incident on a diffracting edge, a circle of diffracted rays are produced in the plane of the incident ray. 30

2.6 A typical ToFD inspection setup. 30

2.7 The amplitude of a compression wave mode diffracted signal due to an incident compression wave over a range of incident angles. The angle of diffraction is equal to the incident angle. 31

2.8 Generation of longitudinal creeping waves. 33

2.9 Inner surface-breaking defect detection with secondary creeping waves and the 30-70-70 path. 34

2.10 Illustration of the tangential plane approximation. 40

2.11 Achenbach and Norris modelled a surface-breaking defect as an isolated defect by extending the defect and ray paths symmetrically about the backwall. 42

2.12 A diagram which shows the calculation of an exact derivative and the approximations used in the finite difference scheme 44
2.13 An illustration of (a) a pulse echo ultrasonic inspection setup and (b) the hybrid methodology used to simulate the inspection. 55

3.1 Schematic of the Huygens-Fresnel beam model setup for a wedge-mounted transduction system. 60
3.2 Far field radiation patterns for various types of 2D FE sources. 62
3.3 An approximate 3D shear wave point source for an FE model. 8 neighboring nodes are excited in a torsional manner to generate a spherically expanding polarised shear wave. 63
3.4 A schematic of the three monitoring circles used to measured the field radiated from the point source. The legend describes which Cartesian axis plane the monitoring circles are parallel to. 64
3.5 Polar plots of the results obtained from the monitoring circles in each orthogonal plane. (a) shows the normalised shear wave amplitude, (b) the compression wave amplitude normalised to the shear wave and (c) the time of flight error for the shear wave where the radial axis has units of nanoseconds. 65
3.6 A projection of the shear wave point source in the (a) $x-y$, (b) $x-z$ and (c) $y-z$ planes along with the definition of the angle θ used in figure 3.5. 66
3.7 A plot of the shear wave amplitude measured on the monitoring rings in the $x-y$ and $x-z$ planes and the $|\sin\theta|$ function. 68
3.8 An approximate 3D longitudinal wave point source for an FE model. 8 neighboring nodes are excited in a radial manner to generate a spherically longitudinal wave. 70
3.9 Polar plots of the results obtained from the monitoring circles in each orthogonal plane. (a) shows the normalised longitudinal wave amplitude and (b) shows the residual amplitude relative to the longtudinal wave. 71
3.10 2D schematic of the 3D model setup for the validation of the beam model against CIVA for simulating a normal incidence longitudinal wave. 71

3.11 Beam profile measured at the receiver plane in (a) CIVA and (b) the Huygens model. The x_0 and z_0 lines to compare the echodynamic profile of the beams are marked in (b). 72
3.12 The echodynamic profiles of the normal incidence longitudinal wave along the (a) z_0 and (b) x_0 lines measure by the Huygens model and CIVA. 72
3.13 2D schematic of the 3D model setup for the validation of the source to defect domain linkage against the Huygens model for simulating a normal incidence longitudinal wave. 73
3.14 Beam profile measured at the receiver plane by (a) the Huygens model and (b) in the FE model. The x_0 and z_0 lines to compare the echodynamic profile of the beams are marked in (b). 74
3.15 The echodynamic profiles of the normal incidence longitudinal wave along the (a) z_0 and (b) x_0 lines measured by the Huygens model (solid blue) and the FE model (broken red). 75
3.16 Schematic of the modelling process used to validate the forward process for the hybrid technique. 76
3.17 Images of the maximum amplitude of the incident wave recorded at the receiver plane. (a) is calculated directly by the Huygens beam model and (b) is measured from the FE model by exciting a plane of shear wave point sources. The white lines in (b) show the locations of the echodynamic curve measurements in figure 3.18. 76
3.18 Echodynamic curves of the incident wave field measured parallel to the x-axis (a) and y-axis (b). The results from the Huygens model are plotted in both, along with the results measured from the FE model in figure 3.16 for a range of source plane angles. 77
3.19 Offset of location of maximum of incident wavefield. 77
3.20 2D schematic of the 3D model setup for the validation of the source to defect domain linkage against CIVA for simulating an angled incidence shear wave. 78
3.21 Beam profile measured at the receiver plane by CIVA (a) and in the FE model (b). 79

3.22 Echodynamic profiles of the incident beam excited in the FE (blue) and CIVA (red) models. (a) is measured at the location of the maximum in the x-axis and (b) is measured at the location of the maximum in the z-axis. 80

4.1 Schematic of the corner echo scattering from a surface-breaking defect. 84
4.2 A truncated backwall is combined with the defect into a single scatterer. The hybrid monitoring surface encloses the scatterer within the defect domain. 85
4.3 The hybrid monitoring surface is reduced to a single edge. 87
4.4 Schematic of the numerical validation model including an illustration of the monitoring surface used for the hybrid calculation. 88
4.5 A comparison of (a) the recorded time history from each model and (b) the waveform of the scattered wave. 90
4.6 A comparison of the scattered wave from the rough defect predicted by each model. 91
4.7 Schematic diagram of the setup used to collect experimental data. The out-of-plane extent of the defect is 3 mm 93
4.8 B-scan image formed from the experimental data. 94
4.9 Schematic of the defect domain FE model used to simulate the shear wave reflection from the surface-breaking defect. Note the change in z-axis direction in comparison to figures 4.7 and 4.10 94
4.10 Schematic diagram of the hybrid method to link the defect domain FE model with the wedge model. 95
4.11 The B-scan image generated by the hybrid simulation is shown in (a). The scattering mechanisms of the distinct features on the image have been labelled. The experimental B-scan image has been repeated in (b) for comparison to (a) 97
4.12 An illustration of the tip diffraction and 'half-skip' tip diffraction, where the diffracted waves reflect from the backwall and are measured by the transducer. 98
4.13 Schematic of the hybrid method to simulate the ultrasonic scattering from a surface-breaking defect with a rough surface. 100

4.14 Attenuation of scattered wave from a surface-breaking defect with increasing roughness calculated with the hybrid model (blue) and the Kirchhoff approximation (red). 101

5.1 Stitched optical microscope images of the defect profile on the surface. No scale is provided on the images however the surface length of the defect is approximately 15.5 mm. 106
5.2 A schematic of the inspection setup. The test piece thickness is also given. 107
5.3 A schematic of the ultrasonic array scan path along the length of the defect. The test piece dimensions are also given. 108
5.4 Photograph of the experimental setup used to capture the ultrasonic data. The array is coupled with water to the test piece and a manipulator is used to scan the array across the length of the defect. 108
5.5 Illustration of a B-scan inspection using an array transducer; the aperture is moved electronically across the array elements to perform the scan. 109
5.6 Schematic of the XCT setup. 110
5.7 Photograph of the CT coupon made from sectioning the test piece. . 111
5.8 An example of the filters applied to the image reconstructed by the CT process. The segmentation was performed by dividing the image into smaller regions. 112
5.9 Images of the reconstructed defect morphology after segmentation from two different viewing angles. 113
5.10 A snapshot of the resulting FE mesh of the thermal fatigue defect. Visualised in ABAQUS CAE. 116
5.11 Images of the elements that lie on the boundary of the mesh generated by (a) the FE Grid algorithm where the adjacent hypotenuses are perpendicular and (b) the custom mesh appending algorithm where the adjacent hypotenuses are parallel. 117
5.12 A 2D schematic of the 3D model used to measure the reflection from the crossed hypotenuses. The out-of-plane dimension is also 16 λ and the source point depicted in the figure is located in the centre of the x-y plane of the model. 118

5.13 An image of (a) a solid model with only the exterior element boundaries showing and (b) a wire-frame model which shows the crossed hypotenuses on the tetrahedral elements. Images taken in ABAQUS CAE. 119
5.14 An uncorrected B-scan image of the displacement-time histories recorded at along a line of monitor nodes. The line of nodes are parallel to the x-axis and are located at the centre of the monitoring surface. 119
5.15 A 2D schematic of the 3D hybrid model procedure for simulating the inspection of a surface-breaking defect. 121
5.16 A schematic of the defect domain for the hybrid simulation. 122
5.17 Images (a) and (b) show an Alicona optical microscope measurement of two distinct features on the defect to the boundary of the coupon and (c) shows the corresponding locations on the defect mesh, taken from ABAQUS CAE. 122
5.18 The 45° shear wave B-scan generated from the experimental FMC data. The sub-aperture size is 10 elements and no focusing was applied. In addition to the corner trap, two distinct features have been labelled on the image. 124
5.19 A Schematic of the generation of a B-scan image. (a) shows the origin of the corner trap indication and the tip diffraction indication as a transducer is scanned over the defect in a line scan. (b) depicts the effect of the beam width on the B-scan image and shows that signals scattered from complex defect features may be mis-plotted. 125
5.20 The B-scan image generated by the hybrid simulation is shown in (a). The experimental B-scan image has been repeated in (b) for comparison to (a) 126
5.21 A Schematic of the 2D FE model for measuring the diffracted signal from a closed crack tip. 129
5.22 A Schematic of the 2D FE model for measuring the diffracted signal from a rounded notch tip. 130
5.23 The back-diffracted wave amplitude relative to a 3 mm SDH for (a) an incident longitudinal wave and (b) an incident shear wave. In the legend, r refers to the radius of the semi-circular tip of of the notch in the FE simulations. 132

Chapter 1

Introduction

This thesis presents the development and validation of a simulation technique using numerical-based modelling for the ultrasonic inspection of components containing complex surface-breaking defects. The inspection qualification process in the nuclear sector requires that the performance of ultrasonic inspections carried out on safety critical components is substantiated by various methods, including experimental validation and semi-analytical modelling. As set out below, these methods have significant limitations, in particular in relation to complex defects. The work in this thesis sets out to provide a reliable and accurate basis for simulations that will address these limitations and thus improve the inspection qualification process.

1.1 Industrial Context

Non-Destructive Evaluation (NDE) techniques provide a means to assess the structural integrity of a component without causing damage. This capability is paramount across the engineering sector and failure to perform such assessments to a high degree of accuracy can lead to catastrophic consequences, such as large financial losses and a risk to public safety. Many NDE techniques exist for a wide range of applications, each with their own advantages and limitations; a full review of available NDE techniques can be found in the literature, for example [1].

In the nuclear power generation industry, a key NDE technique is ultrasonic testing (UT). UT is a cost-effective and versatile NDE technique that provides the ability to inspect the full volume of a component. It is often used to assess the structural integrity of Nuclear Steam Raising Plant (NSRP) components both during

manufacture and throughout operational life. Due to the regulatory requirements of the industry, an inspection applied to an NSRP component is subject to a rigorous qualification procedure.

Historically, the performance of an NDE technique is demonstrated by providing an evidence based justification, which is often formed using data generated by experimental trials and previous inspection experience [2]. However, the generation of evidence that truthfully represents the performance of the NDE inspection is challenging; the morphology of cracks and defects that have been found within NSRP components are often complex, exhibiting significant levels of surface roughness and branching or connected to irregular component geometries [3]. Although methods exist for the reproduction of credible plant defects to assess inspection performance [4], the range of available methods is limited and each have significant drawbacks. For example, manufacturing defects, such as welding defects, can be reproduced through weld doping or weld modification [4], yet there is poor control over the characteristics of the induced defects therefore impacting the accuracy of this process. For service-induced defects, such as fatigue cracking, it is possible to recreate the fatiguing process in a controlled environment [5], however this process can be time-consuming, expensive and complications arise when considering complex component geometry. Inspection performance is therefore commonly justified using simple artificial defects [6]. To account for defect complexities, reporting thresholds are often made overly-sensitive and inspection redundancy is increased, resulting in a decrease in the efficiency and cost-effectiveness of NDE inspections.

Semi-analytical modelling offers an efficient alternative to experimental data collection and enables the simulation of inspection scenarios that are not possible through experiment. Models that have previously been employed in the nuclear sector include the Geometrical Theory of Diffraction (GTD) [7] and the Kirchhoff Approximation (KA) [8]. These semi-analytical methods are advantageous because they are computationally efficient and have a history of validation. However, the broad physical assumptions used in the models mean that they are limited to predicting the ultrasonic interaction from defects with low levels of complexity [9]; semi-analytical methods therefore provide little advantage over experimental trials when considering complex defects.

Numerical-based modelling techniques provide the ability to accurately calculate the ultrasonic scattering from complex structures [10]. For example, the Finite

Element Method (FEM) has recently been used to improve current understanding of the effect of defect roughness on the ultrasonic response [11]. However, the spatial discretisation required by numerical methods combined with the size of components in the nuclear sector often leads to excessive and infeasible computational memory requirements, especially in three dimensions (3D). Alternatively, hybrid techniques [12–14] combine both semi-analytical and numerical methods offering an approach to rapidly simulate an entire ultrasonic inspection, whilst also providing the capability to simulate the ultrasonic scattering from complex defects.

Despite the great potential of hybrid methods, they have not been widely applied to simulate the ultrasonic scattering from surface breaking defects and there is limited validation of these techniques for simulating the ultrasonic scattering from complex defects in 3D.

1.2 Personal Context

The author began the Engineering Doctorate (EngD) in 2013 during the completion stages of a programme of research between Imperial College and several stakeholder companies, including Rolls-Royce Submarines, entitled "Modelling of Ultrasonic Response from Rough Defects". The Engineering and Physical Sciences Research Council (EPSRC) grant number for this project is EP/I018948/1. The programme focused on the development and utilisation of modelling techniques to improve understanding of the ultrasonic scattering from rough surfaces. The benefits of an efficient numerical modelling procedure became evident through this research, however, it only focused on defects that are embedded within the parent material. The capability of the model would not be fully comprehensive without the consideration of surface-breaking defects, as such defects are regularly anticipated throughout NDE inspections on NSRP components.

As is typical for the EngD scheme, the author spent the first 15 months in the NDE Group at Imperial College London before moving the NDE Research department at Rolls-Royce Submarines. The author has been responsible for the development and validation of the model to expand its application to surface breaking defects and to fully account for a generic ultrasonic transduction system. The technology developed by the author has been delivered in accordance with the Rolls-Royce engineering governance, such as the achievement of the Technology Readiness

Level (TRL) 4. On completion of this EngD, the author became a full-time member of the NDE research team at Rolls-Royce aiding in the continued development of this technology such that it can be deployed and fully utilised for the qualification of the inspection of safety critical NSRP components.

The author was a leading member of the Rolls-Royce Engineering Doctorate Network, founded by previous EngD colleagues in 2012. The network's key goal is to increase the visibility of EngD research across all sectors of the company. This has been successfully achieved through the annual conference, now in its fifth iteration, which brings together industry specialists with researchers and academics to promote the impact of technology transfer and facilitate internal and external research collaboration. In addition, regular visits to world leading research centres across the UK are organised for Rolls-Royce sponsored EngD researchers, to both create a community within the company and to establish links to research centres. Finally, the author was the UK ambassador for industry-based research in the Rolls-Royce global research community by presenting at the Rolls-Royce PhD Asia conference held in Busan, South Korea, on behalf of the Engineering Doctorate Network.

1.3 Thesis Structure

Following the introduction to this thesis in chapter 1, chapter 2 presents a review of the theoretical background and literature on ultrasonic testing and inspection modelling relevant to the inspection of surface-breaking defects. The review considers commonly employed ultrasonic inspection techniques, semi-analytical models historically used in the nuclear sector and various numerical and emergent hybrid methods that enable the scattering from complex shapes to be calculated.

Following the review, chapter 3 investigates the use of Huygens' principle as a means to couple a semi-analytical model of an ultrasonic transduction system with a localised 3D FE model of the defect. Both longitudinal and shear wave modes are considered in the investigation and the method is compared to the commercially available software CIVA (EXTENDE, France). Chapter 4 then discusses the methodology developed for simulating the inspection of surface breaking defects using a 3D hybrid modelling technique. The validity of this approach is measured by comparison to a full numerical model for simple and complex defect geometries and by comparison to experiment for a simple defect geometry. In this chapter, a Monte

Carlo study is carried out using the hybrid technique to investigate the ultrasonic attenuation due to increasing roughness on surface-breaking defects.

In chapter 5, further experimental validation of the hybrid technique is presented through the simulation of an ultrasonic inspection of a thermal fatigue defect, where X-ray computed tomography is employed to obtain an accurate representation of the true defect morphology. The chapter concludes with a study into the influence of crack tip shape on the back-scattered diffracted ultrasound by comparing the diffraction from a sharp crack to that from an artificial reflector commonly employed for inspection qualification. Finally, the conclusions of the thesis are drawn together in chapter 6.

Chapter 2

Ultrasonic Testing & Inspection Modelling

To suitably report on the modelling of the ultrasonic inspection of components containing surface-breaking defects, consideration is first given to ultrasonic inspection techniques used within industry and the theoretical foundations of the inspection models. This chapter includes a review of common inspection techniques employed for the detection and characterisation of surface-breaking defects. In the following sections, the methods of simulation of the propagation and scattering of ultrasonic waves in elastic media are reviewed, with focus on the simulation techniques commonly employed within the nuclear power generation industry. Firstly, the mathematical foundations of elastic wave propagation are summarized.

2.1 Introduction

The formulation of elastic wave propagation is well documented, as in [15, 16]. Here, the fundamental mathematical relations necessary for a complete description of linear elastic bulk wave propagation are summarised. The formulation of wave propagation begins by considering Newton's second law in terms of particle displacement and material stress, which leads to the following equation of motion:

$$\rho \frac{\partial^2 u_i}{\partial t^2} = \frac{\partial \sigma_{ij}}{\partial x_j} \tag{2.1}$$

where u_i is the component of particle displacement in the direction x_i, ρ is material density and σ_{ij} is the stress tensor; indicial notation is employed here. Hooke's law can be used to relate the stress of an isotropic material to the strain, ϵ:

$$\sigma_{ij} = \lambda \delta_{ij} \epsilon_{kk} + 2\mu \epsilon_{ij} \tag{2.2}$$

where δ_{ij} is the Kronecker delta and λ and μ are the Lamé constants. The strain is given by:

$$\epsilon_{ij} = \frac{1}{2}\left(\frac{\partial u_i}{\partial x_j} + \frac{\partial u_j}{\partial x_i}\right) \tag{2.3}$$

From (2.1), (2.2) and (2.3) the Navier governing equation can be derived and is given in vectorial form by:

$$\rho \frac{\partial^2 \boldsymbol{u}}{\partial t^2} = (\lambda + \mu)\nabla(\nabla \cdot \boldsymbol{u}) + \mu \nabla^2 \boldsymbol{u} \tag{2.4}$$

Solutions to the Navier governing equation describe the propagation of disturbances in isotropic elastic media in the absence of external forces. The Navier governing equation can be simplified by utilising the Helmholtz decomposition, which enables the particle displacement vector to be expressed in terms of an irrotational scalar field, ϕ, and solenoidal vector field, $\boldsymbol{\psi}$:

$$\boldsymbol{u} = \nabla \phi + \nabla \times \boldsymbol{\psi} \tag{2.5}$$

The terms ϕ and $\boldsymbol{\psi}$ are often referred to as the wave potentials; whilst ϕ is a scalar and therefore describes only magnitude, the vector field $\boldsymbol{\psi}$ describes the propagation of disturbances whose oscillation can be polarised in the three orthogonal directions.

By combining equations (2.4) and (2.5), the resulting equation is reached:

$$\nabla\left[(\lambda + 2\mu)\nabla^2 \phi - \rho \frac{\partial^2 \phi}{\partial t^2}\right] + \nabla \times \left[\mu \nabla^2 \boldsymbol{\psi} - \rho \frac{\partial^2 \boldsymbol{\psi}}{\partial t^2}\right] = 0 \tag{2.6}$$

For the left hand side of equation (2.6) to remain consistent with the right hand side, the terms in the brackets on the left hand side must vanish. This leads to the equations:

$$\nabla^2 \phi = \frac{1}{c_L^2} \frac{\partial^2 \phi}{\partial t^2} \tag{2.7}$$

$$\nabla^2 \boldsymbol{\psi} = \frac{1}{c_T^2} \frac{\partial^2 \boldsymbol{\psi}}{\partial t^2} \tag{2.8}$$

where the longitudinal wave mode velocity, c_L, is given by the equation:

$$c_L^2 = \frac{\lambda + 2\mu}{\rho} \tag{2.9}$$

and the transverse wave mode velocity, c_T, is given by the equation:

$$c_T^2 = \frac{\mu}{\rho} \tag{2.10}$$

Equation (2.4) has been decomposed using the Helmholtz decomposition into two independent wave equations. By assuming that particle motion is irrotational, i.e. $\boldsymbol{u} = \nabla\phi$, equation (2.6) and (2.7) lead to:

$$\nabla^2 \boldsymbol{u} = \frac{1}{c_L^2} \frac{\partial^2 \boldsymbol{u}}{\partial t^2} \tag{2.11}$$

which is the wave equation governing the propagation of longitudinal wave motion only. Similarly, by assuming that particle motion is purely solenoidal, $\boldsymbol{u} = \nabla \times \boldsymbol{\psi}$, the wave equation governing transverse (shear) wave motion is obtained:

$$\nabla^2 \boldsymbol{u} = \frac{1}{c_T^2} \frac{\partial^2 \boldsymbol{u}}{\partial t^2} \tag{2.12}$$

As equations (2.11) and (2.12) are independent, the wave modes they describe will propagate independently of each other in unbounded elastic media.

The solution to equations (2.11) and (2.12) for the propagation of plane harmonic longitudinal and shear waves in linear elastic media, are given by:

$$\boldsymbol{u}_\alpha = A e^{i(k_\alpha \boldsymbol{r} - \omega t)} \tag{2.13}$$

where $\alpha = L, T$ for longitudinal or transverse (shear) wave modes respectively, A is the displacement amplitude, $k_\alpha = \frac{2\pi}{\lambda_\alpha}$ is the associated wavenumber, λ_α is the associated wavelength, $\omega = 2\pi f$ is the angular frequency, f is the frequency of oscillation and the vector $\boldsymbol{r} = (x, y, z)$. These solutions describe planes of infinite extent with constant phase propagating through space and are commonly used to decrease the complexity of the analysis.

Although equations (2.11) and (2.12) are formulated in the time-domain, in general, analytical scattering models are formulated in the frequency-domain. The time-harmonic form of the wave equation is known as the Helmholtz equation. Considering only longitudinal motion, the source-free Helmholtz equation is written:

$$(\nabla^2 + k_L^2)\phi = 0 \tag{2.14}$$

Equation (2.14) governs the propagation of monochromatic waves and any solution to the Helmholtz equation will naturally be a solution to the wave equation.

2.2 Ultrasonic Inspection of Surface-breaking Defects

Surface-breaking defects occur through many different mechanisms. For example, in the manufacture of an engineering component, such defects can occur from incomplete weld penetration or cracking along the weld centreline due to shrinkage [3, 17]. Throughout the service life of the component, surface-breaking defects may also occur as a result of fatigue, caused by thermal and mechanical stresses [18], or from environmentally assisted cracking [19]. Regardless of the cause, stresses on pressure-containing components are often most severe at the surface [20] meaning that surface-breaking defects are particularly prone to growth and their detection is crucial.

The inspection technique chosen for the detection of surface-breaking defects is ultimately dependent upon the access to the component surface. With direct access to the surface that the defect is connected to, a variety of surface-based NDE techniques are available, such as visual inspection, dye penetrant inspection, or eddy current inspection [1]. However, there is often restricted access to this surface. For example, the anticipated defect is likely to be on the inside of a pipe or vessel where the stress is most severe, yet the inspection is often restricted to the outer exposed surface, as illustrated by figure 2.1. In this scenario, the defect is often referred to as an Inner Diameter (ID) surface-breaking defect or simply inner surface-breaking defect. This type of defect is the focus of the work presented here.

For the detection of inner surface-breaking defects, the aforementioned surface-

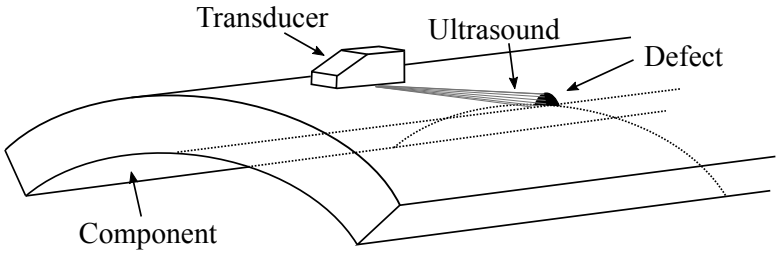


Figure 2.1: A wire-frame sketch of a pipe section containing a surface-breaking defect located on the inner diameter. A typical angled beam ultrasonic inspection technique is also illustrated.

based NDE techniques are no longer applicable and a volumetric technique is required. Radiography is a common volumetric method and holds significant advantages over other techniques, for example it does not require significant component preparation and provides a permanent record of the inspection. However, due to the inherent safety hazard, the use of radiography is heavily regulated, causing inspection to become time consuming and costly. Furthermore, crack-like defects, such as fatigue cracking, will cause little variation in component density unless aligned with the path of radiation and can therefore be difficult to detect. Ultrasonic methods, on the other hand, are more suited to the detection of crack-like defects and are not subject to the regulation and control of radioactive substances. The following subsections will review ultrasonic inspection techniques regularly used to detect and size inner surface-breaking defects.

2.2.1 Angled Shear Wave Inspection

Industry practice for the detection of inner surface-breaking defects is the angled shear wave pulse-echo (P-E) contact inspection [21], illustrated by figure 2.1. In this inspection, a shear wave is generated within the component by mode conversion of an incident longitudinal wave. The longitudinal wave is generated within a wedge, typically made from Perspex or Rexolite, and propagates at an angle to the normal of the component surface. At the interface between the wedge and the component, a proportion of the incident wave will be reflected, and some will be transmitted, undergoing refraction. Figure 2.2 illustrates the possible ray path combinations when a longitudinal wave is incident on an interface between two elastic media; at oblique incidence, mode conversion occurs resulting in the generation of multiple reflected and refracted waves, as shown in the figure.

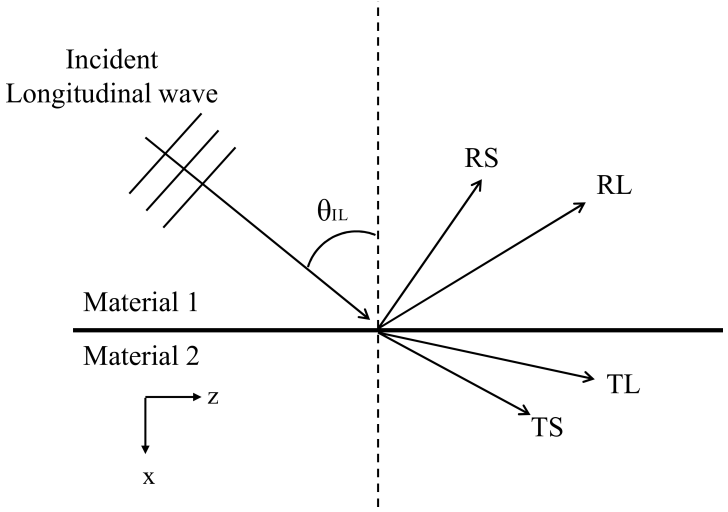


Figure 2.2: A plane longitudinal wave at oblique incidence on an infinite planar boundary between two materials. The direction of each transmitted and reflected wave type is shown by an arrow and the boundary normal is shown using a dashed line. Reflected Shear (RS), Reflected Longitudinal (RL), Transmitted Shear (TS) and Transmitted Longitudinal (TL) waves are labeled on the figure.

The direction of the reflected and refracted waves can be determined by the well known Snell's law. For a smooth interface, under the law of reflection an incident longitudinal wave propagating at θ_{IL} will generate a reflected longitudinal wave at an angle $\theta_{IL} = \theta_{RL}$. All other angles of reflection and refraction are given by Snell's law:

$$\frac{c_L^{(2)}}{sin(\theta_{TL})} = \frac{c_s^{(2)}}{sin(\theta_{TS})} = \frac{c_S^{(1)}}{sin(\theta_{RS})} = \frac{c_L^{(1)}}{sin(\theta_{IL})} \tag{2.15}$$

where $c_\beta^{(\alpha)}$ denotes the wave speed in material α for the wave mode β.

From equation 2.15 it can be observed that there are certain cases where θ_{TL} or θ_{TS} are 90°. These are known as critical angles. At the point where $\theta_{TL} = 90°$ all longitudinal wave energy is either reflected or mode converted into a surface wave [15]. This is commonly known as the first critical angle and can be calculated from the relation:

$$\theta_{crit,1} = sin^{-1}\left(\frac{c_L^{(1)}}{c_L^{(2)}}\right) \tag{2.16}$$

The second critical angle, where $\theta_{TS} = 90°$, can be calculated using the same approach. By selecting an incident angle greater than the first critical angle, only a single wave mode will propagate into the bulk of the component. This simplifies the analysis of the received scattered waves.

The angled shear wave technique is effective for detecting inner surface-breaking

defects because a strong reflection from the defect is achieved through the corner echo scattering mechanism, shown in figure 2.3. In this mechanism, an incident ultrasonic wave is reflected in the specular direction from both the crack face and the backwall. The magnitude of the waves reflected from this type of scattering can be determined by considering the appropriate reflection coefficients. For this analysis, the crack is assumed to be filled with a vacuum, however the consideration of other boundary conditions can be found in many reference texts, such as [22]. Under this assumption, no waves will be transmitted across the interface and the boundary conditions require the normal and tangential stress imparted by the incident wave on the interface to vanish; this type of interface is often referred to as a stress-free or free surface boundary. The coefficient of pressure of the reflected longitudinal wave due to an incident longitudinal wave is given by [23]:

$$\Gamma_{LL} = \frac{\gamma^2 \sin 2\theta_{RL} \sin 2\theta_{RS} - \cos^2 2\theta_{RS}}{\gamma^2 \sin 2\theta_{RL} \sin 2\theta_{RS} + \cos^2 2\theta_{RL}} \tag{2.17}$$

where $\gamma = C_S/C_L$. The reflection coefficient for the mode converted shear wave is given by:

$$\Gamma_{LS} = \frac{2\gamma^2 \sin 2\theta_{RL} \sin 2\theta_{RS}}{\gamma^2 \sin 2\theta_{RL} \sin 2\theta_{RS} + \cos^2 2\theta_{RL}} \tag{2.18}$$

For an incident shear wave, the equation for the reflection coefficient of a reflected shear wave is equal to that given by equation 2.17, such that $\Gamma_{SS} = \Gamma_{LL}$, however it should be noted that the values of θ_{RL} and θ_{RS} will not be the same for the two

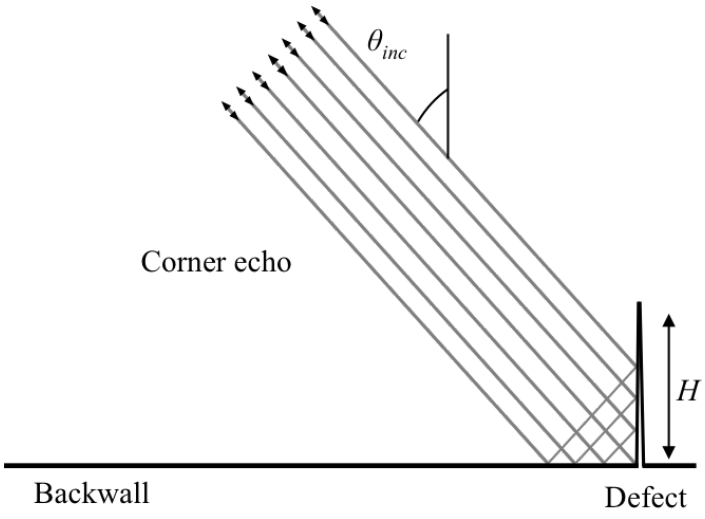


Figure 2.3: Schematic of the corner echo scattering from a surface-breaking defect.

cases. For the reflected longitudinal wave the coefficient is given by:

$$\Gamma_{SL} = \frac{-\sin 4\theta_{RS}}{\gamma^2 \sin 2\theta_{RL} \sin 2\theta_{RS} + \cos^2 2\theta_{RL}} \tag{2.19}$$

By assuming that the defect is smooth and perpendicular to the component backwall, from the law of reflection it can be determined that the angle of incidence on the second interface is equal to $90-\theta_{inc}$. Thus, the reflection coefficient of the corner echo can be calculated by the product of two reflection coefficients. For a longitudinal wave this is given by:

$$\Gamma_{CornerL} = \Gamma_{LL}(\theta_{inc})\Gamma_{LL}(90 - \theta_{inc}) \tag{2.20}$$

and similarly for an incident shear wave.

$$\Gamma_{CornerS} = \Gamma_{SS}(\theta_{inc})\Gamma_{SS}(90 - \theta_{inc}) \tag{2.21}$$

Both reflection coefficients are plotted in 2.4 for a defect contained within stainless steel (Youngs modulus: 200 GPa, density: 7800 $\mathrm{kg\,m^{-3}}$ and Poissons ratio: 0.3). It is clear from the figure that mode conversion strongly attenuates the longitudinal

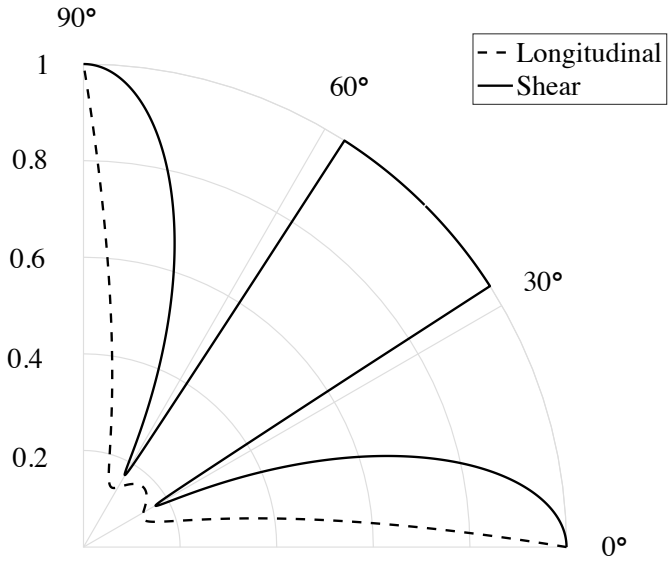


Figure 2.4: A polar plot of the coefficient of reflection of longitudinal and shear waves from a 90° corner. The incident angle is varied between 0° and 90°.

wave amplitude at oblique incidence. For shear wave incidence, however, total reflection is achieved for incident angles between approximately 32° and 58°, providing the optimal angular range for detection. Furthermore, the first critical angle for the wedge material Rexolite to a stainless steel boundary is around 24°, which is approximately equal to the incident angle required to generate a 32° incident shear wave. Therefore, within the optimal angular range for the corner echo, only a single incident wave mode will be generated in the material, simplifying the analysis of the recorded ultrasonic data. As a result, the angled incidence shear wave detection is the superior inspection technique for detecting inner surface-breaking defects.

2.2.2 Time of Flight Diffraction

When an ultrasonic wave is incident on a sharp discontinuity, such as the edge or tip of a defect, diffracted waves are generated [24]. For planar defects orientated perpendicular to the plane of incidence, the diffracted waves propagate away from the crack tip in a cylindrical manner, which in 2D can be thought of as a circle of diffracted rays as illustrated in figure 2.5. The Time of Flight Diffraction (ToFD) method is an ultrasonic inspection technique that utilities the diffraction phenomena [25–27].

As the name suggests, ToFD uses the transit time of the diffracted waves to provide information on a crack or defect, such as its location and size. A typical ToFD inspection setup is illustrated by figure 2.6; the inspection consists of two separate wedge mounted transducers for transmission and reception. The transmitted wave is typically a longitudinal wave. The figure shows both the 'lateral' waves and diffracted waves traveling towards the receiving transducer. The lateral wave is generated by mode conversion of the incident wave to a surface wave; the surface wave has the shortest path and is therefore the first signal received assuming the velocities are the same. This is a limitation with the ToFD approach because the lateral wave can mask any diffraction signals that have similar transit times, such as from near-surface defects. The waves diffracted from the defect tip are used to measure the through-wall height of the defect relative to the backwall. Although figure 2.6 depicts a surface-breaking defect inspection, ToFD is also applicable to embedded defects where both tips of the defect are detected to provide a measure of the through-wall defect extent.

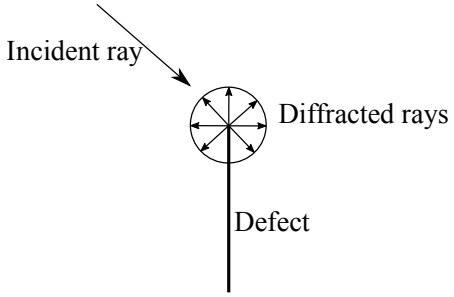


Figure 2.5: For a ray normally incident on a diffracting edge, a circle of diffracted rays are produced in the plane of the incident ray.

ToFD inspections rely on the time-of-flight of the diffracted waves and do not make use of the amplitude information for defect characteristion. The ability to predict the amplitude of the diffracted waves is, however, important when designing an inspection to ensure that they will be visible above the noise threshold. For example, it was reported by Ogilvy *et al.* [27] and experimentally confirmed by Ravenscroft *et al.* [26] that there is significant variation in the amplitude of the diffracted waves depending on the angles of insonification and detection. The theoretical predictions proposed by Ogilvy *et al.* are based on a semi-analytical formulation of the Geometrical Theory of Diffraction (GTD) by Chapman [28]. GTD was initially developed by Keller [24] as an extension to Geometrical Optics and was first applied to elastic wave scattering by Achenbach *et al.* [29–31].

For the configuration depicted in figure 2.5, where a circle of diffracted rays are produced, the far-field wave potential for the diffraction from the tip of a straight

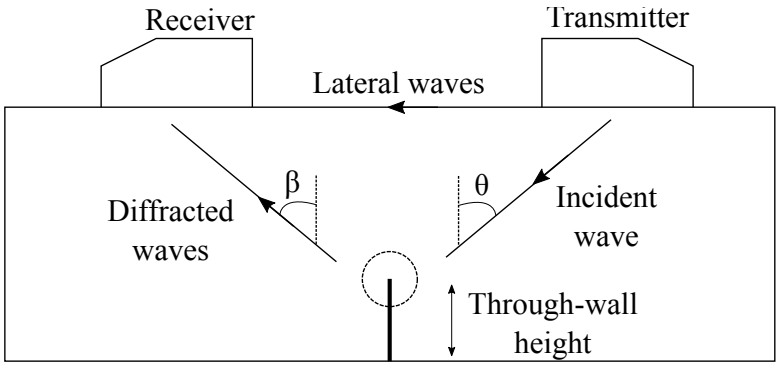


Figure 2.6: A typical ToFD inspection setup.

edge semi-infinite crack are given [27], for the compression wave mode, by:

$$\phi_d = \left\{ \begin{array}{c} F_p(\theta, \beta) \\ G_p(\theta, \beta) \end{array} \right\} \left(\frac{\lambda_p}{R}\right)^{\frac{1}{2}} e^{ik_p R} \tag{2.22}$$

and for the shear wave mode:

$$\psi_d = \left\{ \begin{array}{c} F_s(\theta, \beta) \\ G_s(\theta, \beta) \end{array} \right\} \left(\frac{\lambda_s}{R}\right)^{\frac{1}{2}} e^{ik_s R} \tag{2.23}$$

where R is the distance from the point of diffraction to the point of observation, θ and β are the incident and diffracted angles as defined in figure 2.6 and $F_{p,s}$ and $G_{p,s}$ are the diffraction coefficients, which are omitted here for brevity but can be found in [27]. Equations 2.22 and 2.23 can be determined on a case-by-case basis for specific material properties and for specific incident and diffracted angles. Alternatively, it is common for the diffraction coefficients to be calculated for specific material properties that are typical for NSRP components, such as stainless steel, and listed in a look-up table for efficient generation of results.

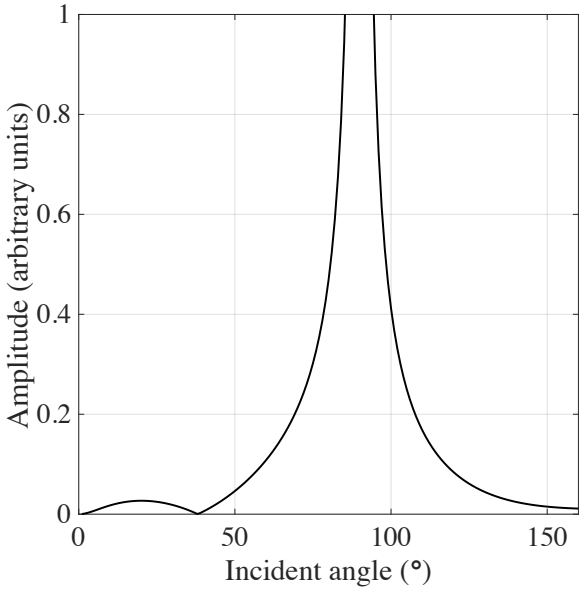


Figure 2.7: The amplitude of a compression wave mode diffracted signal due to an incident compression wave over a range of incident angles. The angle of diffraction is equal to the incident angle.

As an example, figure 2.7 shows the amplitude of a diffracted compression wave where the angle of incidence and reception are equal ($\beta = \theta$). Of note is the predicted minimum in the diffraction coefficient at 38°; this observation has been experimentally validated by Ravenscroft *et al.* [26] and is commonly avoided in a ToFD inspection. Following the minimum, the signal rapidly increases in amplitude until the diffracted waves become indistinguishable from the direct transmission signal at $\theta = 90°$.

GTD has been used extensively in the ultrasonic testing (UT) of nuclear plant components; much of the development and validation of GTD for use with ultrasonic inspections was carried out by Coffey and Chapman [28, 32] and Chapman [7] for the justification of the ultrasonic inspection of the Pressurised Water Reactor (PWR) at Sizewell B. In [32], comparisons with exact solutions to the wave equation are given for the backscattered shear wave when a plane shear wave is incident on a smooth flat crack. GTD is shown to perform well across all angles of incidence. Experimental validation is given in [7] for the backscatter from smooth planar cracks and flat bottom holes, which show good agreement over a range of incident angles.

The ability to predict the amplitude of the diffracted waves both facilitates the design of a ToFD inspection and provides a basis for justifying the inspection. However, the theoretical model discussed here is based on various limiting assumptions, e.g. plane wave incidence, high frequency approximation and that the defect is smooth, flat and semi-infinite. In reality, ultrasonic inspections often encounter defects that have a complex morphology and features that may have a size of the order on the ultrasonic wavelength. Because of this, the application of this theory is commonly used along side extensive experimental trials, which also often only consider idealised crack shapes due to the manufacturing constrains when producing artificial defects. This highlights that there is clear need for an accessible and validated modelling procedure to account for the effect of defect complexity in ultrasonic inspections.

2.2.3 Longitudinal Creeping Wave Inspection

Longitudinal creeping waves are referred to by various names, such as subsurface longitudinal waves (SSL) [15, 33], critically refracted longitudinal waves [34] or simply as creeping waves [23]. Creeping waves are said to be generated when a longitudi-

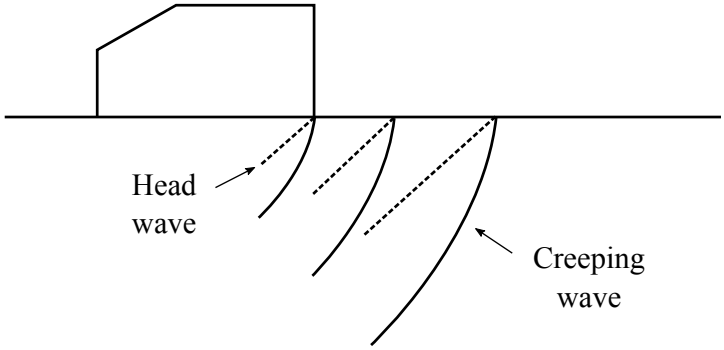


Figure 2.8: Generation of longitudinal creeping waves.

nal wave is incident on the boundary between liquid and solid media or two solid media at an angle which is close or equal to the first critical angle [15, 35]. Rose [15] describes the phenomenon as a high angle longitudinal wave whose wavefront demonstrates a maximum in amplitude at an angle at approximately 10° to 20° from the inspection surface. This is illustrated by figure 2.8. Away from the wedge-mounted transduction system, the boundary condition at the component surface is the stress-free condition. The creeping wave interacts with the boundary and in order to satisfy the boundary condition, a 'head' wave with shear polarisation is generated (figure 2.8) [15, 35]. The head wave travels with an angle calculated by Snell's law for a longitudinal wave incident at the first critical angle.

Annex A.5 in the British Standard for ultrasonic testing of welds [36] suggests that creeping waves can be used to detect defects that are near or connected to the inspection surface, up to a depth of approximately one wavelength from the surface. Creeping waves are said to be preferable to Rayleigh waves as they are less sensitive to surface roughness [15] as well as providing greater sensitivity in coarse-grained anisotropic weld material due to their longitudinal polarisation. However, it is noted in the British Standard [36] and by various authors that the propagation distance of a creeping wave is limited due to the continual generation of the shear head wave [23, 33].

Creeping waves can also be used to detect inner surface-breaking defects [23, 36–38] by the generation of secondary creeping waves through mode conversion as a shear wave is incident on the backwall, illustrated in figure 2.9. The work from Langenberg *et al.* [33] indicates that a shear wave is generated simply from refraction at the wedge-component interface, as well as the head wave described above. The secondary creeping wave may result from refracted shear wave or the head wave,

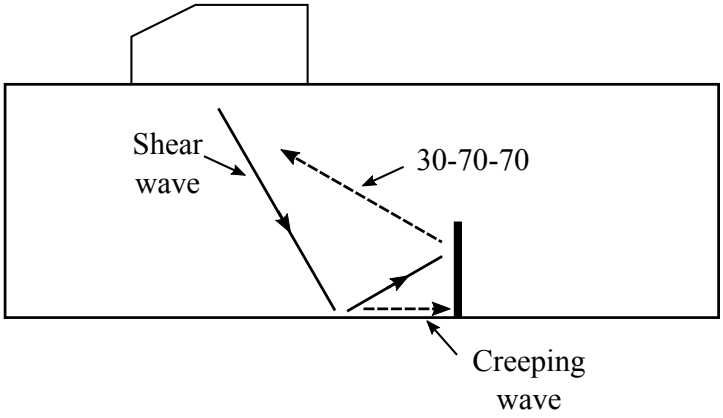


Figure 2.9: Inner surface-breaking defect detection with secondary creeping waves and the 30-70-70 path.

as they propagate at the same angle in the component. The American Society for Testing and Materials (ASTM) standard [39] describes the detection of an inner surface-breaking defect though mode conversion of the reflected secondary creeping wave back to a shear wave and is said to be detected by the transducer on the inspection surface. The standard also describes the accompaniment of the '30-70-70' detection mechanism (also commonly referred to as the TLL inspection), where a shear wave incident at 30° on the backwall mode converts into a 70° longitudinal wave. The 70° longitudinal wave is reflected in a specular direction from the defect and returns to the transducer (figure 2.9).

An important distinction must also be made between a Rayleigh wave mode that propagates along a concave surface, which has previously also been called creeping waves [40], and the longitudinal creeping wave referenced here. The Rayleigh creeping waves are also known as 'leaky' Rayleigh waves [41] as they continuously radiate bulk waves in order to satisfy the boundary conditions at the curved surface.

2.2.4 Ultrasonic Array Inspections

In contrast to the monolithic transducers employed in the aforementioned inspection techniques, ultrasonic arrays are composed of an arrangement of smaller piezoelectric transducer elements. The elements of the array can be fired individually and with a pre-calculated time delay; therefore, through the superposition of the individual wave fields it is possible to form plane or focused ultrasonic beams over a wide range of incident angles. This concept is known as beamforming [42] or phasing [43], which has led to the name Phased Array (PA) testing for inspections of

this type. Phased array transducers have many advantages, such as the ability to interrogate a component from multiple angles with a single transducer and powerful post-processing capabilities. A review of ultrasonic arrays for NDE can be found in [44] and an overview of PA testing in [43].

As well as conventional beamforming, a technique known as Full Matrix Capture (FMC) offers an alternative data acquisition procedure; FMC lends itself to the application of post-processing algorithms and works by individually and sequentially firing each element of the array. For each element fired, the ultrasonic wave field is recorded on all array elements [45]. With the FMC dataset, beamforming algorithms can be applied in post-processing. This enables the operator to interrogate the component under inspection with multiple incident ultrasonic beams from a single dataset.

Recently, there has been research into the application of post-processing algorithms, also known as imaging algorithms, to the case of inner surface-breaking defects. Felice *et al.* [46] have proposed an adaptation of the Total Focusing Method (TFM); TFM focuses the incident ultrasound at all points in the field of view, generating an image which can be used to identify and characterise potential defects [45]. When applied to the inspection of an inner surface-breaking defect, Felice *et al.* noted that, on the TFM image, the indication from the crack root (where the crack meets the backwall) has the potential to obscure the indication received from the crack tip, particularly for small or tilted cracks. The ability to size a defect from the TFM image is therefore hindered. The modification made in [46] was to account for the ultrasonic ray paths that include a reflection from the component backwall when generating a TFM image. The algorithm was termed the Half-Skip TFM (HSTFM) because 'half-skip' is typically used to describe a reflection from a component backwall. Felice *et al.* showed that the image produced by HSTFM for surface-breaking defects provided an improved ability to determine defect size in comparison to conventional TFM. There have also been recent developments in the application of Super-Resolution (SR) imaging algorithms to the inspection of surface-breaking defects. Zhang *et al.* [47] investigated the ability of the Factorisation Method (FM) to image surface-breaking defects and found that it was possible to size a defect with a length equal to the incident wavelength using this method.

Ultrasonic array inspections offer clear advantages in both data manipulation and inspection cost and efficiency in comparison to conventional monolithic trans-

ducer inspections. However, array transducers and the necessary equipment are often more expensive than conventional transducers and require specialist training. Furthermore, FMC data acquisition times and the required computational memory to store the data is often far greater than for conventional inspections. These practical challenges have limited the deployment of array inspections in the nuclear sector.

2.2.5 Summary

This section has reviewed ultrasonic inspections techniques that are commonly employed for the inspection of inner surface-breaking defects. By considering the reflection coefficient for the corner echo scattering mechanism, it was shown that the angled beam shear wave inspection technique generates a strong reflected signal and is therefore a common choice of inspection technique. The ToFD inspection, which is another common inspection technique, was also reviewed along with a discusson of the semi-analytical GTD theory that is used to aid in the design of such inspections. ToFD is most commonly used for measuring the through-wall extent of surface-breaking cracks; diffraction signals are also commonly detected in the angled shear wave inspection therefore often mitigating the need for a separate ToFD inspection.

The longitudinal creeping wave inspection offers another approach for the detection of inner surface-breaking defects, yet it was discussed that this technique has limited application due to the attenuation of the creeping wave. Emerging array imaging algorithms offer novel approaches to detect and size small surface-breaking defects yet their take up in the nuclear industry has been slowed due to the practicalities of the inspection.

2.3 Semi-Analytical Models

Semi-analytical models, although they often compromise on versatility, generally surpass the efficiency of numerical methods. Three of the most widely used semi-analytical models are the Born approximation, GTD and Kirchhoff Approximation (KA). Each of these techniques have been used in the power generation industry to help the design and justification of ultrasonic NDE inspections. GTD has been

discussed in subsection 2.2.2; in this section, a description of the Born approximation and KA is given. Following this, a review of the semi-analytical methods which have been applied to the case of scattering from near-surface and surface breaking defects is given in section 2.3.3.

2.3.1 Born Approximation

The Born approximation is a low frequency approximation and is used to calculate the scattering from inhomogeneities whose properties do not vary far from the background material, such as inclusions.

As with most general scattering problems, the total field is represented as a linear superposition of the incident and scattered field:

$$\phi^{tot} = \phi^{inc} + \phi^{scat} \tag{2.24}$$

Equation 2.14 described wave propagation in the absence of external sources and therefore governs the propagation of the incident field, ϕ^{inc}. In the presence of a scattering object, the right hand side (RHS) of equation 2.14 is replaced by a forcing function and becomes inhomogeneous [48]:

$$(\nabla^2 + k_0^2)\phi(\mathbf{r}, \omega) = -O(\mathbf{r}, \omega)\phi^{tot}(\mathbf{r}, \omega) \tag{2.25}$$

$O(\mathbf{r}, \omega)$ is known as the object function or the scattering potential and is a mathematical representation of the inhomogeneity. Equation 2.25 describes the wavefield purely due to the presence of inhomogeneities in the medium which the incident wave is propagating and therefore represents the scattered field, ϕ^{scat}.

Green's function is defined as the impulse response of an inhomogeneous differential equation, such that it returns the Dirac delta function, δ, as the source term when acted on by a linear differential operator, which in this case is the Helmholtz operator:

$$(\nabla^2 + k^2)G(\mathbf{r}|\mathbf{r_0}) = \delta(\mathbf{r} - \mathbf{r_0}) \tag{2.26}$$

where $\mathbf{r_0}$ is the location of a source and $\mathbf{r}$ is the receiver location. With knowledge of the Green's function, the response of an arbitrary forcing function $f(\mathbf{r_0})$ can be

calculated through the convolution integral:

$$\phi(\mathbf{r},\omega) = -\int G(\mathbf{r}|\mathbf{r_0}) f(\mathbf{r_0},\omega) \mathrm{d}\mathbf{r_0} \tag{2.27}$$

Equation 2.27 states that the response to a forcing function can be represented by a linear superposition of the system's impulse response. Combining this result with Green's theorem leads to an expression for the scattered field [48]:

$$\phi^{scat}(\mathbf{r}) = -\int_{V'} G(\mathbf{r}|\mathbf{r}') O(\mathbf{r}') \phi(\mathbf{r}') \mathrm{d}\mathbf{r}' \tag{2.28}$$

where $\mathbf{r}'$ represents a location in the volume, V', of the inhomogeneity. From equation 2.24 an expression for the total field can then be found:

$$\phi^{tot}(\mathbf{r},\omega) = \phi^{inc}(\mathbf{r},\omega) - \int_{V'} G(\mathbf{r}|\mathbf{r}') O(\mathbf{r}') \phi(\mathbf{r}') \mathrm{d}\mathbf{r}' \tag{2.29}$$

which is a form of the Lippmann-Schwinger equation. This equation states that the total field is equal to the incident field superposed with a sum of sources, of strength $-O(\mathbf{r}')\phi(\mathbf{r}')$, at the locations of the inhomogeneity. The first order Born approximation simply assumes that the total field at any point in the inhomogeneity can be represented by the incident field. The scattered field can therefore be calculated by the interaction of the incident field with the object function at every point in the inhomogeneous medium. Equation (2.28) then becomes:

$$\phi_B(\mathbf{r}) = -\int_{V'} G(\mathbf{r}|\mathbf{r}') O(\mathbf{r}') \phi^{inc}(\mathbf{r}') \mathrm{d}\mathbf{r}' \tag{2.30}$$

For the total field to be approximated by the incident field at all points in the medium, it is clear that the properties of the inhomogeneity must not deviate far from the background material; in other words, the scattered field must be a lot weaker than the incident field, limiting the applicability of this approximation.

The Born approximation has been used in the context of elastic wave scattering [49, 50], however its use is typically limited to the low frequency regime and for inhomogeneities which have properties similar to the background material. In general, this approximation is of limited use in the modelling of ultrasonic elastic wave scattering from cracks because the impedance mismatch between metal and

the air in the crack is extremely large.

2.3.2 Kirchhoff Approximation

KA is widely employed in the nuclear power generation industry for modelling the ultrasonic scattering from crack surfaces and is often used as a complementary model to GTD [7, 28]. The KA model is based on the Helmholtz-Kirchhoff scattering formula. In the acoustic model, the scattered field at a point, $\mathbf{r}$, is given by:

$$\phi^{scat}(\mathbf{r}) = \int_{S_0} \left(G(\mathbf{r}|\mathbf{r_0}) \frac{\partial \phi(\mathbf{r_0})}{\partial n_0} - \phi(\mathbf{r_0}) \frac{\partial G(\mathbf{r}|\mathbf{r_0})}{\partial n_0} \right) \mathrm{d}S_0 \tag{2.31}$$

where S_0 is the closed surface of the scatterer and n_0 is the normal on the surface of the scatterer at the point $\mathbf{r_0}$. KA provides a means to approximate the value of the wavefield on the surface of the scatterer, $\phi(\mathbf{r_0})$, and its derivative by treating each point on the surface of the scatterer as if it were a point on an infinite plane tangential to the scatterer, as depicted by figure 2.10. In the application to the scattering from crack surfaces, it is common to assume the Dirichlet boundary condition [51]:

$$\phi(\mathbf{r_0}) \equiv 0 \tag{2.32}$$

This reduces equation (2.31) to:

$$\phi^{scat}(\mathbf{r}) = \int_{S_0} \left(G(\mathbf{r}|\mathbf{r_0}) \frac{\partial \phi(\mathbf{r_0})}{\partial n_0} \right) \mathrm{d}S_0 \tag{2.33}$$

In the fully elastic case under the stress-free boundary conditions, the scattered displacement field, $\mathbf{u}^{scat}(\mathbf{r})$, is found using the elastic Green's tensor, $\Sigma_{ijk}(\mathbf{r}|\mathbf{r_0})$ [8]:

$$u_k^{scat}(\mathbf{r}) = \int_{S_0} \Sigma_{ijk}(\mathbf{r}|\mathbf{r_0}) u_i(\mathbf{r_0}) n_j(\mathbf{r_0}) \mathrm{d}S_0 \tag{2.34}$$

where $\mathbf{u}(\mathbf{r_0})$ and $\mathbf{n}(\mathbf{r_0})$ are the total displacement field and the unit normal at $\mathbf{r_0}$, respectively. Using KA, the amplitude of the total displacement field is calculated from plane wave reflection coefficients of displacement, analogous to those given by equations 2.17 - 2.19.

In the context of NDE, experimental validation has been carried out by Coffey and Chapman [32] for the case of 2.5 MHz shear wave P-E inspection from a

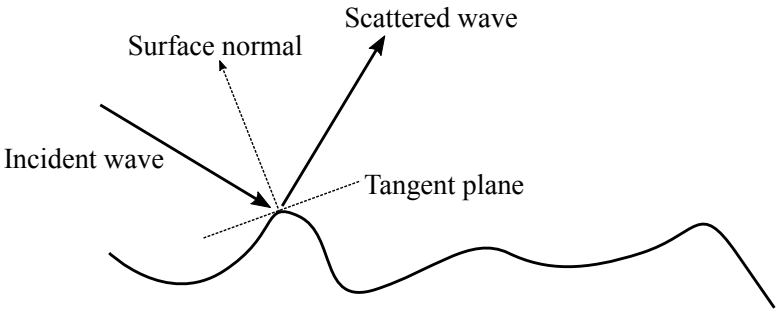


Figure 2.10: Illustration of the tangential plane approximation.

smooth Flat Bottom Hole (FBH) inclined at 5° to normal incidence. The results are presented in the form of a contour plot and show good agreement between theory and experiment in the shape and amplitude of the contours. As discussed in [52] and highlighted by Chapman [7], KA is accurate for predicting the scattered field in the specular and near-specular directions but is less accurate for predicting the scattered field in other directions because the proximity of the crack edge is not taken into account.

By accounting for the local variations in gradient along the scatterer surface, KA can be used to account for the effect of roughness on the scattered wavefield [53, 54], as shown by figure 2.10. The work by Ogilvy [53] shows that amplitude of the ultrasonic wave reflected from a defect can be greatly affected by the presence of surface roughness. Zhang *et al.* use KA to determine the effect of defect roughness on the detectability of defects using ultrasonic array inspections. However, the use of the infinite tangential plane approximation in KA leads to the limitations on the applicability of this model. The approximation assumes that each point is fully insonified by the incident wavefield and that there is only a single interaction of the wavefield with that point. Consquently, multiple scattering surface shadowing and surface wave phenomena are neglected. Bass and Fuks [55] highlight that this theory remains accurate provided that the local surface radius of curvature, a, is much larger than the incident wavelength, i,e. $ka\cos^3(\theta) >> 1$, where θ is the angle between the direction of the incident wave and the local mean plane normal.

Thorsos validated KA against exact results for surfaces which have roughness varying in one dimension (i.e. constant in the out-of-plane direction) [56]. It was found that KA performed well except at low grazing angles and where multiple scattering effects were prominent. Zhang *et al.* [54] compared the scattered field obtained by FE simulations and Kirchhoff theory. KA was shown to maintain a

good level of consistency with the FE results for incident angles ranging from $-80°$ to $80°$ for defects with a roughness of $\lambda_0 \geq 0.5\lambda$ and $\sigma < 0.3\lambda$. Here, σ is defined as the Root Mean Square (RMS) height of the rough surface and λ_0 is the Surface Correlation Length (SCL). The Kirchhoff model was therefore used in this angular range in preference to an FE model due to the lower computational cost. Shi [57] provides a comprehensive assessment of the validity of elastic KA by comparison to numerical results in both 2D and 3D. It was concluded that at normal incidence, KA remains valid when $\sigma^2/\lambda_0 \leq c$, over the range of scattering angles from $-70°$ to $70°$. In 2D, c is given by one fifth of the incident longitudinal wavelength. Whereas in 3D, i.e. a 3D simulation, the restriction is tighter and c becomes 0.14λ, highlighting the importance of considering the ultrasonic scattering from complex defects in 3D.

The studies that have been considered here show that KA is applicable to real defects within a regime of validity. In general, KA is valid for predicting the ultrasonic response from large planar defects that have low levels of roughness where the contribution from edge diffraction signals is negligible.

2.3.3 Extended Methods for Surface-Breaking Defects

The aforementioned semi-analytical methods are valid for isolated defects. In the presence of a large stress-free boundary, such as the back wall of a material, consideration must be given to the effect this will have on the scattered wave.

An approximate method was given by Achenbach [58] who utilised elastodynamic ray theory to evaluate the ultrasonic surface wave interaction with a surface-breaking defect. Similarly, Achenbach and Norris [59] applied GE and GTD to the problem to study the interference of the edge diffracted signal and corner echo signal in the ultrasonic scattering from a surface-breaking defect. An interesting approach was used to model the rays incident on the defect and backwall. This is outlined in figure 2.11, where the defect is extended symmetrically about the backwall and treated as an isolated defect. The ultrasonic ray paths are extended across the back wall to create artificial image rays, simplifying the treatment of a surface-breaking defect. Although mode conversion is considered, only longitudinal rays are used in the approximation by Achenbach. As with the high frequency approximations previously discussed, the model also assumes that the defect is much larger than the incident wavelength.

In a recent paper by Chapman *et al.* a suite of semi-analytical models for predicting the scattered ultrasonic field from planar defects in ferritic steel is outlined [60]. The in-house models have been developed by British Energy in collaboration with the British Nuclear Group. Two of these semi-analytical models are specifically designed to be used with surface-breaking defects and are named COREDGE and CORKIRCH. COREDGE is based on a special case of the GTD model which calculates the diffraction of elastic waves from the corner of a wedge. It is discussed that the corner echo from a surface-breaking defect is optimised when the defect is perpendicular to the back wall surface, as this will give the largest specular reflection. However if the defect is tilted, the diffracted waves from the corner between the defect and the back wall may enable detection. The CORKIRCH model utilises KA to calculate the corner echo from a surface-breaking defect. The model also creates an imaginary extension to the defect and ray paths and treats the defect as isolated, as in figure 2.11.

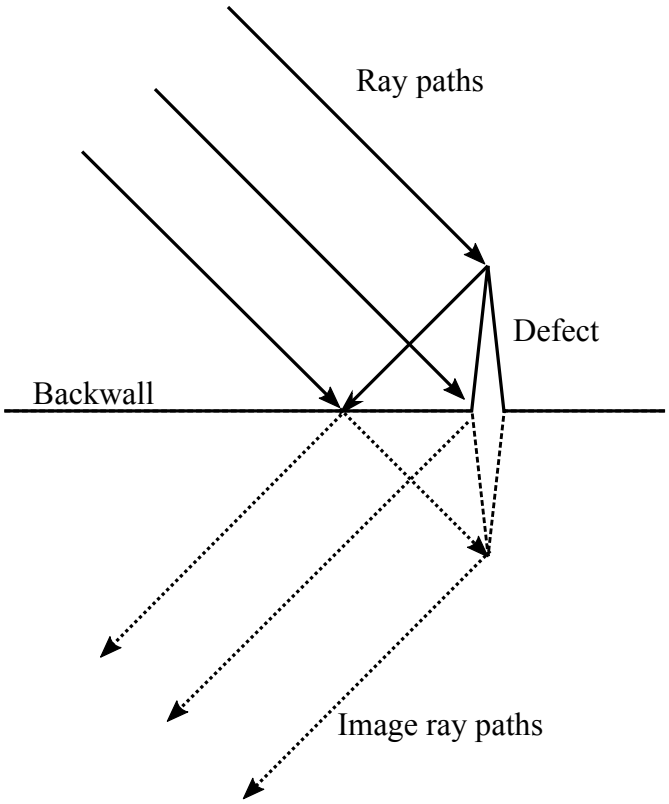


Figure 2.11: Achenbach and Norris modelled a surface-breaking defect as an isolated defect by extending the defect and ray paths symmetrically about the backwall.

2.3.4 Summary

Semi-analytical models are advantageous due to their low computational cost and are widely employed in the development of ultrasonic inspections of NSRP components. The methods presented here are based upon certain approximations which restrict their applicability. The Born approximation is valid in the low frequency regime for scatterers whose properties do not vary significantly from the background material. Kirchhoff and GTD are high frequency approximations which break down when the size of the defect becomes comparable to the wavelength of the incident ultrasonic wave field. The adaptations of KA and GTD, CORKIRCH and COREGDE, are also subject to these limitations and are therefore only valid for a specific range of inspection parameters. In some cases, it may be beneficial to utilise semi-analytical methods within a known range of validity. The motivation of this project is, however, to provide an efficient modelling procedure to simulate the inspection of surface-breaking defects which are complex and are typically outside the regime of validity of semi-analytical methods.

2.4 Numerical Models

Partial Differential Equations (PDE's), such as the wave equation, are only analytically solvable for a limited number of cases; to arrive at exact solutions, approximations and simplifications are applied to the system. In most cases this results in a loss of generality or the generation of solutions that are only valid in a specific range. Numerical methods are employed to obtain accurate solutions by solving a system of equations at discrete locations. The accuracy of numerical methods is dependent on the ability to correctly define or represent a certain system as a discrete set of points or regions. With increasing computational power, numerical methods can generate very reliable solutions to almost any system. More specifically, a very accurate representation of the scattering of ultrasound from complex defect geometries can be obtained. There are various types of numerical modelling methods; four common techniques are discussed here, namely Finite Difference (FD), Finite Volume (FV), the Boundary Element Method (BEM) and Finite Elements (FE).

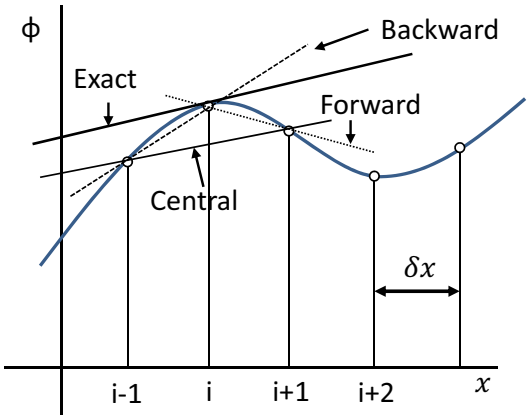


Figure 2.12: A diagram which shows the calculation of an exact derivative and the approximations used in the finite difference scheme .

2.4.1 Finite Difference

In finite difference methods, a structured grid of nodes is assigned to a solution domain, which is a region where the solutions to a differential equation is required. The nodal values of the functions within the differential equation are used to approximate the value of derivatives at each grid point. The approximation used by FD methods comes from calculating a truncated Taylor series expansion of the function to be derived about a node. Equivalently, the approximation arises from the definition of the derivative of the function:

$$\left(\frac{\partial \phi}{\partial x}\right)_{x_i} = \lim_{\delta x \to 0} \frac{\phi(x_i + \delta x_i) - \phi(x_i)}{\delta x} \tag{2.35}$$

where $\phi(x_i)$ is the value of a well-behaved function at the node x_i and δx is the distance between two nodal points on a grid. This is essentially the gradient between two points, as represented in figure 2.12. Also shown in figure 2.12 are three difference approximations to calculating the gradient, known as the forward difference scheme (FDS), backward difference scheme (BDS) and central difference scheme (CDS). These are calculated using the equations:

$$FDS : \left(\frac{\partial \phi}{\partial x}\right)_i \approx \frac{\phi_{i+1} - \phi_i}{x_{i+1} - x_i} \tag{2.36}$$

$$BDS : \left(\frac{\partial \phi}{\partial x}\right)_i \approx \frac{\phi_i - \phi_{i-1}}{x_i - x_{i-1}} \tag{2.37}$$

$$CDS : \left(\frac{\partial \phi}{\partial x}\right)_i \approx \frac{\phi_{i+1} - \phi_{i-1}}{x_{i+1} - x_{i-1}} \tag{2.38}$$

It is clear from figure 2.12 that the accuracy of each scheme is dependent on the location of the nodes. However for increasingly small spacing between points, their values converge. From equations (2.36), (2.37) and (2.38) the first order derivative can be approximated at all nodal points enabling quantities of interest, such as velocity, to be obtained.

The second order derivative may be required for the calculation of quantities such as acceleration. It can be calculated be applying the approximation to the first derivative twice:

$$\left(\frac{\partial^2 \phi}{\partial x^2}\right)_i \approx \frac{\left(\frac{\partial \phi}{\partial x}\right)_{i+1} - \left(\frac{\partial \phi}{\partial x}\right)_i}{x_{i+1} - x_i} \tag{2.39}$$

It can be noted from the above equation that at least 3 nodes are required for the calculation of the second order derivative. Here the second order derivative is represented using a FDS, however a BDS or CDS can also be used [61].

Many examples of the use of FD within NDE can be found in the literature. An example relevant to this project is Scandrett and Achenbach's [62] use of the FD technique to simulate the scattering of a shear wave incident at 45° to a smooth planar surface-breaking defect in a weld between two plates. Comparison with an analytical Kirchhoff model shows agreement; however, discrepancies arise due to the assumptions and limitations of KA and errors in the FD model, which are on the order of the square of the grid spacing. This follows from the fact that the higher order terms in the Taylor series expansion are neglected in the CDS, FDS and BDS; therefore the neglected terms are a measure of error and the largest of which will be the second order (squared) term.

An advantage of the FD method is its relative simplicity. However, a major limitation of using FD is that the complexity of the analysis is significantly increased if a non-structured grid is required, such as for complex defect geometries, and these are much better handled by other methods, i.e. FE models. Historically, this has been one of the main reasons why FE has become more popular for modelling domains with complicated geometry and is discussed further in subsection 2.4.4.

2.4.2 Finite Volume

The Finite Volume (FV) method utilises conservation laws in order to predict the value of a vector field, such as displacement or pressure, at specific locations throughout the model. Typically, a 3D grid of discrete volumes is generated and the vector field is conserved across the boundary of each volume. It is based on the divergence theorem, which states that the divergence of a vector field integrated over a volume is equal to the net flow of vector flux across the volume boundary:

$$\int_V (\nabla \cdot F) dV = \int_S (F \cdot n) dS \tag{2.40}$$

The vector field within a discrete volume can therefore be calculated with knowledge of the vector flux across its boundary. In general, however, the integrand will not be known at all points on the surface and approximations must be made in order to make the integration achievable.

FV provides more generality over FD as a grid is only required for definition of volume boundaries and does not need to be structured. However inaccuracies can arise quickly with this method if the surface or volume of integration is large (i.e. the discretisation is coarse) and also due to assumptions made to the behaviour of the function or vector field which is interpolated over the surface of the discrete volumes. The way in which the FV method is constructed means that it lends itself well to applications such as fluid dynamics, where the conservation of flow is the basis for its formulation, and is less appealing for use in elastic wave propagation. Despite this, Dormy and Tarantola [63] outline a FV method for elastic wave propagation. In their work, propagation in unstructured grids is achieved at the cost of inconsistency and lower accuracy than FD methods.

2.4.3 Boundary Element Method

The Boundary Element Method (BEM) is a numerical technique of solving boundary integral equations. Due to its diverse applicability, there is a significant amount of literature on this method. The reviews by Beskos [64, 65] are recommended for an in-depth overview the the applications of BEM.

Depending on the problem, a boundary integral equation is formulated from a governing PDE using some prescribed initial and boundary conditions and typically

the fundamental solution of the PDE, such as the Green's function. BEM performs numerical discretisation on the boundaries on which the integral equations are defined. In 2D, line elements are used to construct a mesh on the domain boundary, whereas in 3D a mesh of surface elements is imposed on the boundary. The solution to the integral equation is approximated along each element using an interpolation procedure, which then enables the calculation of the solution within the solution domain.

BEM has been used in the context of ultrasonic NDE. For example, Kitahara *et al.* [66] formulated a BEM for the problem of bulk wave scattering from an inclusion and Cho *et al.* used a hybrid BEM model to study the scattering of guided and plate waves [67, 68]. The main advantage of BEM over other numerical techniques is that no discretisation is required other than on the defined boundary, often leading to a reduction in computational effort. In addition, the integral equations are typically formulated using the Sommerfeld radiation condition, removing the requirement of other boundary conditions such as absorbing boundaries, which can often occupy a significant proportion of the solution domain in other numerical approaches.

However, although no discretisation is required in the solution volume using BEM, it involves a dense matrix calculation. In comparison to FE, where only a sparse matrix is created, the computation time of BEM may not be significantly different [69] and in some cases is greater. Increases in computation time can occur due to increasing scatterer size and for complex scatterer geometries. As BEM is not widely used in industry, there are few robust commercial BEM software packages available.

2.4.4 Finite Elements

FE is one of the most widely used numerical modelling techniques. Early applications to the propagation of waves can be found in work by Alsop *et al.* [70] and Smith [71]. Further work on this method within the area of NDE displayed the diversity and accuaracy of this technique [72–74].

In FE, a numerical grid is constructed by either surface or volume discretisation. The discrete areas or volumes are known as elements. The elements are often of triangular or quadrilateral shape in 2D or of tetrahedral or hexahedral shape in 3D. In a simple mesh of elements, nodes are placed at the vertices of the elements

connecting them to neighbouring elements. In a more refined mesh containing higher order elements (which allow for higher order interpolation schemes), nodes can be placed at many points around the element. A system of equations are solved at the nodes in order to find the required field variables, which are then propagated across each element by a form of interpolation [75]. In an explicit time-domain FE simulation, the calculations are performed in a time-marching manner, where the previously calculated values are taken as pseudo-initial conditions for the current time-step. Implicit FE modelling of wave propagation is typically used for the time-harmonic steady state response of a system. Time-domain implicit models are available [76] however they have proved less efficient than the explicit method [10].

For the explicit time-domain elastic wave simulation, the equation of dynamic equilibrium is used to quantify the response of a system to an external force [77], and is expressed:

$$[M]\ddot{\boldsymbol{u}} + [C]\dot{\boldsymbol{u}} + [K]\boldsymbol{u} = [F_a] \tag{2.41}$$

where $\boldsymbol{u}$, $\dot{\boldsymbol{u}}$ and $\ddot{\boldsymbol{u}}$ are displacement, velocity and acceleration vectors respectively. $[M]$ is a diagonal matrix which represents the mass of the system. A simplification commonly used is known as the 'lumped' mass matrix where the total mass of the system is distributed amongst, or lumped at, the nodes of the predefined mesh. $[C]$ is the viscous damping matrix and is a summation of the mass proportional and stiffness proportional damping of the system. $[K]$ is the stiffness matrix and finally $[F_a]$ is a matrix describing the external time-dependent forcing applied to the system.

In the absence of an initial external force there will clearly be zero displacement, and therefore velocity and acceleration, at all nodes in the mesh. The application of a time-varying force, such as a tone burst, to a set of nodes will disrupt the initial static equilibrium and generate a wave to propagate through the system.

In a comparison between the FD and FE methods, Frehner *et al.* [78] confirmed that the most efficient scheme consists of an FE method for spatial discretisation and an FD method for temporal discretisation. The velocity and acceleration at the time step, t, are related to the displacement through the use of the central difference operator:

$$\dot{\boldsymbol{u}}^{(i)} = \frac{1}{2\delta t}\left(\boldsymbol{u}^{i+1} - \boldsymbol{u}^{i-1}\right) \tag{2.42}$$

$$\ddot{\boldsymbol{u}}^i = \frac{1}{\delta t^2}\left(\boldsymbol{u}^{i-1} - 2\boldsymbol{u}^i + \boldsymbol{u}^{i+1}\right) \tag{2.43}$$

where δt is the time increment and i is the increment number. Equations (2.42) and (2.43) are substituted into equation (2.41) and rearranged to give:

$$\boldsymbol{u}^{i+1} = \left([M]\frac{1}{\delta t^2} + [C]\frac{1}{2\delta t}\right)^{-1}\left[[F] + \boldsymbol{u}^{i-1}\left([C]\frac{1}{2\delta t} - [M]\frac{1}{\delta t^2}\right) + \boldsymbol{u}\left([M]\frac{2}{\delta t^2} - [K]\right)\right] \tag{2.44}$$

As all terms on the right hand side of (2.44) are known, $\boldsymbol{u}^{i+1}$ can be calculated explicitly. Under the assumption of lumped mass, both $[M]$ and $[C]$ are diagonal therefore the calculation of the first term on the right hand side of equation (2.44) is efficient. The stiffness matrix, $[K]$ is also a sparse matrix, where the only non-zero values are those relating the stiffness of neighbouring nodes.

As explicit analysis computes the displacement after every time step, conditions must be placed on the size of the time step to prevent instability within the model. The increment δt must be less than a critical time step δt_{cr}, which is given by [75] :

$$\delta t_{cr} = \frac{2}{\omega_{max}} \equiv \frac{T_{min}}{\pi} \tag{2.45}$$

where ω_{max} and T_{min} denote the maximum frequency and shortest time period of the wave propagating through the model. For the simulation of ultrasonic waves, the critical time step is usually approximated as the transit time of the fastest propagating wave across the smallest element of the mesh [10]. Although the number of time steps in this type of analysis is large, the computation time for each increment is small which makes it attractive for the simulation of wave propagation.

To accurately model wave propagation it is necessary for there to be a minimum number of nodes per the shortest wavelength in the model. This is quantified by the parameter N:

$$N \leq \frac{\lambda_{min}}{dx} \tag{2.46}$$

where λ_{min} is the shortest wavelength in the model and dx is the width of the smallest element. In ultrasonic NDE modelling, a minimum value of $N = 15$ is typical in order to accurately model the system and minimise numerical reflections within the mesh [10]. However with increasing computational power, much higher values of N are used to minimise errors.

A key advantage of FE is its versatility. The FE mesh does not need to be

structured or ordered in a particular way to arrive at a solution, which makes it a powerful tool for simulating the ultrasonic interaction with complex geometries [11, 79]. Research has been carried out into the use of automatic irregular mesh generation, which is a function built into FE software that allows unstructured meshing around geometric discontinuities, in comparison to structured meshing for simulating the scattering of ultrasound [79]. It was found that the automatic mesh generation yielded acceptable results for ultrasonic scattering for the typical mesh size mentioned above. However, it was also found that in order to model wave propagation to the same degree of accuracy as the regular square mesh, the element size must be half the size than that used in the square mesh. A detailed study has been carried out by Drozdz [10] which investigates the optimum model parameters to be used when modelling elastic waves in solid media.

The run times and computational memory requirements of FE models are seen as its major limitations, especially for models in 3D. However, recent work by Huthwaite [80] has shown that a substantial reduction in run time can be achieved by performing the analysis on a GPU. This has been successfully implemented in the form of a software package, Pogo, which performs explicit time domain finite element elastodynamic simulations on a GPU. A comparison to commercial FE software demonstrated that the run time was reduced by two orders of magnitude using Pogo [80].

The computational cost of an FE model depends largely on its size. For an accurate model of the scattering of ultrasound from cracks or defects, the scatterer must be isolated from any artificial domain boundaries such that the scattered signal can propagate independent of further unwanted interactions. One method of achieving this is to increase the size of the model, such that the received scattered signal can be distinguished from other unwanted reflections. However, this reduces the computational efficiency. A substantial amount of research has gone into developing techniques which can provide the same solution but with greater efficiency by the use of absorbing boundaries, which change the properties of elements that lie on or close to the model boundary to induce damping of outgoing waves. Two common types of absorbing boundaries are Perfectly Matched Layers (PML) and Absorbing Layers using Increasing Damping (ALID). Although PMLs have been shown to achieve satisfactory damping in a smaller absorbing region, they are suited to frequency-domain solvers and are not available in many commercial FE packages

[81]. The development of the Stiffness Reduction Method (SRM), an extension to conventional ALIDs, have shown satisfactory absorption for an absorbing region with a thickness on the order of a wavelength [82] and are easily implemented in commercial FE software.

2.4.5 Summary

FE modelling provides superior versatility and accuracy for the simulation of elastic wave scattering from complex defects in comparison to FD, FV and BEM. Recent developments in performing the FE analysis on the GPU has seen substantial increases in computational efficiency [80]. However the problem of the large computational memory requirements of FE, especially in 3D, is still a topic of research and is an important topic for this project. The following section reviews hybrid semi-analytical numerical approaches, which are aimed at solving this problem.

2.5 Hybrid Methods

In the context of modelling within ultrasonic NDE, a hybrid method typically refers to a model which combines both numerical and (semi-)analytical methods. It is apparent from sections 2.3 and 2.4 that each type of modelling technique brings significant advantages, but also significant drawbacks. Analytical models are able to predict the response of an ultrasound inspection efficiently and provide insight into the underlying phenomena. Their validity is limited, however, for example ultrasonic analytical models are typically only valid in a specific frequency range and become inaccurate when the defect geometry is complex. Numerical models, typically FE methods, are able to predict the ultrasonic response from an arbitrary system, including the inspection of complex defects. To accurately reproduce complex defect geometry, however, a high level of mesh refinement is required leading to slow and inefficient computation, especially in 3D systems. This section outlines three methods of utilising the efficiency of analytical models and the versatility of FE models into a hybrid technique.

2.5.1 CIVA Athena

CIVA is a widely used NDT modelling package and is described as semi-analytical. It uses what is known as the 'pencil' method [83, 84] to propagate ultrasonic waves within a medium, which is a high frequency ray technique that accounts for reflection and transmission at material interfaces. CIVA utilities multiple scattering models, such as KA, GTD and the Born approximation, to describe scattering from defects; the scattering models are combined with the calculated transducer response through Auld's reciprocity theorem [22] to predict the ultrasonic response at the detecting transducer. Although it is computationally efficient, it is subject to the limitations of semi-analytical methods and as a result is unable to accurately describe the interaction with complex defects.

In a collaboration between CIVA and EDF Energy, the CIVA semi-analytical model has been linked to a specialised FE code Athena to enable the simulation of the ultrasonic response from complex geometries. Athena is an explicit FE scheme developed by EDF which uses a fictitious domain method for spatial discretisation of complex-shaped defects [85, 86]. A condition of the code is that the defect box must be big enough such that no reflections arrive before emission into the box has finished because detection and emission cannot simultaneously occur [86], which limits the advantages of a hybrid technique. This may be overcome using absorbing layers, however there is no demonstration of this in the literature for this particular technique. Experimental validation of this hybrid model in two dimensions shows good agreement between simulation and experiment for simple artificial defect shapes [12]. However, there is limited validation for the model and it is also not yet commercially available in 3D, although this is being developed.

2.5.2 Finite Element Local Scattering

Recent work has been carried out by Zhang *et al.*[54, 87, 88] and Wilcox and Velichko *et al.* [13, 89] on the use of the scattering matrix, termed S-matrix, to characterise defects. The S-matrix describes the far field amplitude of the scattered ultrasonic field due a plane wave incident on a defect as a function of the incident angle, scattering angle and incident wave frequency. The scattered wave field amplitude, u_s, measured at a point in the far field, r, due to a time-harmonic plane wave, u_0,

incident on an arbitrary defect is given by [90]:

$$u_s = u_0 S(\theta_1, \theta_2, \omega)\sqrt{\frac{\lambda}{r}}e^{ik(r-\lambda)} \tag{2.47}$$

where θ_1 is the incident angle and θ_2 is the scattering angle and $S(\theta_1, \theta_2, \omega)$ is the S-matrix. To completely characterise the behaviour of ultrasonic scattering from the defect requires 4 scattering matrices in 2D and 9 scattering matrices in 3D in order to describe each incident and scattered wave mode. With knowledge of the field incident on the scatterer, the coefficients of the scattering matrix $S(\theta_1, \theta_2, \omega)$ can be deduced from measurements of the scattered field amplitude via equation (2.47). The S-matrix enables the scattered field due to any incident field to be calculated [89]. A key application of this measurement is to characterize a defect by comparing an experimentally measured S-matrix with simulated S-matrices [87, 91].

An FE model is used by Velichko and Wilcox [92] to obtain the scattered field at incident and scattered angles ranging from 0° to 360° of a defect with arbitrary shape. An incident plane wave of the required wave mode is synthesized from a series of monopole and dipole sources constructed from point sources in the FE model. The model uses the Helmholtz-Kirchhoff scattering formula [89] to analytically continue the scattered field measured by the FE model to the far field in order to calculate the required coefficients for the S-matrix. Velichko and Wilcox have also presented this formulation, termed Finite Element Local Scattering (FELS), generalized to three dimensions and for guided waves, which has shown good agreement with analytical solutions [13].

An adaptation of this technique to include near surface or surface-breaking defects is given in [93]. In this case, the S-matrix describes the scattered wave field due to an incident plane wave and plane wave reflections from the surface interface; consideration is also given to surface waves arising on the stress free boundary. Scattering matrices are then obtained for incident and scattering angles ranging from 0° to 180° corresponding to propagation within the elastic half-space.

The FELS 2D model is validated against an analytical prediction of the scattering from a circular cavity [89], which shows that approximately 40 elements per wavelength are required in the FE model when using square linear elements. The 3D model is also compared against an analytical solution for a spherical scatterer [13]; in this case, tetrahedral elements are used with a discretization of 15 elements

per wavelength (longitudinal). Good agreement is found for the scattered longitudinal wave, yet this becomes less accurate for the scattered Shear Vertical (SV) polarization, which is attributed to the mesh discretization in the FE model being too coarse for the shear wavelength. Experimental validation of the 2D model was provided by Felice [94] by comparing the TFM image of a wire eroded embedded target and branched notch. By sizing the embedded scatterers using the -6 dB drop technique on both simulated and experimental images, good agreement was found. The relative amplitude of the features in the images of the notch also showed agreement to within 1 dB between experiment and simulation. Although the FELS model can be extended to any incident wave field configuration, the S-matrix method is ultimately targeted towards ultrasonic array inspection modelling.

2.5.3 Generic Domain-Linking Scheme

The technique developed by researchers at Imperial College [14, 95] offers flexibility in the hybrid methodology, such that it can be adapted to suit specific requirements and applications. The method simulates a bulk wave ultrasonic inspection by breaking it down into two separate domains, the source and defect domain, and couples them together using a semi-analytical hybrid interface, illustrated by figure 2.13.

The hybrid interface is designed to be independent of the techniques used to simulate each domain providing the required flexibility. This allows compatibility with commercial modelling packages as well as enabling each part of the inspection to be modelled with the most suitable solvers or software. For example, wave excitation and reception is often well represented by semi-analytical methods, whereas scattering from an arbitrary defect geometry may be best calculated in FE. By isolating the source and defect domains, the propagation between them can be computed semi-analytically which enables either a combination of methods or a reduction of the size of a full numerical approach.

The hybrid interface, which acts as the semi-analytical link between the source and defect domains, is based on the Helmholtz-Kirchhoff formula for wave scattering. For example, the displacement potential of a compression wave (ϕ) is propagated from the defect domain (domain 1) to the source domain (domain 2) via the integral formula:

$$\phi(\mathbf{r}_2) = \int_{S_1} (\phi(\mathbf{r}_1)\nabla G_\phi(\mathbf{r}_2|\mathbf{r}_1) - G_\phi(\mathbf{r}_2|\mathbf{r}_1)\nabla\phi(\mathbf{r}_1)) \cdot \mathbf{n}\mathrm{d}S_1 \tag{2.48}$$

where $\mathbf{r}_1$ and $\mathbf{r}_2$ are positions on the boundary of domain 1 (S_1) and domain 2 respectively and G_ϕ is the Green's function, which in dimensionless form is given by:

$$G_\phi(\mathbf{r}_2|\mathbf{r}_1) = \frac{1}{4\pi}\frac{e^{-i(\omega\gamma|\mathbf{r}_2-\mathbf{r}_1|}}{|\mathbf{r}_2-\mathbf{r}_1|} \tag{2.49}$$

where γ is the ratio of the shear to compression wave speeds. Equation 2.48 also applies to the displacement vector potential of shear wave propagation ($\boldsymbol{\psi}$) and the

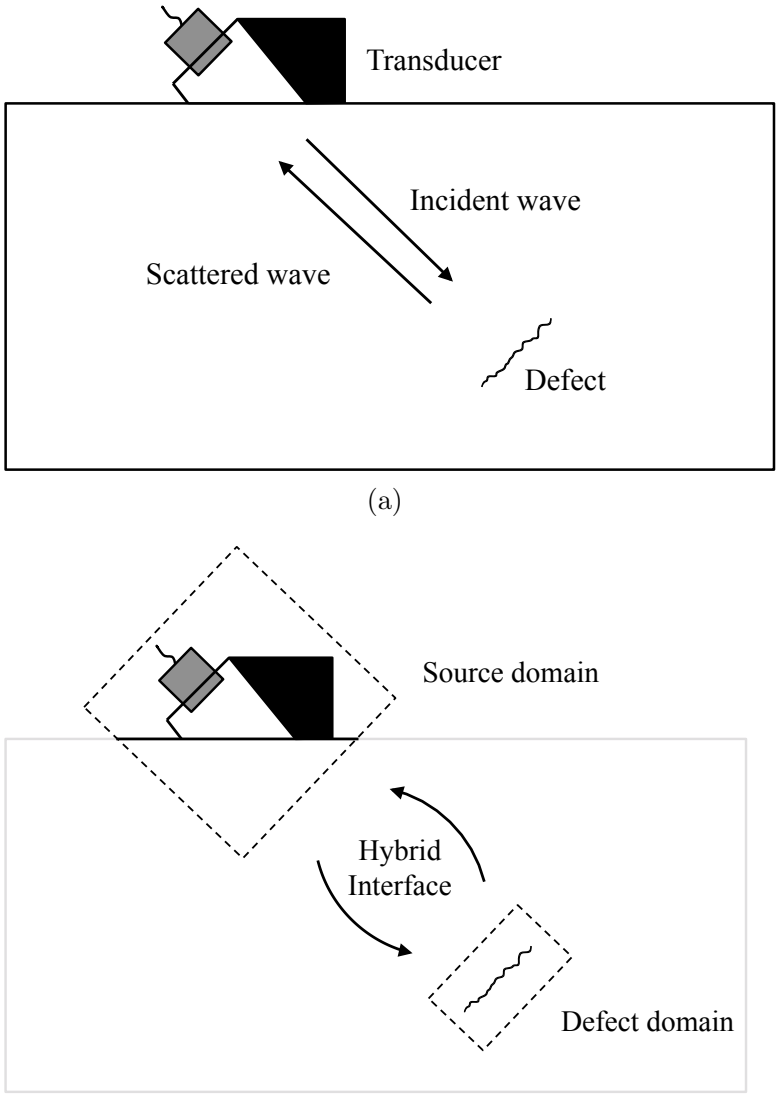


Figure 2.13: An illustration of (a) a pulse echo ultrasonic inspection setup and (b) the hybrid methodology used to simulate the inspection.

Green's function in the dimensionless form is defined by:

$$G_{\psi}(\mathbf{r}_2|\mathbf{r}_1) = \frac{1}{4\pi}\frac{e^{-i(\omega|\mathbf{r}_2-\mathbf{r}_1|}}{|\mathbf{r}_2-\mathbf{r}_1|} \tag{2.50}$$

which is equivalent for each component of the vector potential. As there are 3 components of displacement represented by 4 potentials, the gauge condition, $\nabla \cdot \boldsymbol{\psi} = 0$, is employed to enable the calculation of the displacement potentials. Under this condition, the derivation of the compression and shear potentials from displacements and stresses are given in [95] and are not repeated here for brevity.

The formulation given by equation 2.48 takes the displacement and stress field quantities along the boundary of one simulation domain and propagates the wave fields through the bulk isotropic elastic medium to the boundary of another domain. If a scatterer is present within the simulation domain, the scattered field is extracted via equation 2.24; a separate model is therefore required to calculate the incident field at the boundary of the simulation domain. The use of time-domain FE models to calculate the scattered wave field from a complex geometry requires the Fourier transform of the field quantities measured on the boundary of the simulation domain. Once the hybrid interface calculation is complete, the time-domain signals are recovered through the inverse Fourier transform. In addition, an advantageous aspect of this formulation is that it can handle field quantities in the near field, as shown in [96]. This allows for the boundary of the defect region to be as close to the defect as possible and the size of the FE model can be minimized.

The work by Rajagopal *et al.* [14] and Choi *et al.* [97] provide validation of the generic hybrid technique in 2D and 3D, respectively. In [97], the 3D hybrid model is used to simulate the shear wave inspection of a Side-Dilled Hole (SDH), and the resulting scattered wave is compared to a full FE model and experimental data. Excellent agreement is achieved with the comparison to a full FE model and modest agreement with experimental results. The deviations in amplitude between the hybrid and experimental results are attributed to variations due to couplant, differences in the simulated and experimental pressure profile over the surface of the transducer and positional error of the transducer in the experiment. Verification against FE for the simulation of ultrasonic scattering from a rough embedded defect in 2D is given in [11], which shows good agreement over a range of scattered angles and the level of disagreement is on the order of $-30\,\mathrm{dB}$.

This hybrid method is not tied to a specific inspection technique; although figure 2.13 depicts a pulse echo inspection, the domain representing the reception of scattered waves can be in a separate location to the source, for example, as in a ToFD inspection. This generality, combined with the fact that it is compatible with commercially available FE software, makes it a very suitable choice for technology transfer to industry. In the work referenced here, the model is limited to the simulation of embedded defects and does not consider guided wave scattering.

2.5.4 Summary

This section investigated three hybrid modelling techniques that attempt to address the increasing need for the accurate and efficient simuation of the ultrasonic inspection of larger volumes of material and complex features. All three methods use some form of domain-linking technique to connect (semi-)analytical and numerical methods in order to obtain the benefits of both simulation techniques. Hybrid modelling is an essential tool in the development of FE capabilities in this project. The main advantage will be the ability to perform efficient simulations in 3D, which will enable accurate simulation of current inspections of components containing complex surface-breaking defects. The hybrid model described in section 2.5.1 is advantageous due to the use of the widely employed model CIVA; however, it is based upon the development of a specialized FE code and has not yet been extended to 3D. As discussed in subsection 2.5.2, the S-matrix method is a powerful simulation method for ultrasonic array inspections, yet it lacks the immediate versatility required for this work and requires bespoke software to be developed, potentially hindering its use in the industry. With the model outlined in section 2.5.3, effort has been given to create a generic model which does not rely upon the development of specific code, providing a solid platform for technology transfer into industry. This versatile model has also been extended into 3D with experimental validation and is chosen for further development in this project to simulate the inspection of complex inner surface-breaking defects.

Chapter 3

Ultrasonic Beam Model

The ability to account for the ultrasonic transduction system is a key requirement of the modelling capability delivered by this project. As discussed in the previous chapter, this project is focused on the use and development of the hybrid model described in section 2.5.3, herein referred to as 'the hybrid model'. This chapter reports on the development the transduction system model and its linkage to the hybrid model.

3.1 Introduction

Previous applications of the hybrid model [14, 95, 97, 98] considered the linkage of two FE models, depicted by the 'box-to-box' approach in figure 2.13. In those applications, the transduction system is simulated using an FE model, termed the source box, where a line (2D) or surface (3D) of nodes and elements corresponding to the shape of the transducer are selected for the generation and reception of the incident and scattered waves, respectively. This approach is advantageous as it has the ability to account for a complex transduction system and is not limited by assumptions and approximations made by analytical-based methods.

As described in section 2.5.3, simulation of the incident wave field propagation is termed the forward model and the simulation of the scattered field propagation is termed the backward model. In the approach used in this project, it is proposed that the forward model is simulated using a semi-analytical beam model, which links directly to the finite element defect domain simulation. This is because a semi-analytical model is often much more computationally efficient than an equivalent

FE one and there are many well-established analytical [7, 90, 99] and semi-analytical [100, 101] models for simulating the common ultrasonic transduction systems.

The results from the beam model are directly coupled to the FE defect domain in the hybrid model. The output of the selected beam model only provides information on the phase and magnitude of the incident wave field; however, excitation of the incident wave within the FE domain requires knowledge of the direction of the incident wave loading conditions. Therefore, in section 3.3, an approach to couple a beam model to an FE model based on Huygens' principle is validated. Finally, section 3.4 validates the linkage of the beam model and FE by comparison to the commercially available semi-analytical model software CIVA.

3.2 Huygens-Fresnel Beam Model

In this project, it was decided to use a beam model based on the Huygens-Fresnel principle of superposition. This decision was made on the basis that this method is simple to implement, computationally efficient and allows for full user control over the points of calculation. The model is also versatile, such that it is not limited to a specific transducer crystal shape or beam profile and can be used to simulate wedge-mounted and array transducers [102].

The Huygens-Fresnel beam model models a transducer as an array of point sources uniformly distributed over its surface. The phase and amplitude of the incident wave generated by the transducer is calculated by summing the contribution from each point source. If the transducer is mounted on a wedge, as depicted in figure 3.1, it is assumed here that the wedge supports only longitudinal waves; previous studies have shown that the shear wave field in the wedge have a negligible contribution to the field radiated into the component [103]. The incident wave complex displacement amplitude, A, at a point, $\mathbf{P}$, within the test piece is given by:

$$A(\mathbf{P}) = \sum_{j=1}^{n} \frac{1}{R_E} e^{-i(k_1 R_1 + k_2 R_2)} T(\theta_j) \tag{3.1}$$

where n is the number of point sources, R_E is the effective propagation distance between point source j and the point P, k_1 and k_2 are the wave numbers for waves propagating in material 1 and 2 respectively, R_1 and R_2 are the distances propagated in material 1 and 2 respectively, T is the transmission coefficient and θ_j is the angle

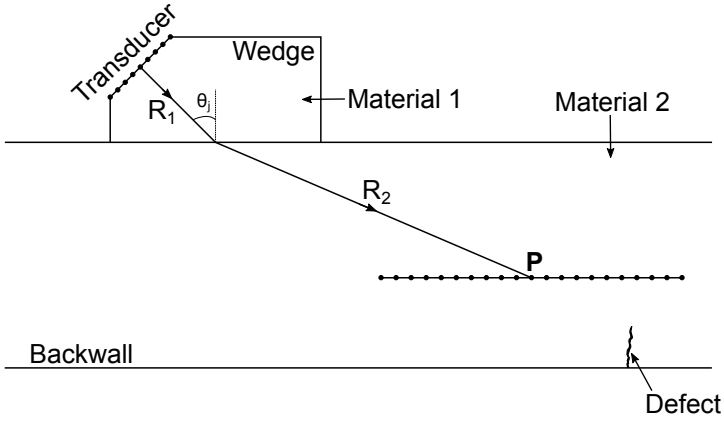


Figure 3.1: Schematic of the Huygens-Fresnel beam model setup for a wedge-mounted transduction system.

of incidence which the ray due to point source j makes with the interface between material 1 and 2. Here, material 1 is the wedge and material 2 is the parent material.

The ray path from each point source to a location in the component is calculated by Fermats principle of least time [104], which accounts for refraction between the two media in an equivalent manner to Snell's law. With knowledge of the ray path, the incident angle of the ray on the interface between material 1 and 2 is known; therefore, the transmission coefficient can be calculated. The propagation distance, R_E, accounts for the amplitude decay due to the radial expansion of the point source. An approximation given by Johnson *et al.* [105], which has been validated by Duxbury [106], provides an effective amplitude decay distance that accounts for the refraction between two media:

$$R_E = R_1 \frac{\cos\theta_2}{\cos\theta_1} + R_2 \frac{C_2}{C_1} \frac{\cos\theta_1}{\cos\theta_2} \tag{3.2}$$

where θ_1 is the angle of incidence in material 1, θ_2 is the angle of refraction in material 2 and C_1 and C_2 are the wave speeds in material 1 and 2 respectively. The amplitude is calculated over a range of frequencies and is multiplied by the spectrum of an excitation signal, such as a toneburst. The inverse Fourier transform is used to obtain a displacement time history at the point of calculation in the component.

The point sources on the surface of the transducer are uniformly distributed with a minimum spacing of $\lambda_{inc}/5$; this level of discretisation has previously been shown to provide accurate results [107].

3.3 Finite Element Point Source Simulation

To couple the beam model to the FE model of the defect domain, the incident field phase and amplitude calculated from the beam model are applied as an excitation to an array of point sources in the FE model. Using Huygens' principle, the incident field will be generated within the FE model by the superposition of the fields radiated from each point source.

Due to the discretised nature of FE, excitation signals can only be applied at predefined nodal locations in a specified direction. It is therefore impossible to generate a spherical or cylindrical wave with uniform amplitude in all directions from a single node. To overcome this issue, it is common to apply an excitation to a selection of neighboring nodes to approximate the point source wave field. In the field of seismology, authors have studied the field radiated from an approximate point source generated in both FD [108] and FE [109] models in order to achieve an accurate explosion or earthquake source. In NDT, Zhang *et al.* uses an eight node ring to produce a cylindrical compression wave [87], whereas Drozdz [10] employs a four node excitation source to generate cylindrical compression and shear waves.

The accuracy of an incident wave field generated by Huygens' principle is dependent upon the uniformity of both the phase and amplitude of the spherical field radiated by the FE point sources. Wilcox and Velichko [89] study the relative amplitude and phase error of a compression wave point source generated by the 8 node method. Their study finds unacceptable errors if the centre of the source does not fall on a nodal location and a new approach is developed for accommodating for an arbitrary point source centre location. In this work, due to the use of the beam model, it is feasible to constrain the location of source centres and therefore this method is not required here.

To demonstrate types of 2D FE sources, the far field radiation pattern of the longitudinal and shear wave modes generated by the excitation of a single node and the four node combination is plotted in figure 3.2. The results from this figure have been generated from an FE model; the radiation patterns are measured on the perimeter of a circle with a radius of $7\lambda_L$ from the point source. Each node in the point source is excited with a 3 cycle 2 MHz tone burst in the direction shown in the figure. The figure shows that the uniaxial forcing of a single node causes both wave modes to propagate. The longitudinal and shear wave mode decay according to the

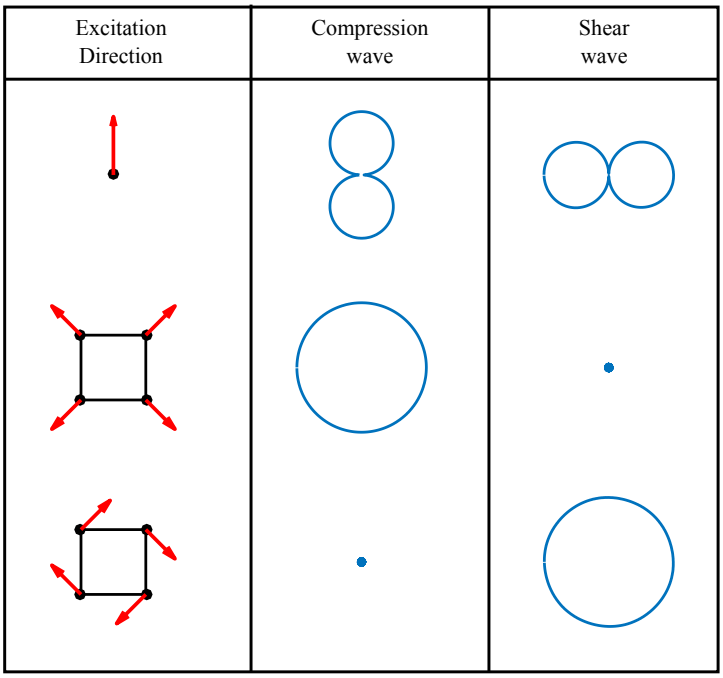


Figure 3.2: Far field radiation patterns for various types of 2D FE sources.

projection of the force vector in the radial and tangential directions respectively. Using a combination of four nodes to create radial or tangential particle motion, it is clear that excellent modal purity can be achieved.

This work is primarily focused on the development of 3D simulations. The use of approximate point sources to reconstruct an incoming wave in a 3D FE model has not previously been demonstrated in the literature. In the following subsections, the wave fields generated by approximate 3D point sources for both shear and longitudinal wave modes is measured to ensure the application of Huygens' principle will accurately reconstruct the incident wave.

3.3.1 Shear Wave Point Source

According to the hedgehog theorem, it is not possible for a continuous tangent vector field to exist on a sphere in three dimensions without vanishing [110]. As a result, it is not possible to generate a spherically expanding wave field with a polarization that is tangential to the direction of propagation in all directions. For the transduction systems of interest to this project, however, the shear wave fields have a defined polarization which can be exploited in the design of an approximate

shear wave point source.

Figure 3.3 shows one approach for generating a spherically expanding shear wave; here, eight neighbouring nodes located at each vertex of a cube are excited in a torsional manner. This approach is selected because all nodes are equidistant from the centre of the element. It is clear from figure 3.2 that this method of excitation will uniformly radiate a shear wave polarised in the y-z plane (with reference to the coordinate system in the figure). However, in the x-y and x-z planes, this will not be the case and the amplitude of the wave will diminish. In this section, the radiation pattern in each plane is measured to understand whether such sources will be effective for the application of Huygens' principle.

An FE model containing the source pictured in figure 3.3 is executed. Each node on the source is excited using a 3 cycle tone burst with a centre frequency of 2 MHz in the directions specified in figure 3.3. The material properties of stainless steel are assumed: the longitudinal and shear velocities are $5760\,\mathrm{m\,s^{-1}}$ and $3110\,\mathrm{m\,s^{-1}}$ respectively and the density is $7800\,\mathrm{kg\,m\,s^{-1}}$. All other parameters used in the FE model are given in table 3.1. Tetrahedral elements ares used to mesh the model as

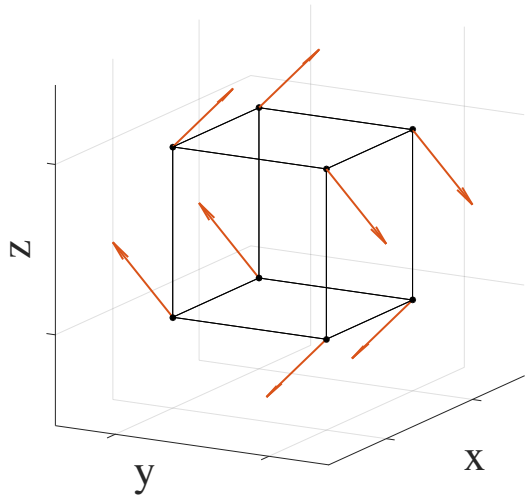


Figure 3.3: An approximate 3D shear wave point source for an FE model. 8 neighboring nodes are excited in a torsional manner to generate a spherically expanding polarised shear wave.

Table 3.1: FE model parameters

Element Type	Element size (µm)	Time step (ns)	SRM layer thickness (λ_L)
Linear Tetrahedral	75	2.5	1.5

they are typically used for unstructured meshes. Although an unstructured mesh is not used here, the results from this study are applicable to models that use tetrahedral elements when conforming to complex geometries. The mesh is generated in MATLAB (The MathWorks, Inc., Massachusetts, United States); in this technique, many regular hexahreda discretise the FE domain and each hexahedron is divided into 6 tetrahedra. The edge length of the hexahedra is 75 µm resulting in a mesh density of approximately 20 elements for wavelength at the centre frequency. This is a typical mesh density for 3D models, as it provides a compromise between the criteria set out by Drozdz [10] and computational efficiency.

The displacement due to the wave field radiated from this source is measured on 3 rings of nodes that lie in each orthogonal plane centred on the point source with a radius of $2\lambda_S$, as depicted by figure 3.4. The monitoring rings are found by selecting the node that is closest to the desired location and each ring contains 230 nodes. The component of displacement corresponding to the shear and longitudinal wave amplitudes will be found at each node on the monitoring rings. In addition, the time of arrival of the shear wave will be compared to an exact analytical prediction to measure the time of flight error. The analytical prediction of the time of flight will use the location of the monitoring nodes, rather than the desired monitor ring location, to ensure a true estimate of time of flight error is provided. The maximum of the Hilbert envelope of the wave from the FE model is used to measure its time

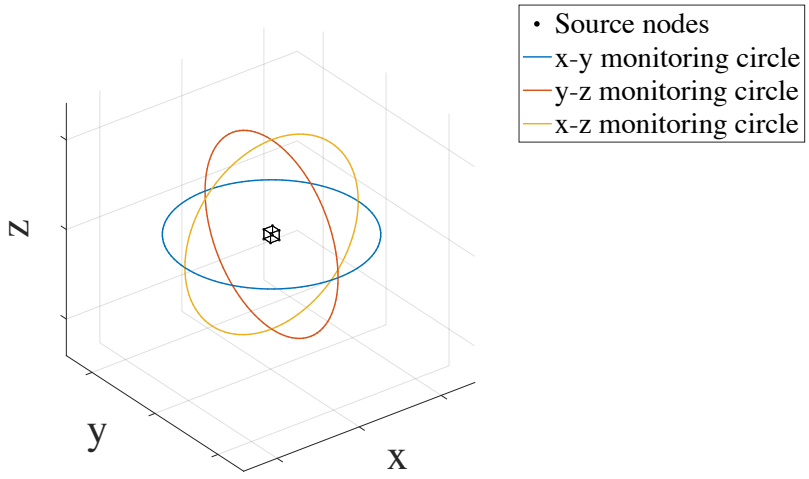


Figure 3.4: A schematic of the three monitoring circles used to measured the field radiated from the point source. The legend describes which Cartesian axis plane the monitoring circles are parallel to.

of flight.

3.3.2 Results

The results are plotted in figure 3.5. All amplitudes plotted in the figure are normalised to the maximum peak amplitude measured on all rings. The colour of the lines on the plot correspond to their orientation in the Cartesian coordinate system, for example the blue line corresponds to the ring which lies in the $x - y$ plane; this colouring system also corresponds to figure 3.4. The definition of theta on the polar plots is depicted in 3.6, which also shows a projection of the loading applied to each node in the point source.

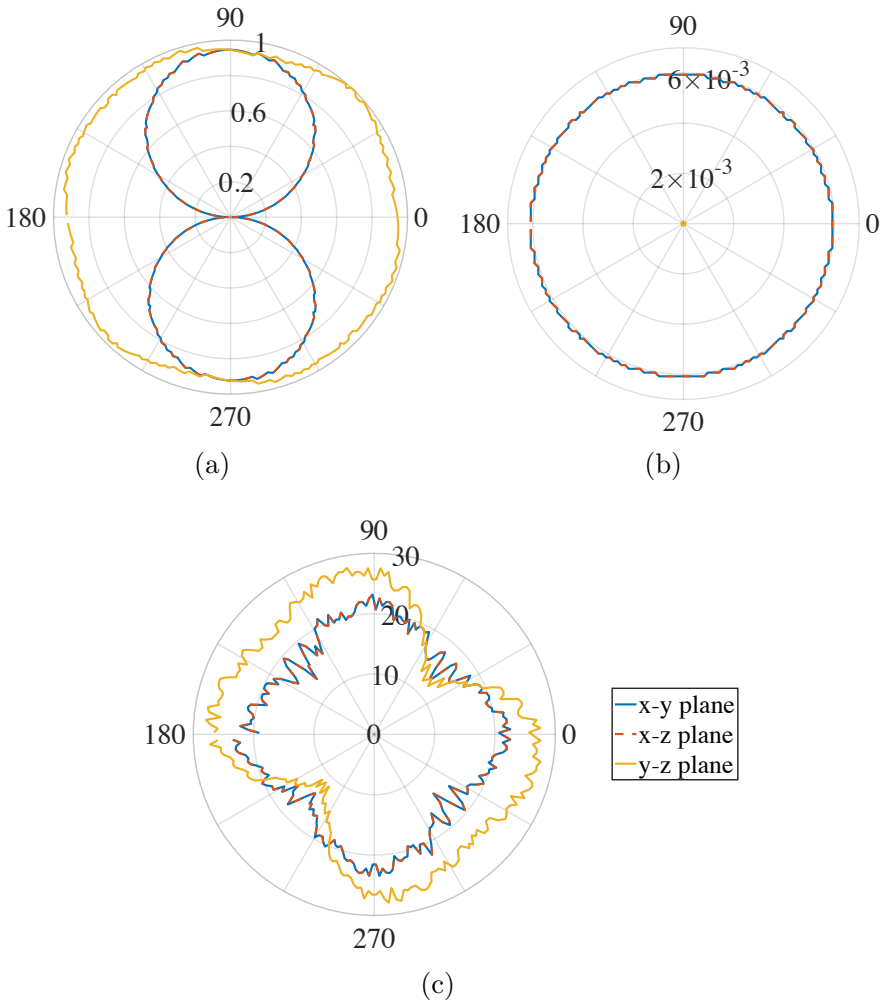


Figure 3.5: Polar plots of the results obtained from the monitoring circles in each orthogonal plane. (a) shows the normalised shear wave amplitude, (b) the compression wave amplitude normalised to the shear wave and (c) the time of flight error for the shear wave where the radial axis has units of nanoseconds.

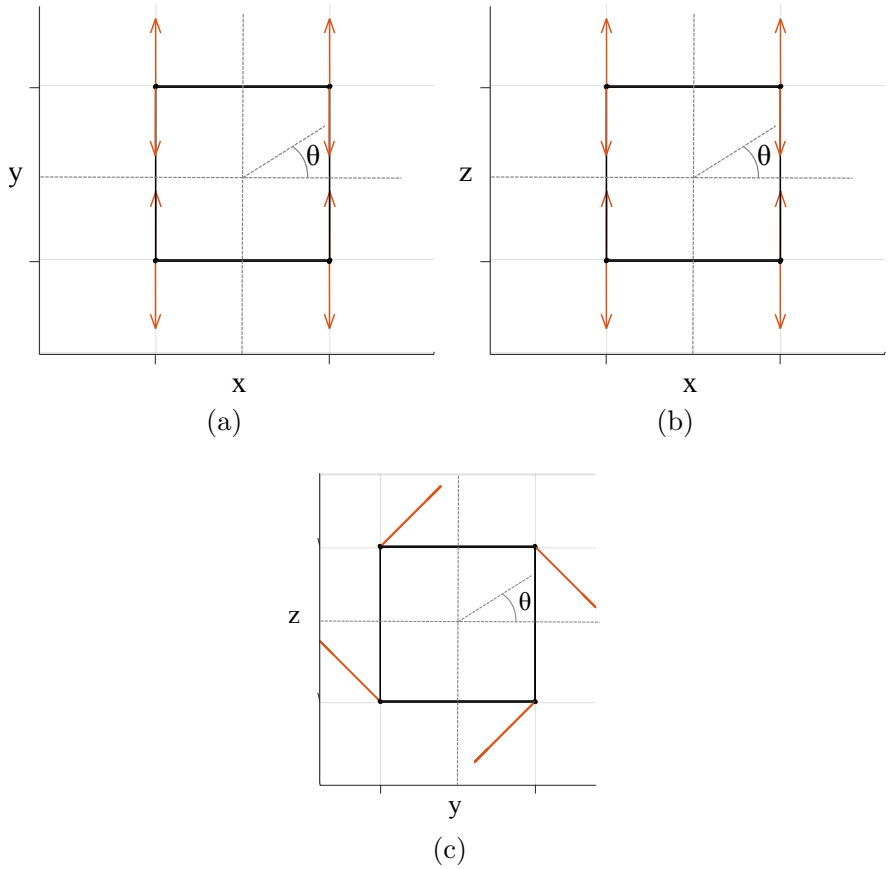


Figure 3.6: A projection of the shear wave point source in the (a) $x-y$, (b) $x-z$ and (c) $y-z$ planes along with the definition of the angle θ used in figure 3.5.

Figure 3.5(a) displays the amplitude of the shear wave which passes through each orthogonal monitoring ring. As predicted, the results from $y-z$ plane plotted in yellow are comparable to that of the 2D shear wave source in figure 3.2 because the shear wave is polarised in this plane. The shear wave amplitude in the $y-z$ plane is more consistent over 360° in comparison to the amplitude measured in the other two planes, with a mean amplitude of 95%, varying by 10%.

The radiation patterns of the shear wave measured on the rings that lie in the $x-y$ and $x-z$ planes are shown by the blue and red lines in figure 3.7 and are equal due to the rotational symmetry of the source around the x-axis. The polarisation of the spherical shear wave in these planes is in the out-of-plane direction; in the $x-y$ plane, the shear wave polarisation is in the z-direction and in the $x-z$ plane, the polarisation is in the y-direction.

The radiation patterns in these planes exhibit a sinusoidal angular dependence; this is confirmed by figure 3.7 where $|\sin\theta|$ is also plotted. This is because the shear

wave point source is equivalent to the oscillatory rotation of a sphere around the x-axis. The angular displacement on the surface of the sphere, which represents the shear wave oscillation, is zero along the axis of rotation and increases at a rate proportional to the distance from the axis of rotation, leading to the sinusoidal angular dependence of the shear wave motion.

The longitudinal wave amplitude measured in each plane is shown in figure 3.5(b). In the $x-y$ and $x-z$ planes, the longitudinal wave exhibits uniform amplitude in all directions of -44 dB relative to the shear wave and in the $y-z$ plane, this reduces to -81 dB, which is negligible in all planes.

The error in arrival time of the shear wave relative to an analytical prediction in all directions is plotted in figure 3.5(c). The radial axis on the figure varies from 0 to 30 ns, which is equivalent to a range of 0 to 3% error relative to the analytical prediction. The worst case is in $y-z$ plane, which has a mean error of 23 ns, a range of 17 ns and shows two minima occurring at approximately 45° and 225°. Using the longest element edge length in the tetrahedral mesh and the time step of the model, an estimate of the velocity error can be calculated to be 1.24% [10], giving a time of flight error of 12 ns. This is the same order of magnitude as the error measured in figure 3.5(c). However, the estimation is based on an analysis in 2D therefore it is unsurprising that the time error measured here is different. Furthermore, the minima observed in figure 3.5(c) directly coincide with the minima observed in a study performed by Drozdz [10] for a mesh consisting of right scalene triangles at a very similar nodal density, which also suggests that the time of flight error is due to numerical dispersion in the model.

The deviation in wave velocity around the monitoring rings demonstrates the anisotropy of individual elements, which is due to small irregularities in the tetrahedra comprising the mesh [10]. The use of a structured mesh causes the velocity error to accrue, whereas an unstructured mesh would average out this result.

3.3.3 Discussion

Acceptability criteria of the amplitude and timing errors of the field radiated by a source used for beam forming can be derived from studies on phased array transducers. The cause of variation in amplitude and phase of the source field of an array element may be different to that of the field of an FE point source, however the

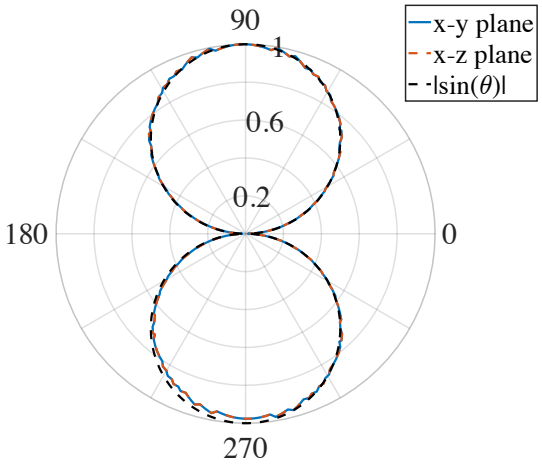


Figure 3.7: A plot of the shear wave amplitude measured on the monitoring rings in the $x-y$ and $x-z$ planes and the $|\sin\theta|$ function.

objective is the same. In a study performed by Duxbury *et al.* [106] it was shown that approximately a 20% variation in array element sensitivity is acceptable for beamforming in PA pulse echo ultrasonic testing; the results of this study are based on the premise that beam artifacts smaller than $-8\,\mathrm{dB}$ relative to the main beam are acceptable. This suggests that the variation of 10% over all angles observed in figure 3.5(a) in the plane of polarisation (the $y-z$ plane) should not have a significant impact on beam forming.

In the planes orthogonal to the plane of polarisation, i.e. the $x-y$ and $x-z$ planes, the variation in sensitivity was shown to approximately follow a $|\sin\theta|$ variation. Huygens' principle of superposition assumes the secondary sources have a constant amplitude in all directions; accordingly, the amplitude of the reconstructed field will be superposed with the sensitivity variation in the directions orthogonal to the plane of polarisation. To understand the impact of this sensitivity variation, the field from a typical ultrasonic probe is considered. It is common for a NDT inspection of NSRP components to use an ultrasonic probe with a circular diameter; the angle between the main beam axis and point at which the amplitude drops by $-6\,\mathrm{dB}$ can be estimated for a probe with a circular diameter by the equation [23]:

$$\sin\theta = 0.7\frac{\lambda}{D} \tag{3.3}$$

where D is the diameter of the probe, which is commonly 0.25" (6.35 mm). For typical shear wave velocity in stainless steel ($3110\,\mathrm{m\,s^{-1}}$) over a range of common

NDT inspection frequencies (1 to 5 MHz), the wavelength falls in the range 0.5 to 3 mm. This results in a range of beam divergence angles of 4° to 20° from the mean beam axis. Assuming that the main beam axis is equivalent to 90° in figure 3.5(a), the sensitivity variation over a 60° range around 90° is 15%, which is deemed to be an acceptable sensitivity variation on the basis of the study in [106].

A study by Duxbury [106], related to the work by Steinberg [111], investigated the effect of the firing delay on beam forming when using an ultrasonic array. The study demonstrated that the product of the −6 dB bandwidth of the input signal with the sampling frequency should have a maximum value of 0.03 for beam artifacts to be sufficiently suppressed. With knowledge of the −6 dB of the input signal it is therefore possible to estimate the maximum acceptable time of flight error, which is calculated as 22 ns.

The maximum time of arrival error relative to the analytical prediction for the shear wave point source in all planes was measured as 23 ns. However, this is the average error over all angles therefore the phase of the signal from every point source when reconstructing an incident wave will, on average, become shifted by this amount. A more influential parameter is the range of the time error over all angles, as this dictates the worst case phase variation when the source fields are superposed. The maximum range in time of flight was measured as 17 ns, which is acceptable according to the study by Duxbury.

3.3.4 Longitudinal Wave Point Source

The longitudinal wave point source is a simpler case than the shear wave point source. By definition the direction of polarization is parallel to the direction of propagation, which for a spherical wave is in the radial direction. To excite the point source, 8 neighbouring nodes with the smallest possible radius are again selected. Figure 3.8 shows the excitation direction used to generate a spherically expanding longitudinal wave. The displacement radiated by this source is measured on 3 circles that lie in each orthogonal plane centered on the point source with a radius of $4\lambda_L$. As there is no predefined direction of polarisation for the shear wave in this case, a residual amplitude is measured by subtracting the longitudinal wave component from the total measured field.

Stainless steel material properties are again assumed for the FE model, however

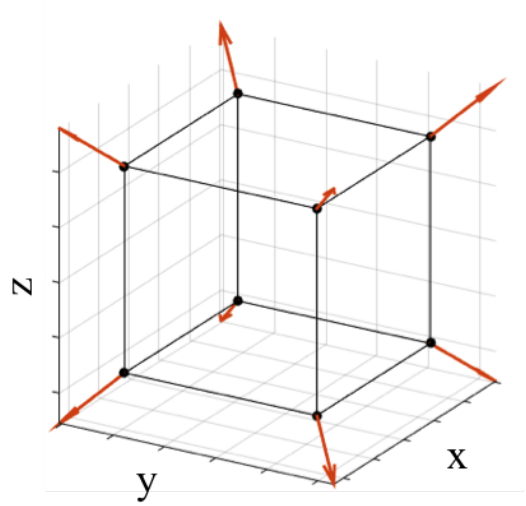


Figure 3.8: An approximate 3D longitudinal wave point source for an FE model. 8 neighboring nodes are excited in a radial manner to generate a spherically longitudinal wave.

in this case linear cubic elements are employed with an edge length of 100 µm. The signal applied to each node is again a 3 cycle 2 MHz toneburst. The increase in mesh density to approximately 30 elements per wavelength will reduce the velocity error of the FE model [10], therefore the time of flight calculation is omitted for brevity.

The results are plotted in figure 3.9. The definition of theta in each Cartesian coordinate plane is consistent with the plots in figure 3.6. It is clear from 3.9(a) that the longitudinal wave radiates uniformly in all directions, as expected. Furthermore, excellent modal purity is demonstrated by the negligible residual signal amplitude plotted in figure 3.9(b).

3.4 Beam Model Validation

In this section, both the Huygens-Fresnel model and the full source to defect domain coupling procedure is compared against the validated commercial software CIVA [112]. Firstly, a longitudinal incident wave model is validated and secondly the shear wave model is validated.

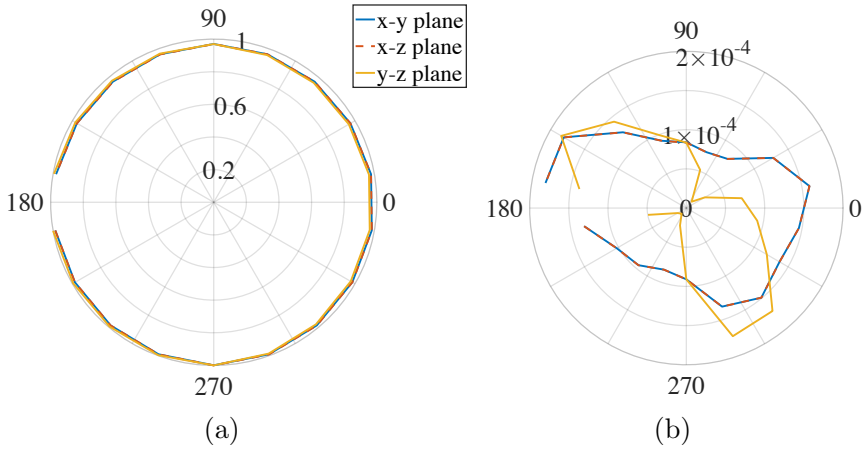


Figure 3.9: Polar plots of the results obtained from the monitoring circles in each orthogonal plane. (a) shows the normalised longitudinal wave amplitude and (b) shows the residual amplitude relative to the longtudinal wave.

3.4.1 Normal Incidence Longitudinal Wave

In this subsection, the Huygens-Fresnel model will be compared with CIVA [112], which has had extensive experimental validation. Following this the source to defect domain linkage will be compared directly to the Huygens-Fresnel model to ensure the incident wave is accurately reconstructed in the defect domain FE model.

A single element circular transducer with a 6.35 mm diameter is simulated in both the Huygens-Fresnel model and CIVA. The model setup is shown in figure 3.10. A 2 MHz, 3 cycle toneburst is used as the excitation signal in both models, which has a -6 dB bandwidth of 66%. Austenitic stainless steel properties are assumed (shear and longitudinal wave velocities are $3110\,\mathrm{m\,s^{-1}}$ and $5760\,\mathrm{m\,s^{-1}}$, respectively, and the density is $7800\,\mathrm{kg\,m^{-3}}$).

The incident wave fields are measured at the receiver plane which is located at

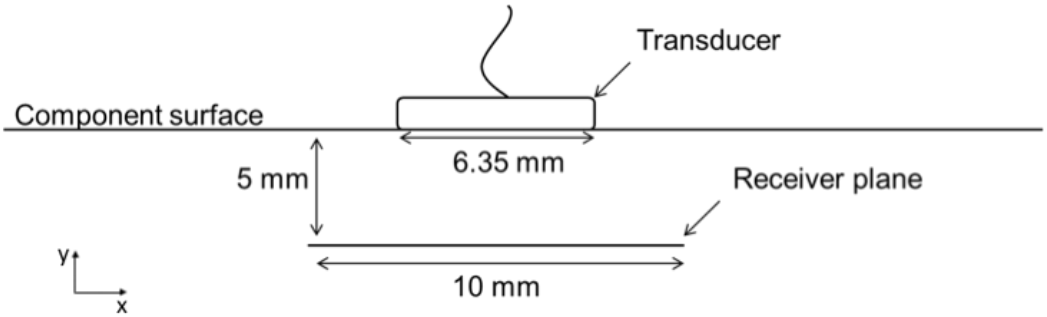


Figure 3.10: 2D schematic of the 3D model setup for the validation of the beam model against CIVA for simulating a normal incidence longitudinal wave.

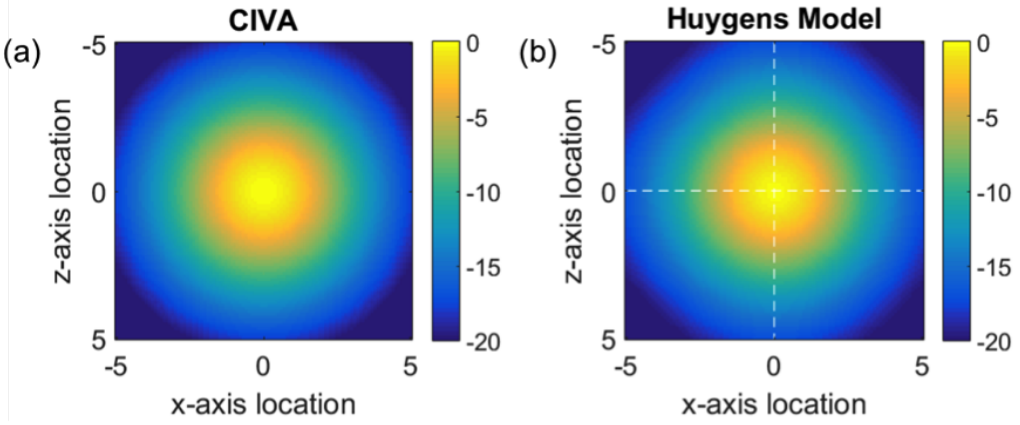


Figure 3.11: Beam profile measured at the receiver plane in (a) CIVA and (b) the Huygens model. The x_0 and z_0 lines to compare the echodynamic profile of the beams are marked in (b).

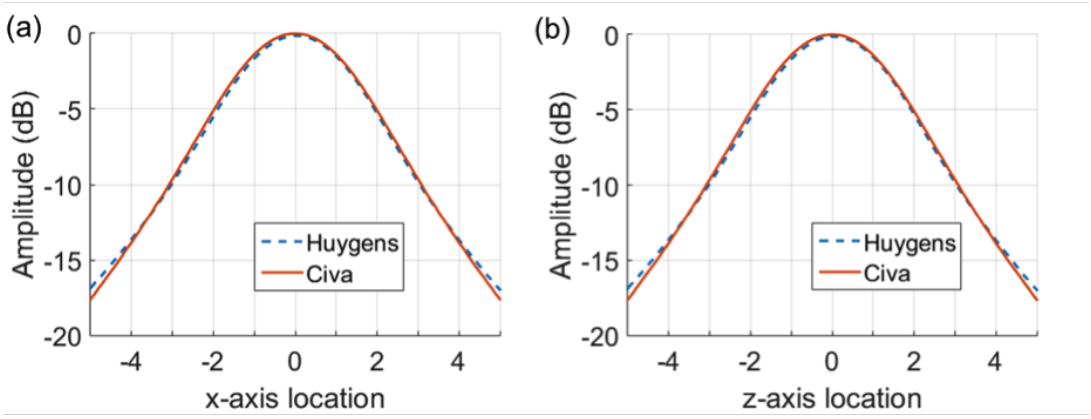


Figure 3.12: The echodynamic profiles of the normal incidence longitudinal wave along the (a) z_0 and (b) x_0 lines measure by the Huygens model and CIVA.

5 mm below the component surface and aligned with the centre of the transducer. The receiver plane is uniformly discretised at 100 µm. The time traces of the incident wave are measured at a 70 MHz sample frequency and the near field of the probe is 3.5 mm. In the Huygens model, the transducer surface is uniformly discretised at $\lambda_L/8$ and the transducer is assumed to be located within the component material. In CIVA, the beam computation module is used. The transducer is located at the inspection surface and is coupled to the component with water, which has a wave speed of 1483 m s^{-1}. In the simulation settings module, the accuracy parameter is set to 8. This parameter sets the spatial discretisation of the transducer and ranges from 1 to 10, 10 being most accurate at the cost of model run time. The recommended setting is 2, therefore the value chosen here provides a good trade off between accuracy and model run time.

Figure 3.11 contains the beam profiles measured at the receiver plane from both models. The beam profile is obtained by taking the maximum amplitude of the time trace that passes through each point on the receiver plane. The beam profiles are self-normalised and converted to a decibel scale. Visual comparison of the profiles shows that the Huygens model is in excellent agreement with CIVA. A closer comparison of the incident fields can be found by plotting the maximum amplitude along a line, which is often referred to as an echodynamic curve or simply an 'echodynamic'. For the comparison, the echodynamic curves of the beams are compared along the x_0 and z_0 lines (as illustrated in figure 3.11(b)) in figure 3.12. Excellent agreement is again observed between the two models.

The second step is to validate the linkage of the source domain Huygens model to the defect domain FE model. The model setup used to perform this validation is shown in figure 3.13. The incident wave parameters are consistent with those mentioned above. The longitudinal wave point sources (as illustrated in figure 3.8) are uniformly distributed across the excitation plane. The excitation signal applied to each point source is calculated by the Huygens model.

The wave radiated from the excitation plane in the FE model is measured at the receiver plane; the out-of-plane extent of the receiver plane is equal to the in-

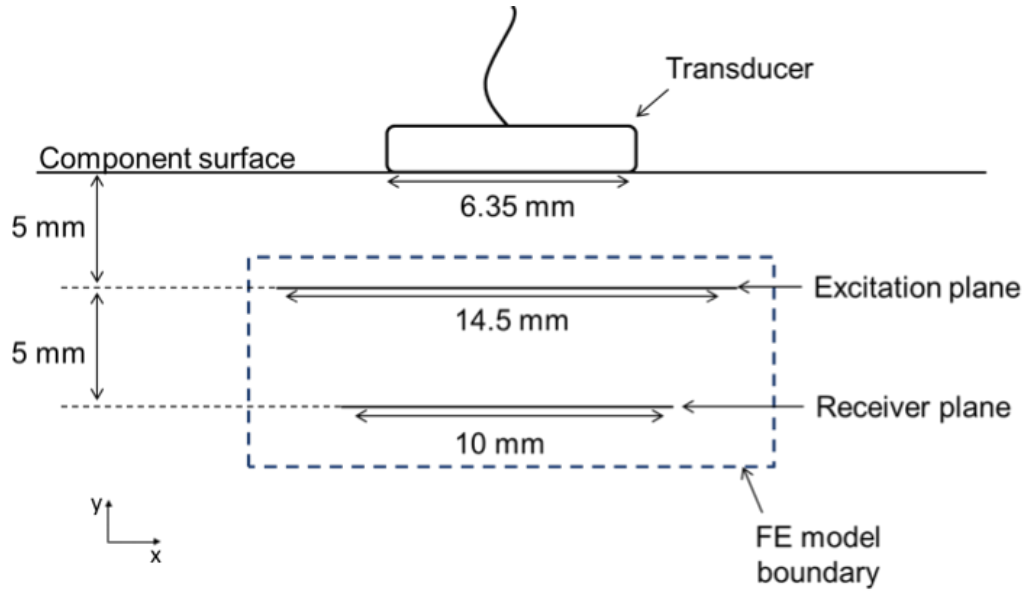


Figure 3.13: 2D schematic of the 3D model setup for the validation of the source to defect domain linkage against the Huygens model for simulating a normal incidence longitudinal wave.

plane extent shown in figure 3.13. For validation, the Huygens model is also used to calculate the incident wave at the receiver plane and the beam profiles are compared in figure 3.14. The echodynamic curves along the x_0 and z_0 lines are also compared in figure 3.15. Excellent agreement is observed in both figures.

3.4.2 Normal Incidence Shear Wave

For the shear wave case, the source to defect domain linkage is initially compared to the Huygens-Fresnel beam model. Due to the variation in sensitivity of the point sources demonstrated in subsection 3.3.2, the validation case also considers the accuracy of the procedure when there is a level of mis-orientation between the main axis of the incident wave and the excitation plane. Secondly, a comparison of the full procedure to CIVA is given.

A schematic of the model used to validate the source to defect domain linkage process is given in figure 3.16. The shear wave point sources are distributed uniformly over the source plane within the FE model and are separated by 150 µm, which is twice the element size. The parameters of the FE model are consistent with those given in table 3.1. The Huygens-Fresnel beam model is employed to calculate the incident wave field displacement at the central location of each approximate point source and the calculated time traces are used as excitation signals in the FE model. The transducer simulated by the beam model is circular, has a diameter of 6.35 mm and is in direct contact with the surface of the component. The incident

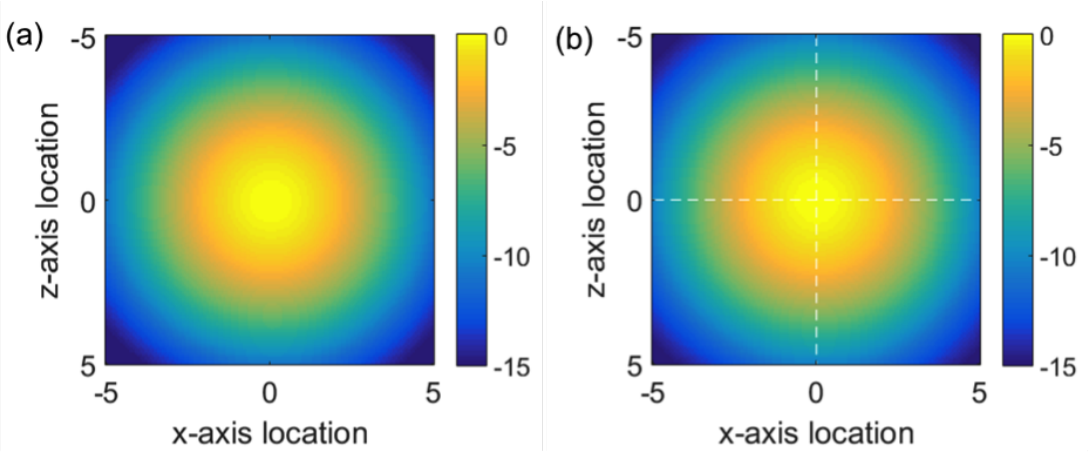


Figure 3.14: Beam profile measured at the receiver plane by (a) the Huygens model and (b) in the FE model. The x_0 and z_0 lines to compare the echodynamic profile of the beams are marked in (b).

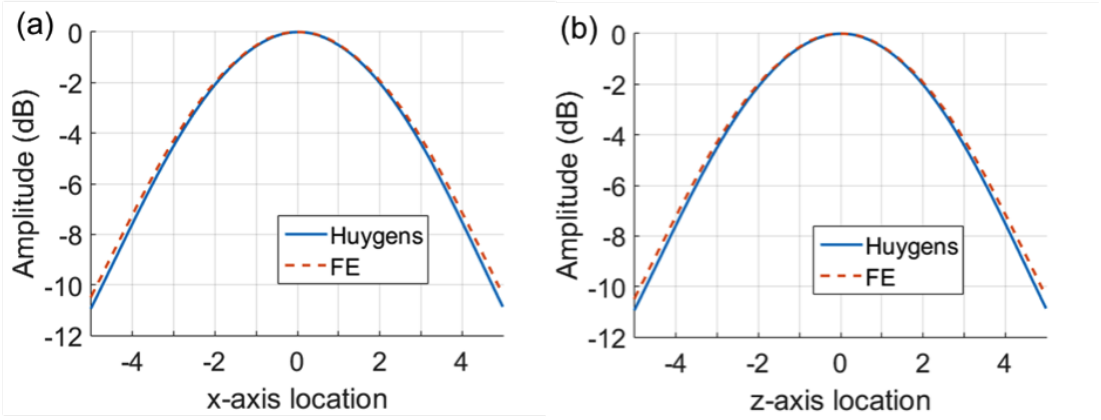


Figure 3.15: The echodynamic profiles of the normal incidence longitudinal wave along the (a) z_0 and (b) x_0 lines measured by the Huygens model (solid blue) and the FE model (broken red).

wave is a 2 MHz 3 cycle toneburst. The incident wave generated in the FE model is recorded at the receiver plane; both the source and receiver plane have an $x - y$ extent of 9.3×9.3 mm.

As depicted by figure 3.1, the source plane may not be perpendicular to the main beam axis. In order to examine the ability of the approximate point sources to correctly steer the beam, the source plane is rotated about its centre at increments of 5° between 0 and 60°. The polarization of the point sources is shown in figure 3.16; the shear sources are only required to steer the beam in the plane of polarization shown in the figure. The incident field measured at the receiver plane in the FE model will be compared to the field calculated by the Huygens-Fresnel model over the same locations.

The results for the 0° shear wave case are plotted in figure 3.17. To create the images in the figure, the maximum amplitude from the time traces for each point on the receiver plane was measured. The results are normalised and converted to a decibel scale. Figure 3.17(a) displays the results from the Huygens model and figure 3.17(b) displays the results recorded from the FE model. The images shown in the figure are in excellent agreement. The incident field shown in the images is characteristic of a field radiated by a circular transducer in the far field. The near field of this transducer is equal to 6.5 mm, which therefore means the source plane in the FE model lies beyond the near field. As Huygens' principle is used to excite the wave in the FE model, it will also be accurate inside the near field of the transducer.

For a closer comparison, two echodynamics are plotted along lines parallel to

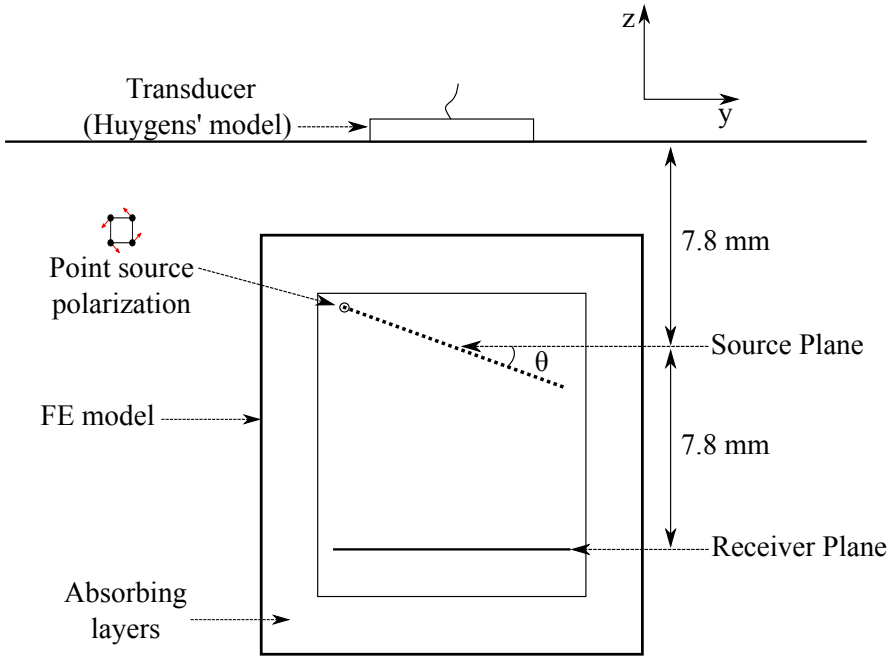


Figure 3.16: Schematic of the modelling process used to validate the forward process for the hybrid technique.

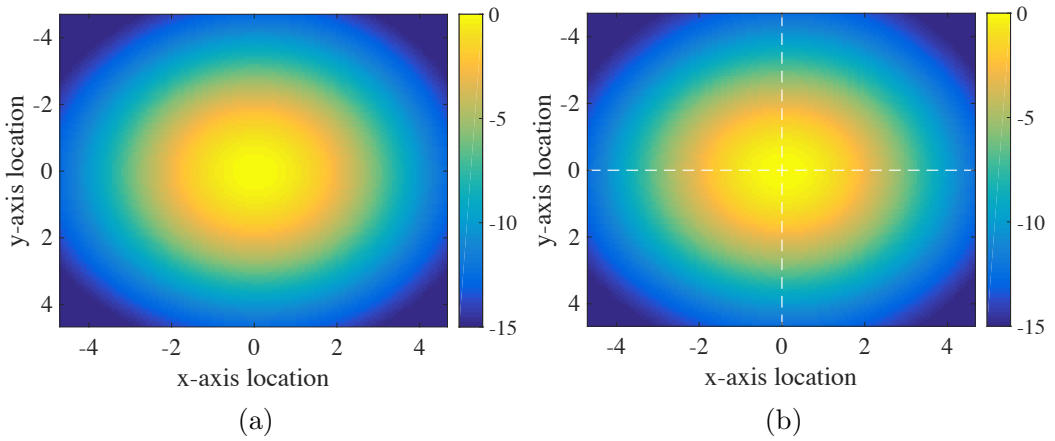


Figure 3.17: Images of the maximum amplitude of the incident wave recorded at the receiver plane. (a) is calculated directly by the Huygens beam model and (b) is measured from the FE model by exciting a plane of shear wave point sources. The white lines in (b) show the locations of the echodynamic curve measurements in figure 3.18.

the x and y-axes and passing through the maximum point in the wave field, as shown by the white lines on figure 3.17(b). The results are plotted in figure 3.18, along with the echodynamics for a selection of the rotated source planes.

It is clear from the figures that the echodynamics are in good agreement, suggesting that the rotation of the source plane has little effect on the amplitude of the reconstructed incident field.

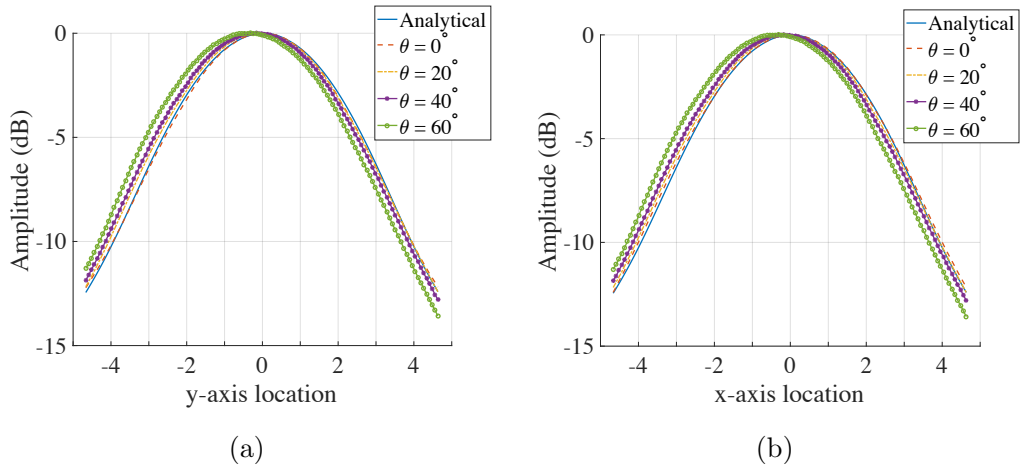


Figure 3.18: Echodynamic curves of the incident wave field measured parallel to the x-axis (a) and y-axis (b). The results from the Huygens model are plotted in both, along with the results measured from the FE model in figure 3.16 for a range of source plane angles.

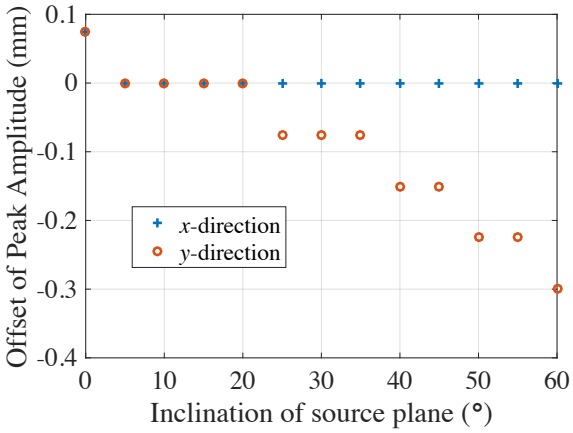


Figure 3.19: Offset of location of maximum of incident wavefield.

It is also clear from the figures that there is a level of misalignment between the echodynamic curves. In figure 3.19, the offset between the analytical and FE results for the location of the peak amplitude of the incident wave in both the x and y-direction is plotted for all angles of source plane inclination. There is an initial offset of 75 µm between the FE model results and the analytical prediction for the location of the incident field maxima in both axes. This offset reduces to zero for both the x and y-axis for increasing inclination of the source plane. As the inclination of the source plane increases past 20°, the offset in the y-direction increases, with step changes of 75 µm up to 300 µm. The step is because the spatial

discretisation of the receiver plane is equal to the element size of the model, which is 75 µm.

It is likely that the offset of the peak amplitude location relative to the analytical prediction is caused by differences in the interference pattern of the source fields as a result of the wave speed errors in the field radiated by the approximate point sources. An offset of 0.3 mm is less than the offset specified in the British Standard BS EN 12668 [113] for an acceptable deviation of 1 mm between the geometrical centre or index point of an ultrasonic transducer and the measured beam centre point. This suggests that the offset measured at a source plane inclination angle of 60° is acceptable, however the best performance of the point sources occurs when the source plane is orientated perpendicular to the main beam axis.

3.4.3 Angled Incidence Shear Wave

For the angled incidence shear wave, the incident wave excitation in the FE model is directly compared with the output from CIVA. In this instance, the source domain is also simulated using CIVA. This section therefore provides validation of the accuracy of the linkage between the source domain and the defect domain using a point source approach.

The model setup is shown in figure 3.20. A 6.35 mm diameter circular transducer is mounted to a Perspex wedge to generate a 2 MHz, 45° shear wave within an austenitic stainless steel test piece. The transducer is mounted at an angle of 37.5° to the normal to generate the refracted wave at the correct angle. The incident wave

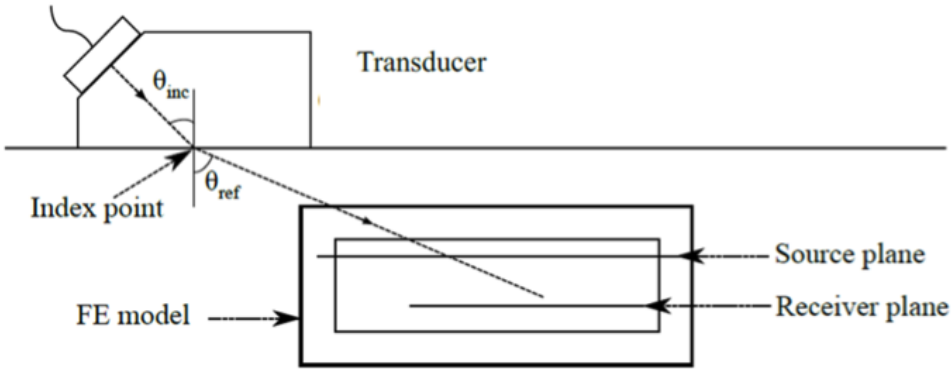


Figure 3.20: 2D schematic of the 3D model setup for the validation of the source to defect domain linkage against CIVA for simulating an angled incidence shear wave.

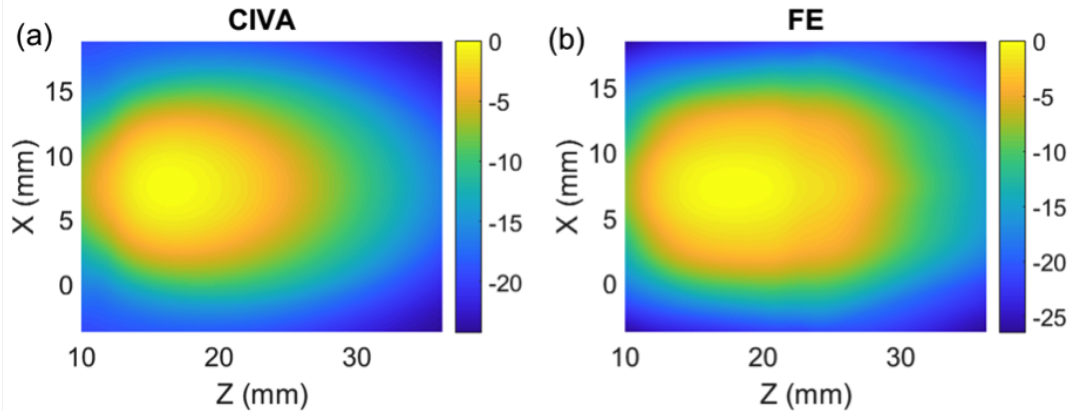


Figure 3.21: Beam profile measured at the receiver plane by CIVA (a) and in the FE model (b).

is excited inside an FE model at the source plane, shown in figurre 3.20. The source plane is made up of an array of shear wave point sources and the point sources are uniformly distributed across the excitation plane.

CIVA is also used to measure the beam profile at the receiver plane, which is given in figure 3.21(a). The beam profile generated in the FE model is given in figure 3.21(b). The results show good agreement. There is an over-estimation of the beam width beyond approximately 20 mm in the z-direction. This can be clearly observed on the echodynamic curves shown in figure 3.22. Figure 3.22(a) shows that the beam profiles are in good agreement until the maximum amplitude of the incident wave occurs. There is an offset of 1.78 mm in the location of the maxima between FE and CIVA in the z-direction. This is likely to be as a result of amplitude and phase variations in the source field radiated from the shear wave point sources used to excite the incident wave in the FE model. The overall profile of the beam is however in good agreement with CIVA.

In the x-direction, the echodynamics in figure 3.22(b) show excellent agreement. There is a small offset of 0.3 mm of the location of the maxima predicted by each model. The error has reduced in this dimension as the point sources are not required to steer the beam in this direction and therefore the results are less affected by amplitude and phase variations in the field radiated by the point sources.

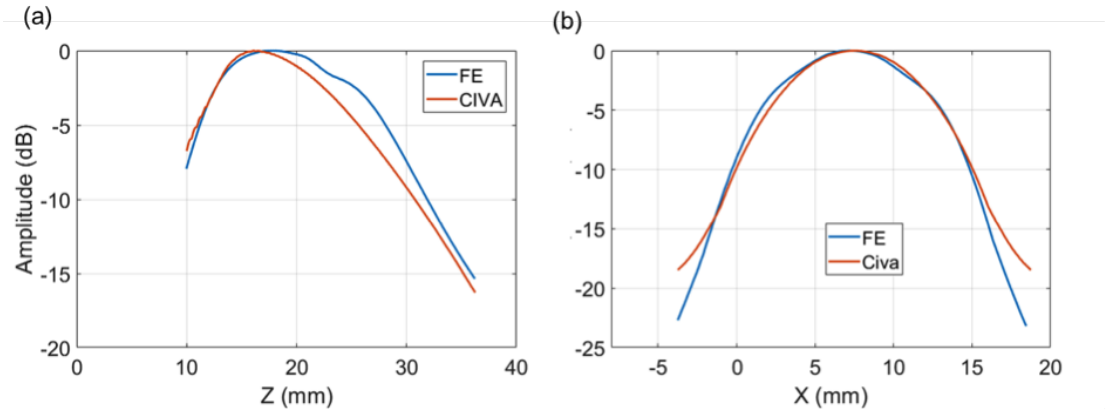


Figure 3.22: Echodynamic profiles of the incident beam excited in the FE (blue) and CIVA (red) models. (a) is measured at the location of the maximum in the x-axis and (b) is measured at the location of the maximum in the z-axis.

3.5 Conclusions

The accurate simulation of ultrasonic transduction systems is an integral part of an ultrasonic inspection model. Previous applications of the hybrid method have used an FE model to simulate a transduction system. However, it was highlighted that a semi-analytical beam model would offer a more computationally efficient approach and therefore the Huygens-Fresnel beam model was selected. However, problems arise when attempting to re-excite the predicted incident wave field within an FE model because there is no information on the direction of required loading. This chapter therefore investigated the accuracy of generating the incident field by exciting a series of secondary point sources in the FE model.

The use of point sources in 2D FE models for ultrasonic NDE is common place within the literature. However this approach has not been previously demonstrated in 3D, specifically for the generation of an incident shear wave field. Section 3.3 investigated the variation in amplitude of the field radiated from a polarised approximate FE shear wave point source, as well as comparing the time of flight to an exact analytical prediction. The amplitude variation in the plane of polarisation of the shear wave and the orthogonal planes was deemed acceptable by comparison to studies on phased array transducer element variation. The maximum variation in time of arrival was also calculated to be within the tolerance for typical array beamforming. The study was repeated for the simpler longitudinal wave point source case and showed uniformity of amplitude in all directions and good modal purity.

Validation of this approach showed excellent agreement for the normal incidence

longitudinal wave beam profile against both CIVA and the Huygens-Fresnel model. The ability of the shear wave point sources to handle off-axis excitation was studied and found excellent agreement at normal incidence, whilst for angles of inclination up to 60° an offset of 0.3 mm was found. For the angled incidence shear wave, a comparison to CIVA demonstrated good agreement. The profiles across the x-axis of the model showed excellent agreement. However, the profile across the z-axis showed that the FE model over-estimated the beam width and there was an error of 1.8 mm in the predicted maximum of the beam profile. This error was attributed to phase and amplitude errors in the field radiated by the shear wave FE point source.

This method of excitation is limited to a single wave mode due to the nature of the Huygens-Fresnel model. If multiple wave modes are required in a single model, it would be feasible run the Huygens-Fresnel model multiple times and superpose the excitation in FE, however this has not been demonstrated here. This is possible since no mode conversion can occur in the free space region, allowing the modes to be treated separately. Furthermore, the errors in phase of the fields radiated by the point sources observed in this chapter have been attributed to the inherent anisotropy of the tetrahedral elements. It is feasible that the errors could therefore become reduced if the mesh density of the FE model is increased, however this is at the cost of computational efficiency. There is further work necessary to optimise the use of excitation surfaces in the hybrid method. In particular, the optimal size of the excitation surfaces is likely to depend on the beam width at the point of excitation however the surface would need to be large enough to avoid edge effects from truncation.

Chapter 4

A Hybrid Method for Surface-Breaking Defects

Despite the great potential of the hybrid simulation methodology, little attention has been given to utilising it for to simulate the ultrasonic inspection of surface-breaking defects. In this chapter, a methodology to simulate the ultrasonic inspection of complex surface-breaking defects using a 3D hybrid model is presented.

4.1 Introduction

For the types of defects of interest to this work, the distance between the ultrasonic transducer and the defect is largely dependent on the wall thickness of the component and can be many orders of magnitudes larger than the ultrasonic wavelength. Hence, to simulate an inspection of this type in its entirety in three dimensions is often infeasible using a full numerical method and a hybrid approach is extremely desirable. Hybrid models proposed by other authors have also considered similar ultrasonic inspection scenarios, for example [12, 92]; however, there are limited studies in the literature that demonstrate the validity of 3D hybrid techniques when simulating the inspection of components containing surface-breaking defects.

In the following section, details of the methodology for simulating an ultrasonic inspection using the hybrid approach are presented. Numerical verification and experimental validation are then given in section 4.3 and 4.4, respectively. In addition to the validation, section 4.5 presents a study into the ultrasonic attenuation due to surface roughness on surface-breaking defects in three dimensions. The work

reported in this chapter has been written up as a journal paper and published in NDT & E International [P1].

4.2 Hybrid Model Methodology

A variety of ultrasonic inspection techniques that are commonly used in the detection and sizing of surface-breaking defects were discussed in section 2.2. In this work, the methodology used to apply the hybrid technique to the simulation of surface-breaking defect inspections focuses on the angled shear wave inspection described in subsection 2.2.1. This is not only because this method is very common, but also because it captures the simulation of both the interaction of the incident wave with the backwall and the defect through the corner echo and the interaction of the incident wave with the tip of the defect though the tip diffraction mechanism. It is therefore feasible to suggest that the methodology can be extended to the ToFD and PA inspection techniques with little complexity. Although the longitudinal creeping wave inspection is not considered directly, a validated methodology to simulate the angled shear wave inspection would provide a sound basis with the potential to be extended to other inspection techniques.

In the hybrid model methodology outlined in subsection 2.5.3, a generic inspection is decomposed into the source domain and defect domain and they are linked by the hybrid interface. For clarity, the linkage of the source to the defect domain is referred to as the forward process, and the reverse as the backward process. The source domain procedure has been described in chapter 3 therefore this chapter will focus on the defect domain and the backward process.

4.2.1 Defect Domain

The ultrasonic scattering within the defect domain is simulated using the accelerated GPU based FE solver Pogo [80]. The aim is to reduce the size of this FE domain as much as possible, due to the inherent computational memory requirements; however, the model must be large enough such that all scattering mechanisms are captured. As previously described, the corner echo scattering relies upon the specular reflection from the backwall and the defect; therefore, an area of the backwall must be present in the FE model to accurately simulate this mechanism. With knowledge

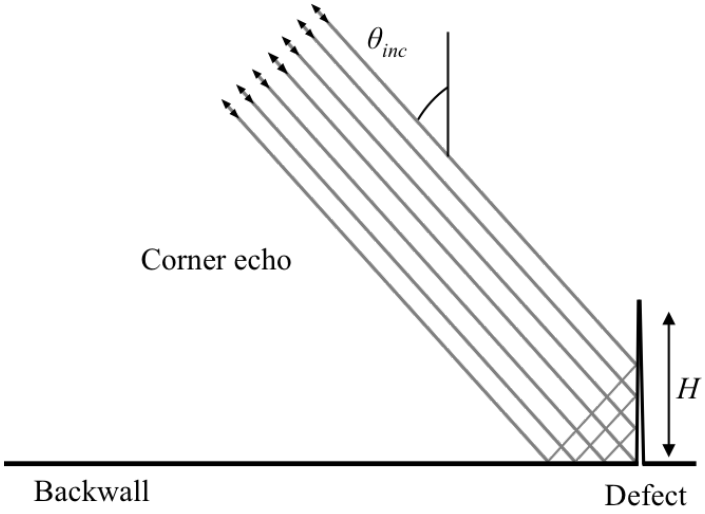


Figure 4.1: Schematic of the corner echo scattering from a surface-breaking defect.

of the defect size, orientation and angle of incidence, the minimum required area of backwall can calculated through trigonometry using a simple ray tracing approach. For a perpendicular defect this leads to the simple relation:

$$BW = H \tan \theta_{inc} \tag{4.1}$$

where H is the through-wall height of the defect as shown on figure 4.1 (repeated from section 2.2.1 for clarity), θ_{inc} is the incident angle of the ultrasonic wave, also shown in figure 4.1, and BW is the backwall extent required to capture the corner echo. In practice, this calculation is an under-estimation because divergence of the incident wave will cause the angle of incidence to change. The beam divergence is dependent on the parameters of the transduction system and component material and can be calculated analytically for simple transducers, or by a semi-analytical beam model for more complex systems. With knowledge of the divergence angle from the mean beam axis, θ_{div}, the argument of the tangent function in equation 4.1 can be replaced by $\theta_{inc} + \theta_{div}$.

4.2.2 Backward Process

Once the scattering from the defect is simulated in the FE model, the propagation through the bulk elastic medium back to the source domain is handled by the hybrid interface. The calculation performed within the hybrid interface is based on the integral representation given by equation 2.48. The equation is repeated here for

clarity:

$$\phi(\mathbf{r_2}) = \int_S [\phi(\mathbf{r_1})\nabla G_\phi(\mathbf{r_2}|\mathbf{r_1}) - G_\phi(\mathbf{r_2}|\mathbf{r_1})\nabla\phi(\mathbf{r_2})] \cdot \mathbf{n}\mathrm{d}S \tag{4.2}$$

where all repeated variables hold their original definition and S is the surface enclosing the defect domain.

Equation 4.2 requires the wave potentials to be measured over the boundary of the defect domain, defined by the surface, S, which is referred to as the monitoring surface. The potentials can be calculated from various field quantities; here, they are computed from stress and displacement, which are common outputs of FE solvers, as in [95]. In general, an FE solver will compute the total field, which contains components of both the incident and scattered fields. However, the wave potential must be calculated from the scattered field; by assuming material linearity, the scattered field can be calculated from equation 2.24. A second FE model without the defect present is required to provide the incident field on the monitoring surface. In previous work, this surface has been defined as a rectangle or cuboid enclosing the defect [14, 95]. However, for the case of a surface-breaking defect, the backwall can be considered to be a semi-infinite stress-free boundary and therefore cannot be enclosed.

Because of the assumption of material linearity, the monitoring surface must not impede the scattered field or cause further scattering. Therefore, the surface cannot lie on the crack face or along the backwall. Alternatively, it is possible to

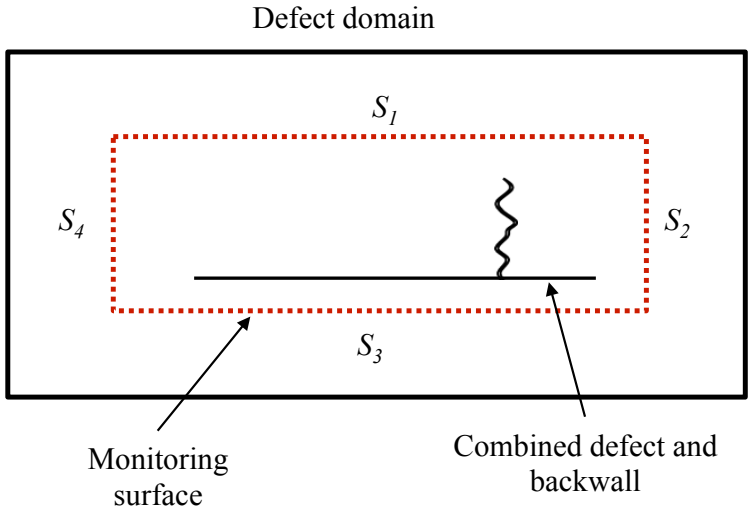


Figure 4.2: A truncated backwall is combined with the defect into a single scatterer. The hybrid monitoring surface encloses the scatterer within the defect domain.

combine the defect and backwall into a single scatterer; by using equation 4.1, we can approximate the section of backwall required for the simulation. The combined defect and backwall can then be enclosed by the monitoring surface, as shown by figure 4.2.

From the figure we notice that the wave potential that would be simulated on the bottom of the monitoring surface (S_3) and a section of the sides (S_2 and S_4) of the monitoring rectangle are unphysical; in reality, no wave field will be present there. Furthermore, truncation of the backwall would induce diffraction effects which would not be present in a real inspection. To overcome this, it is possible to break down the integral representation in equation 4.2 into a summation of 4 integrals, each representing the integration along a separate side of the monitoring surface. In 2D, this becomes:

$$\phi(\mathbf{r_2}) = \int_S f(\phi, G_\phi)\cdot\mathbf{n}\mathrm{dS}_1 + \int_S f(\phi, G_\phi)\cdot\mathbf{n}\mathrm{dS}_2 + \int_S f(\phi, G_\phi)\cdot\mathbf{n}\mathrm{dS}_3 + \int_S f(\phi, G_\phi)\cdot\mathbf{n}\mathrm{dS}_4 \tag{4.3}$$

where

$$f = [\phi(\mathbf{r_1})\nabla G_\phi(\mathbf{r_2}|\mathbf{r_1}) - G_\phi(\mathbf{r_2}|\mathbf{r_1})\nabla\phi(\mathbf{r_1})] \tag{4.4}$$

and S_α denotes the section of the surface of integration, with respect to the labels given in figure 4.2.

We now make use of our prior knowledge of the angled shear wave inspection setup; in subsection 2.2.1 an optimal incident angular range for the angled beam shear wave inspection was calculated to be between 32° and 58°. Consequently, the field scattered through the corner echo mechanism will propagate back along this direction. It is therefore possible to increase the size of the monitoring surface, S_1, such that the relative magnitude of the scattered wave which passes through surfaces S_2, S_3 and S_4 will become negligible. Equation 4.3 can then be reduced to:

$$\phi(\mathbf{r_2}) \approx \int_{S_1} f(\phi, G_\phi)\cdot\mathbf{n}\mathrm{dS}_1 \tag{4.5}$$

Hence, the wave potentials can be calculated over a monitoring surface which lies above the defect and backwall, illustrated in figure 4.3. The backwall now comprises boundary of the defect domain model, removing the edges of the truncated backwall shown in figure 4.2 that may cause spurious diffraction signals. As will be discussed in the next section, absorbing boundary conditions are applied to the boundary of

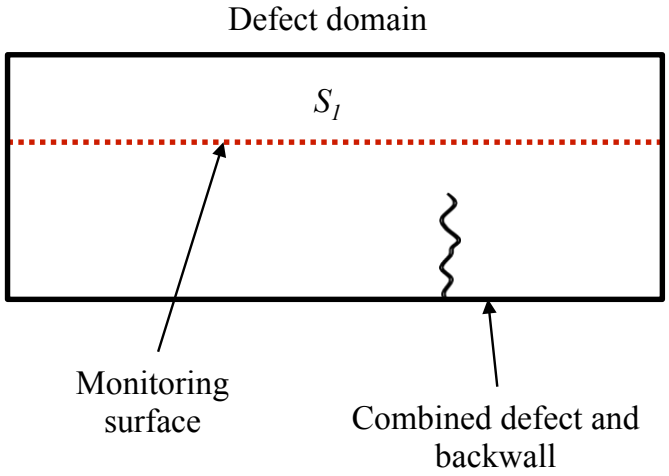


Figure 4.3: The hybrid monitoring surface is reduced to a single edge.

the defect domain FE model. In this case, the absorbing boundaries will not be applied to the model boundary representing the backwall.

A limitation of this approach is that a component of the secondary scattering phenomena, such as the diffracted and surface waves, will not propagate through surface S_1 and will lead to an inherent error. However, the amplitude of this secondary scattering relative to the scattered wave measured by S_1 will be small and should not have a significant effect on the overall result. In this case, a relatively simple case to demonstrate the methodology has been used. Once the validity of this approach has been confirmed, it will be possible to move on to other cases, such as more complex defects and other inspection configurations, where further consideration and validation will be required to ensure the technique remains accurate and to minimize coupling artefacts.

4.3 Numerical Verification

In this section, the accuracy of the hybrid technique for simulating an ultrasonic inspection of a surface-breaking defect is assessed by comparison to an equivalent full numerical model. To make this comparison possible, the separation between the source and the defect is kept small. Firstly, the comparison is shown for a surface-breaking defect with simple morphology and secondly a rough surface is applied to the defect to demonstrate the performance of the hybrid technique when a realistic defect is present. For brevity, the forward process from the source domain to the

defect domain is omitted from the verification because it is only the performance of the hybrid interface to accurately propagate the complex scattering in the defect domain to the source domain that is of importance in this section.

The same FE model is used for both the hybrid model and the verification model therefore the hybrid monitoring surface is located within the verification model, as shown by figure 4.4. A plane shear wave is generated on a surface at a height of 13.6 mm ($8.75\lambda_S$) above the backwall by applying a Hann-windowed 5 cycle tone burst with a 2 MHz centre frequency to all nodes. Appropriate time delays are applied to the excited nodes to ensure the wave travelled at a 45° incident angle. The defect in each validation case is a 3×3 mm square with an opening of 7.5 µm and is connected to a stress-free boundary representing the backwall of the component. Absorbing regions are applied around the FE domain to suppress unwanted reflections polluting the domain. The SRM absorbing layers are employed here; by optimising the material properties of the SRM, satisfactory absorption can be achieved within one wavelength [82]. The dimensions of the entire domain are $13.4 \times 17.3 \times 24$ mm and an element size of 75 µm ($\approx \lambda_S/21$) is used. Stainless steel material properties are again assumed for this model.

The minimum backwall extent required to simulate the corner trap is calculated

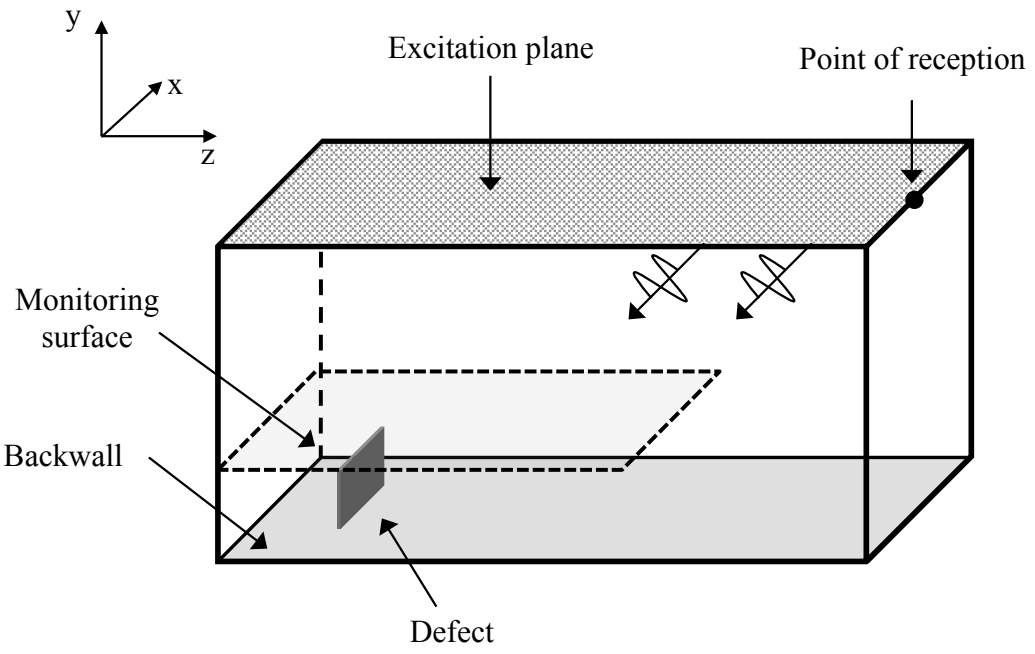


Figure 4.4: Schematic of the numerical validation model including an illustration of the monitoring surface used for the hybrid calculation.

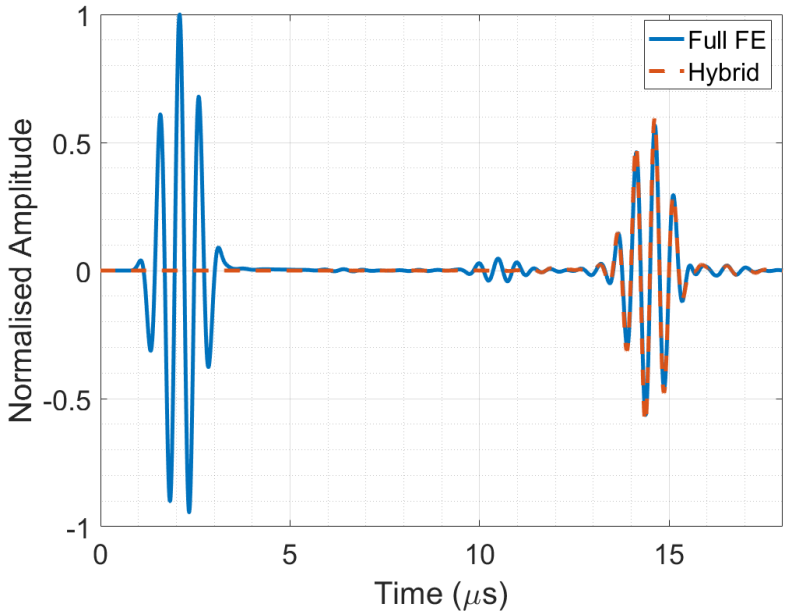
as 3 mm, according to equation 4.1; beam divergence does not apply here as plane wave incidence is used. The extent of the hybrid monitoring surface is larger than this, in order to satisfy equation 4.5. The dimensions of the monitoring surface in the $x-z$ plane are 6×12 mm, which is deemed to provide sufficient coverage of the scattered wave, and it is located at 4.5 mm above the backwall. The displacement resulting from the scattered shear wave is compared at a point of reception, which is aligned with the centre of the defect in the x-direction and located at a distance of 15.6 mm in the y and negative z-direction.

To generate an FE mesh for the entire model domain, a mixed meshing procedure using linear tetrahedral elements is employed. A volume surrounding the defect with dimensions $4.5 \times 3.75 \times 4.5$ mm is meshed in ABAQUS CAE (Dassault Systmes Simulia Corp., Rhode Island, US) using the free meshing tool, with a seed size of 75 µm. A structured tetrahedral mesh is then appended to provide a mesh for the remaining model domain using a custom algorithm in MATLAB. as described in section 3.3.1.

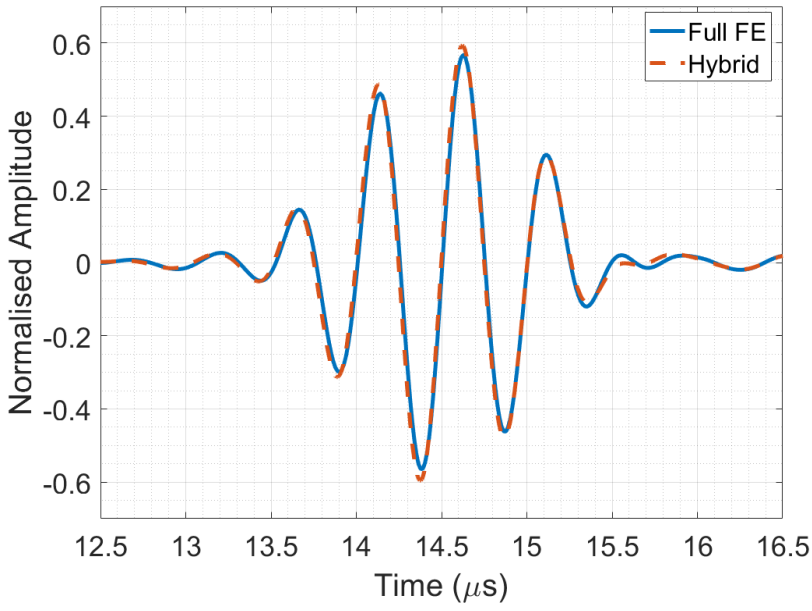
4.3.1 Smooth Notch

The time history of the measured scattered displacement from each model is plotted in figure 4.5(a). The initial pulse in the full FE data is the excitation signal; both data sets are normalised to this. A low amplitude signal that arrives at approximately 10 µs is an artifact of the incident wave excitation and corresponds to a 0° wave reflection from the free surface ($27.2\,\text{mm}/3110\,\text{m}\,\text{s}^{-1} = 8.7\,\mu\text{s}$). This is not present in the hybrid prediction because it does not pass through the hybrid monitoring surface.

The last signal in the time histories corresponds to the reflection from the defect and it is the signal of primary interest. It can be seen to be in good agreement for both models. Figure 4.5(b) shows a more detailed comparison of the reflected signals, where excellent agreement is observed. There is a small but observable difference between the signal amplitudes. The difference between the maximum amplitude of each signal relative to the FE prediction is −30 dB, which is negligible and is probably due to a numerical rounding error in the hybrid calculation. A very small phase delay can also be seen between the hybrid and FE cases; the discretisation error of FE will cause the waves in the full FE model to travel slightly slower than



(a)



(b)

Figure 4.5: A comparison of (a) the recorded time history from each model and (b) the waveform of the scattered wave.

they do in the hybrid model [10].

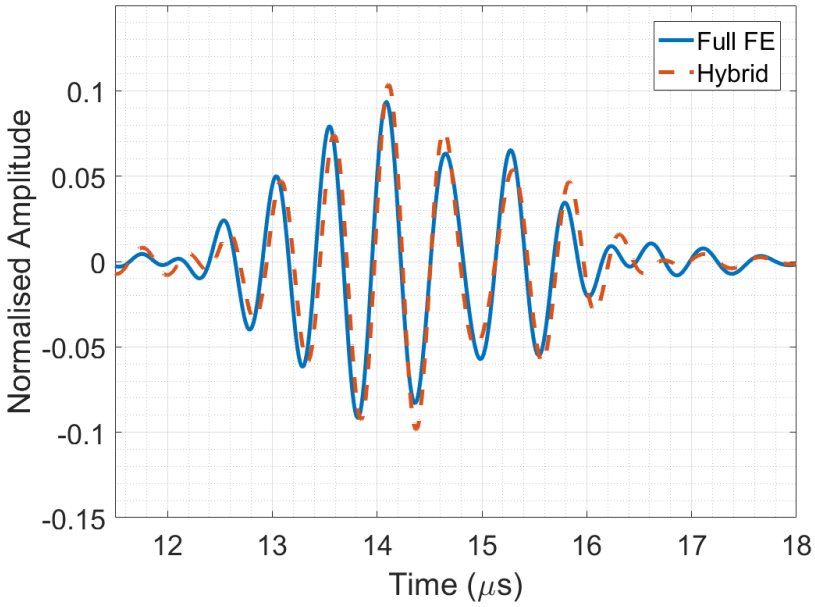


Figure 4.6: A comparison of the scattered wave from the rough defect predicted by each model.

4.3.2 Rough Notch

For the simulation of a complex defect, the defect surface is assumed to be randomly rough and is described using a Gaussian statistical model, in line with the literature [7, 53]. The Root Mean Square (RMS) height and correlation length required for the Gaussian model are both chosen to be 300 µm ($\approx \lambda_S/5$); this is a high level of roughness in comparison to typical welding, forging and thermal fatigue defects found in the nuclear sector and therefore provides a good test of the model.

A comparison of the reflection from the defect predicted by each model is shown in figure 4.6. The signal is more complex, in comparison to the smooth defect case, due to the presence of defect roughness and has also been significantly attenuated. The error between maximum amplitude of signal predicted by the hybrid model relative to the FE prediction is now −23 dB. However, this increase is due to the attenuation of the reference FE signal; the absolute difference in signal amplitude has decreased by an amount that is similar to the attenuation in signal amplitude between the smooth and rough defect cases. In general, good agreement is observed between the predicted waveforms.

An important measure from the hybrid model is the predicted attenuation of the defect response due to the surface roughness. For the full FE model, this is calculated to be −15.9 dB and for the hybrid model, it is −15.4 dB. These values

are in good agreement, which gives confidence in the use of the hybrid model to simulate the scattering from surface-breaking defects with complex morphology.

4.4 Experimental Validation

This section reports on the experimental validation of the hybrid model for simulating an ultrasonic inspection of a surface-breaking defect. For the validation, experimental results were acquired by performing a single pulse-echo line scan over a test piece containing a smooth surface-breaking notch.

4.4.1 Experiment

The test piece chosen for the validation was a 15 mm thick stainless-steel block that contains an artificial notch. The notch is smooth and has a surface length (dimension parallel to the backwall) of 3 mm, a through-wall height (defined as H in figure 4.1) of 1.5 mm and an opening of 0.3 mm. A wedge-mounted circular broadband transducer [wedge: GE 210-852-110 and transducer: GE SB1391] with a diameter of 0.25 inches (6.25 mm) is used to generate a shear wave at an incident angle of 45° and centre frequency of 5 MHz within the stainless-steel sample. The transducer is excited by applying a rectangular voltage signal with a pulse width 100 ns, equal to half the period at the centre frequency of the incident wave. The transducer is aligned with the centre of the defect and scanned in a lateral direction, illustrated by figure 4.7. The reflections from the defect are measured using the same transducer in P-E mode at increments of 0.2 mm. A single channel of a PeakNDT FMC micropulse system is used to acquire the data at a sampling frequency of 100 MHz. As the surface length of the defect is less than the transducer diameter, one scan was sufficient to provide full coverage of the defect.

The results are plotted in figure 4.11(b), which shows an image of the defect that has been generated from the time histories recorded in the scan. This is commonly known as a B-scan image and is formed by converting the time axis of the time histories measured at each scan increment into a distance of propagation. With knowledge of the incident angle and wave speed of the material, each data point is assigned to a pixel location on the image. The edge of the sample was used as a reference point for the x-axis of the image; the defect is located at 80 mm from

this reference point. The data are normalised to maximum amplitude in the image and are converted to a decibel scale. The wave speed of the material was calculated from the material properties of stainless steel and the time delay due to propagation through the wedge has been accounted for in the image.

4.4.2 Hybrid Simulation

The source domain and forward process are simulated using the beam model described in chapter 3. The beam model was solved for the bandwidth of a Hann windowed 3-cycle tone burst and converted into the time-domain using the Inverse Fast Fourier Transform (IFFT). A schematic of the FE model used to simulate the scattering from the defect in the defect domain is given in figure 4.9. The excitation plane represents the selection of nodes in the model that are excited as point sources (figure 3.3) using the phase and amplitude calculated by the beam model. The conclusion drawn from subsection 3.4.2 recommended that for the most accurate incident wave reconstruction the excitation plane should be perpendicular to

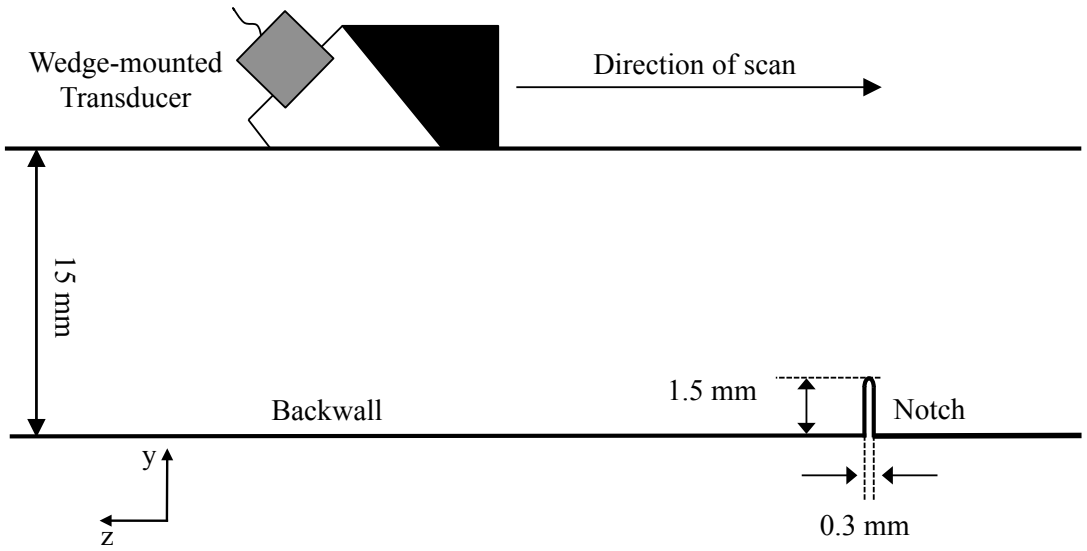


Figure 4.7: Schematic diagram of the setup used to collect experimental data. The out-of-plane extent of the defect is 3 mm

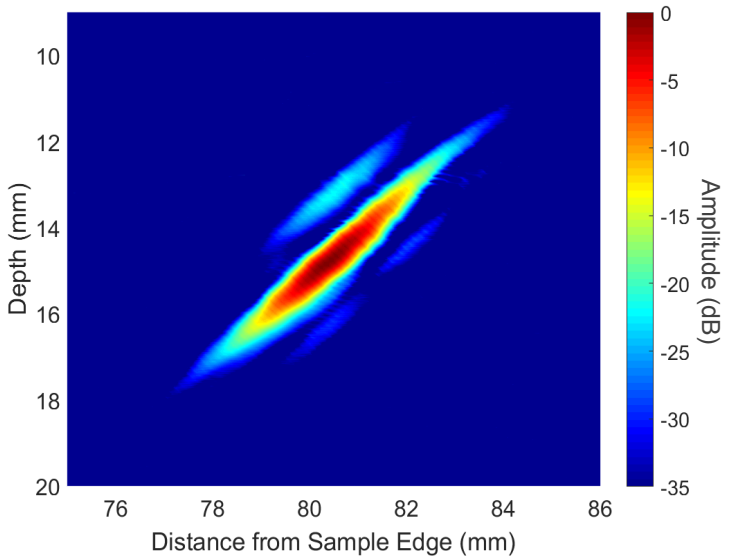


Figure 4.8: B-scan image formed from the experimental data.

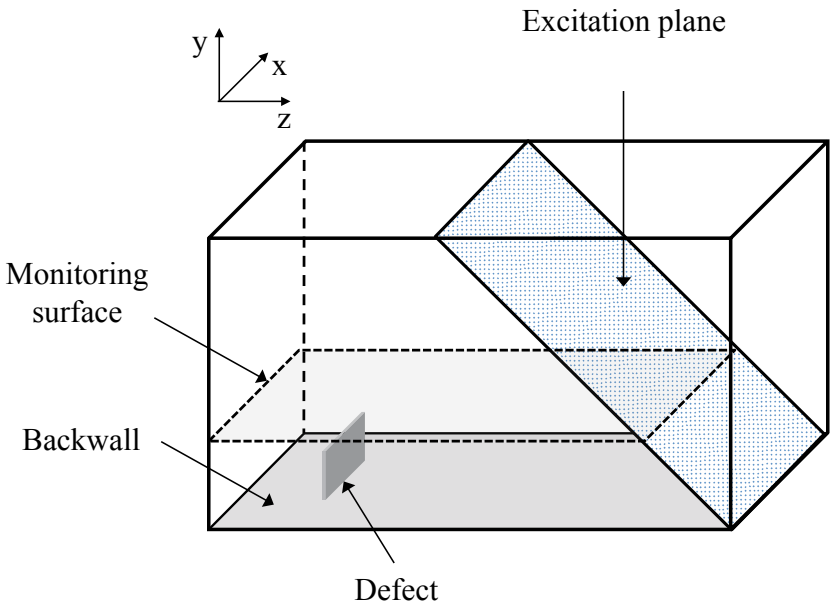


Figure 4.9: Schematic of the defect domain FE model used to simulate the shear wave reflection from the surface-breaking defect. Note the change in z-axis direction in comparison to figures 4.7 and 4.10

the direction of propagation for a shear wave. Therefore, for this validation, it is angled at 45° to ensure the source field is accurately generated. The backwall extent required to capture the corner echo scattering is calculated using equation 4.1; the beam divergence angle is measured at the 20 dB beam edge; this definition of the beam edge is used when sizing defects, particularly those with complex morphology

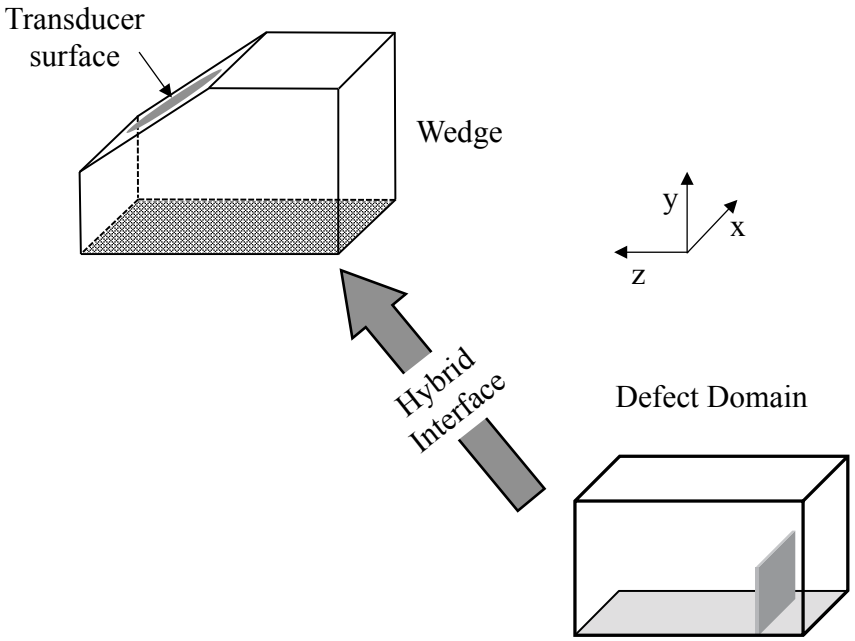


Figure 4.10: Schematic diagram of the hybrid method to link the defect domain FE model with the wedge model.

and multiple facets [114] and is therefore directly relevant to this type of modelling. The 20 dB free-field divergence angle is calculated to be 24° using the beam model and subsequently the minimum required backwall extent in the z-direction is 4 mm. An SRM absorbing region with a thickness of λ_L also surrounds the FE model.

The resulting outer dimensions of the model are 7.4 × 6.6 × 9.9 mm and it is meshed with tetrahedral elements that have an element size of 35 µm ($\approx \lambda_S/18$) using the mixed meshing procedure. The x-z extent of the hybrid monitoring surface is 4.4 × 6.0 mm and it is located at a height of 2.2 mm above the backwall. Stainless steel material properties were also used for the model. The defect shape, including the radius of curvature of the edge, was confirmed by scanning a putty replication of the notch using an Alicona optical microscope (Alicona Imaging GmbH, Austria). The replication putty manufacturer (Microset Products Ltd, Leicestershire, UK) states that the replication will be accurate to ±0.1 mm

The hybrid interface is used to propagate the scattered wave field to the bottom surface of the wedge. The schematic diagram in figure 4.10 illustrates the general procedure; the bottom surface of the wedge is shaded in the figure. The x-z extent of the wedge surface is 12 × 13 mm and it is located at a height of 15 mm above the backwall.

Finally, to propagate the wave through the wedge material, the beam model is again employed. In the experiment, water was used to couple the wedge and the test piece; the boundary condition at the interface requires the continuity of normal displacement and stress and for all other components to vanish. Accordingly, the normal component of displacement is extracted from the scattered wave field predicted by the hybrid model and used for the propagation through the wedge. The wedge material is Perspex, which has a longitudinal wave speed of $2680\,\mathrm{m\,s^{-1}}$ and density of $1180\,\mathrm{kg\,m^{-3}}$. Once the scattered displacement field has been predicted at the transducer surface, an average over all points is taken.

To simulate the line scan performed in the experiment, the process is repeated 80 times and the location of the wedge and transducer is moved over the location of the defect at 0.2 mm increments. The resulting B-scan image is plotted in figure 4.11(a).

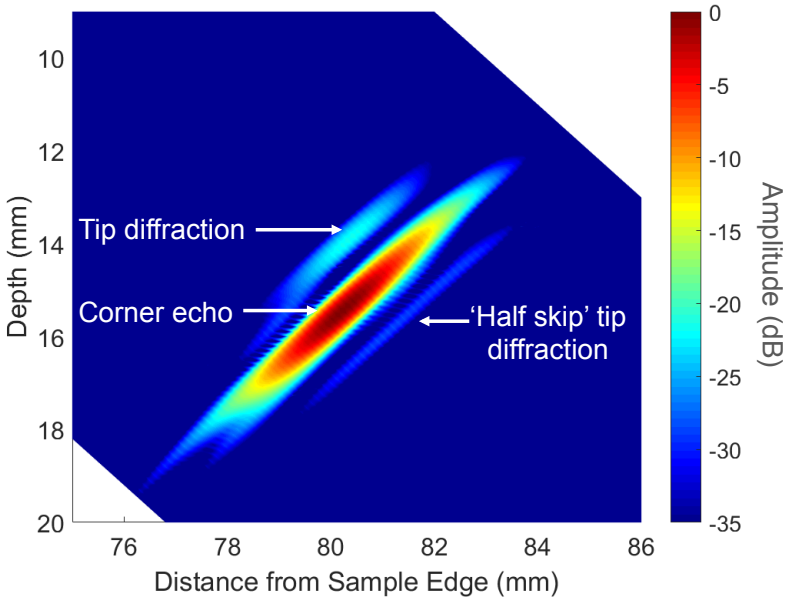
4.4.3 Discussion

The B-scan image from the simulated data shows good agreement with the image from the experimental data. In each image, there are three key features which result from well-known scattering phenomena. These have been labelled on figure 4.11(a) and are often used in practice to characterise surface-breaking defects. Here, these features are compared as a measure of agreement between the images.

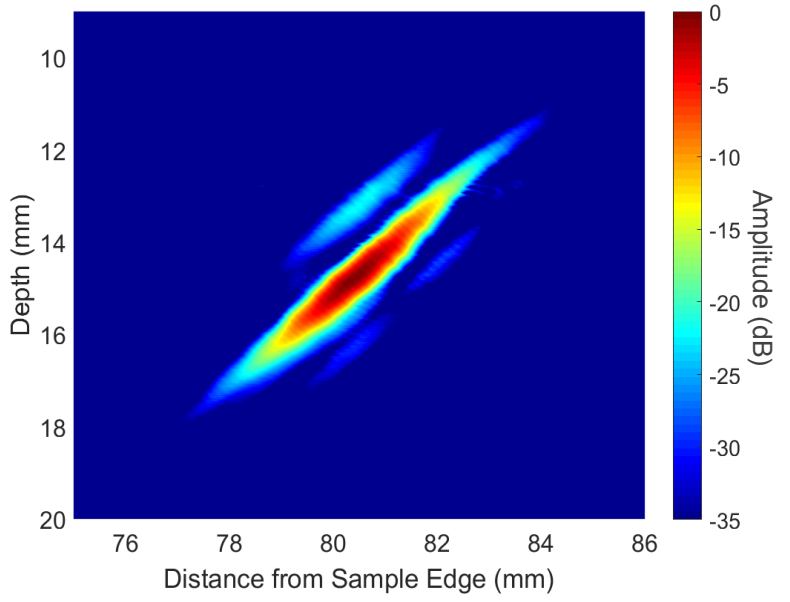
Firstly, the high amplitude indication which lies symmetrically about the centre of each image is due to the corner echo scattering (figure 4.1). Because it has the largest amplitude, all data in each image are normalised to the maximum of this feature. The corner echo is typically used to estimate the location of a defect. For example, the maximum of the feature in the experimental data corresponds to a distance from the sample edge and depth of 80.5 mm and 14.8 mm respectively; for the simulated data, the predictions are 80.2 mm and 15.4 mm, respectively. The defect is located at 80 mm from the sample edge and a depth of 15 mm. The predicted values are in good agreement with the true values. There is a small error in both estimations, however perfect agreement is not expected; the exact location of the maximum may not directly coincide with the defect location due to the divergence of the incident beam. The experimental data set is also effected by a tolerance of ± 0.2 mm given on the location of the defect in the test sample and the distance from

transducer to the datum point measured by a ruler with precision of ±0.2 mm.

Secondly, the feature which lies above and parallel to the corner echo is due to the diffraction of the incident wave from the tip of the defect. The peak amplitude



(a)



(b)

Figure 4.11: The B-scan image generated by the hybrid simulation is shown in (a). The scattering mechanisms of the distinct features on the image have been labelled. The experimental B-scan image has been repeated in (b) for comparison to (a)

of this feature in the experimental data is −21.5 dB relative to the corner trap, whilst in the simulated data it is −21.4 dB; the simulation is therefore in excellent agreement with experiment. This signal is commonly used to determine the through wall height of the defect. In the experimental data, the estimated through wall height is 1.8 mm, and the simulated data estimates it as 1.5 mm. The prediction from the simulation is in excellent agreement with the defect specification, which has a through wall height of 1.5 mm. The prediction from experiment has a small error; however the tolerance of the EDM process was quoted as ≈ 0.2 mm, which accounts for a significant proportion of the error. Further uncertainty is introduced by assuming stainless steel material properties to calculate the wave speed of the material; the actual wave speed of the test piece may vary from this value.

Finally, the feature on the image that lies below the corner echo indication is labelled as the half skip tip diffraction and this scattering process is illustrated by figure 4.12. The 'half-skip' refers to the reflection off the backwall, where 'full-skip' is commonly used to refer to a wave that is reflected from two component surfaces before detection. The peak amplitude of this feature in the experimental and simulated images is −28.0 dB and −28.1 dB, respectively. Again, the simulation agrees well with experiment. It can be seen in figure 4.11(b) that the half-skip tip diffraction feature appears as two distinct indications in the image from experimental data, whereas in the simulated data, it is a single indication. The break in this feature occurs when the corner echo indication amplitude is at its peak, therefore the tip of the defect is not directly insonified by the 45° incident shear wave. At this point, the half skip tip diffraction is reliant on the divergence of the incident

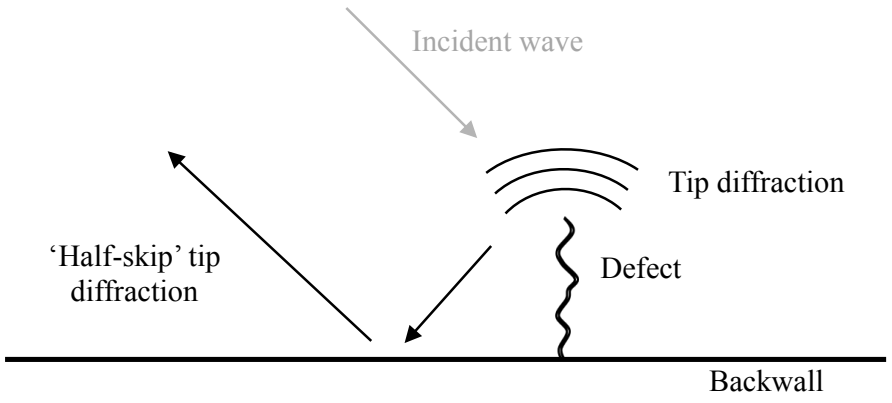


Figure 4.12: An illustration of the tip diffraction and 'half-skip' tip diffraction, where the diffracted waves reflect from the backwall and are measured by the transducer.

Table 4.1: Average computation times for each section of the simulation.

Simulation Component	Time (mins)
Incident wave	13
Defect domain (FE)	4.4
Hybrid interface	28
Wedge model	0.7
Total	46

wave, suggesting that the simulation overestimates the divergence of the incident wave. This is confirmed by noting that the features in the simulated B-scan appear elongated in comparison to that of the experimental B-scan.

The average computation times for each section of the simulation are given in table 4.1. The most time-consuming sections of the simulation are the hybrid interface and the incident wave model. However, it is important to note that both sections are written in the interpretive scripting language MATLAB and were run on a single core of the computer; the computation time will significantly decrease by transferring these sections into compiled code and taking advantage of parallel processing.

4.5 Attenuation due to Roughness

To demonstrate an application of the hybrid model, this section reports an industrially relevant case study into the effect of surface roughness on the scattering from a surface-breaking defect. The attenuation of the reflected ultrasound due to defect roughness has been the subject of many previous investigations [9, 11, 53, 54]; it is often the case that studies that employ numerical simulations are often performed in 2D as they are limited by the sheer computational resource required in 3D. However, 2D simulations do not capture the effect of roughness in the out-of-plane dimensions and can therefore only give general indications of the trends. Full 3D simulation is needed to go beyond this to be able to provide accurate quantitative analysis. Furthermore, there has been no previous investigation for the case of surface-breaking defects, which are of key interest to this work.

The Gaussian statistical model employed in section 4.3 is used here to describe defect roughness and requires both the correlation length, λ_0, and the RMS height, σ, to be defined. Previous research has highlighted that the ultrasonic scattering

from a rough surface is independent of the lateral variation in surface height if the correlation length is smaller than the extent of the defect surface [11]. The correlation length is therefore held constant at a value of 300 µm. The RMS height is used to classify defect roughness and is varied from 75 to 525 µm in 75 µm increments, to study the ultrasonic attenuation over increasing roughness. For each classification of roughness, the attenuation is quantified in a Monte Carlo approach, where the peak amplitude of the scattered field is measured from 50 rough surface-breaking defects and the average of these values is taken.

The model setup is illustrated in figure 4.14. A plane shear wave is incident at 45° on a 3 × 3 mm square surface-breaking defect within the FE model of the defect domain. A Hann-windowed 5 cycle tone burst with a 2 MHz centre frequency is used to excite the wave. The outer dimensions of the FE model are 12.6 × 8.3 × 19 mm, which include absorbing layers that have a thickness of λ_L, and the element size is 75 µm. The hybrid monitoring surface has an x-z extent of 6 × 12 mm, as in section 4.3, and is positioned at a height of 4.5 mm above the backwall. Stainless steel material properties are again assumed. The scattered wave is predicted by the hybrid interface at 50 mm in the y and negative z-direction from the defect.

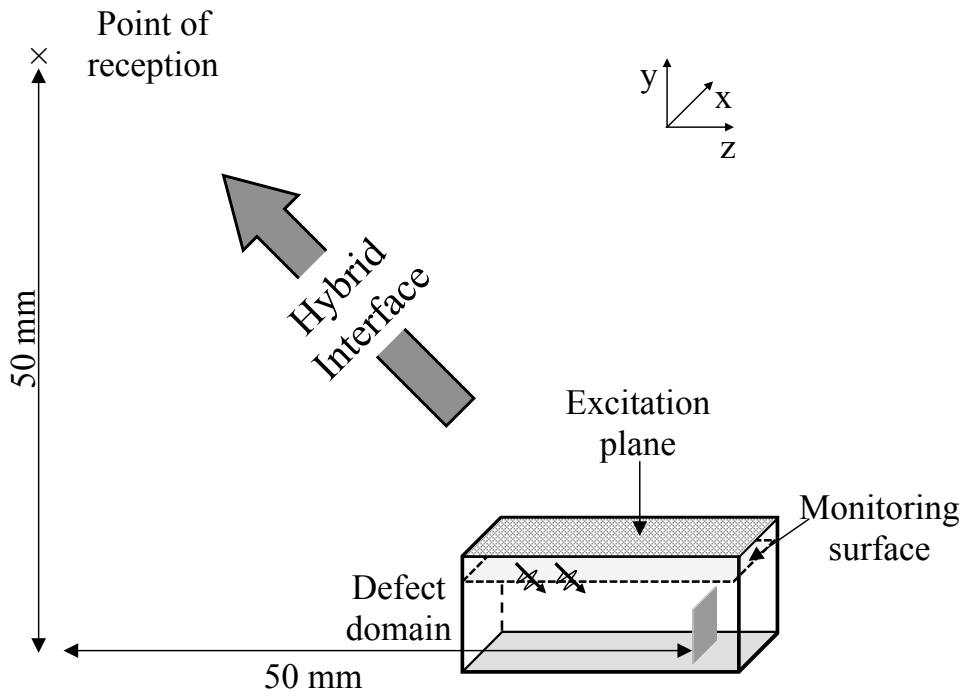


Figure 4.13: Schematic of the hybrid method to simulate the ultrasonic scattering from a surface-breaking defect with a rough surface.

4.5.1 Results and Discussion

The average attenuation is calculated relative to the scattering from a smooth surface-breaking defect and plotted over increasing defect roughness in figure 4.14. To provide context for these results, the coherent field attenuation calculated by an extension to the Kirchhoff Approximation (KA) [53] is also plotted in figure 4.14. It should be noted that there are distinct differences between these calculations, yet the comparison is made because the KA prediction is used widely across the UK nuclear sector to account for roughness on defects. KA is generally valid for planar defects that have a low level of roughness where the diffraction signal makes a negligable contribution to the ultrasonic response. The attenuation predicted by both models up to approximately 250 µm is in agreement with the mean. Beyond this point, the attenuation predicted by the hybrid model begins to plateau, tending towards −15 dB, confirming the overestimation of ultrasonic attenuation at high roughness by KA also observed in previous findings [11].

Confidence bands have also been plotted in figure 4.14 to give an indication of the spread of attenuation values. The confidence bands were calculated using an empirical cumulative distribution function and show the 95% spread about the mean. In general, the confidence bands follow the same trend as the mean and confirm the pessimism of KA at high roughness. However, at low roughness, the

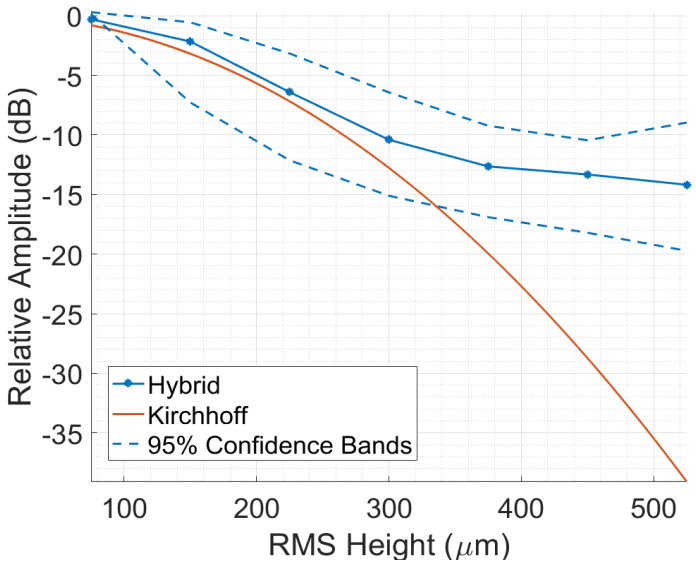


Figure 4.14: Attenuation of scattered wave from a surface-breaking defect with increasing roughness calculated with the hybrid model (blue) and the Kirchhoff approximation (red).

confidence bands extend below the analytical prediction suggesting that KA underestimates also the ultrasonic attenuation at low levels of roughness for the inspection parameters chosen here.

The defect domain FE model was run using two Nvidia (Nvidia Corporation, California, US) GeForce GTX Titan graphics cards that each have a total memory of 6082 MB. To simulate a single model with a full numerical approach would require an FE model to extend to the point of reception, which would require around 94 million nodes. This in turn would require approximately 79 GB of memory, assuming that memory usage scales linearly with model size, and would require a significantly larger amount of pre-processing time. Without the hybrid method, it would therefore become impractical to carry out Monte Carlo study, such as the one performed here.

4.6 Conclusions

A 3D hybrid method, which links numerical and semi-analytical methods, has been demonstrated to accurately simulate ultrasonic NDE inspection of components containing surface-breaking defects in three dimensions. The method substantially increases the computational efficiency over a full numerical model, yet retains the ability to simulate the scattering from complex defects. From the ultrasonic inspection techniques discussed in subsection 2.2.1, a methodology for simulating the angled shear wave inspection technique was presented because this captures a range of scattering mechanisms which occur in other typical ultrasonic inspection techniques. It was discussed that the scattering from the defect and the connecting component surface must be fully captured in the defect domain, which is simulated here using an FE model. Numerical verification was carried out by comparing the predicted displacement from the hybrid method to a full FE simulation and good agreement was found. For experimental validation, a complete ultrasonic inspection system model was presented by utilising the work presented in chapter 3 to accurately simulate the incident ultrasound field. The validation consisted of a line scan over a surface-breaking EDM notch and the resulting B-scan image was compared to experiment; good agreement was found in both the position and amplitude of the features in the image.

Finally, the hybrid method was used to study the attenuation of reflected ultrasound from surface-breaking defects for increasing surface roughness. The mean

results agreed with the widely used KA at low levels of roughness, however at high roughness KA was seen to overestimate the ultrasonic attenuation. Furthermore, the confidence bands calculated from the data set also suggest that KA under-estimates the attenuation at low roughness values for a significant fraction of the defect population. It was shown that the hybrid method provided a significant reduction in the memory requirements over a full numerical simulation, making it practical to simulate the ultrasonic inspection of thick section components containing complex shaped defects without being limited by the computational resource requirements. Having established the hybrid method and confirmed its performance against a full numerical model for a smooth and rough defect and against experiment for a smooth defect, it can now be put into action to simulate the inspection of a real thermal fatigue defect, which are often encountered in NSRP components.

Chapter 5

Simulating the Ultrasonic Response from a Thermal Fatigue Defect

5.1 Introduction

Numerical modelling techniques are powerful tools for simulating the scattering of elastic waves from complex shapes, such as crack-like defects. The focus of this thesis is the development of an ultrasonic inspection model which can be used to inform the inspection of safety-critical components, therefore a high level of confidence in the modelling technique is required. This ultimately leads to the requirement of substantial experimental validation before the modelling can be relied on. With the rapid growth of computing power, the advent of specialist GPU solver capability and hybrid modelling techniques, it is becoming possible to push the capability of numerical simulation methods and provide a level of experimental validation that has not been previously attainable.

Contained within the literature are studies showing validation of FE-based models against experimental results for the simulation of ultrasonic scattering from geometrically simple scatterers [74, 95, 115, 116]. Yet there is limited experimental validation for simulating the ultrasonic scattering from complex morphologies, such as rough crack-like defects. Pettit *et al.* [117] directly compare the ultrasonic amplitude response from a test piece containing a smooth sinusoidal defect machined into the backwall with a 2D FE simulation. The results show good agreement in

both time of arrival and amplitude relative to a flat backwall. Furthermore, the validation in [117] also compares the variation in ultrasonic response from a real rough surface measured experimentally to 2D FE simulations using simulated Gaussian rough surfaces; the general trends in attenuation due to roughness predicted by the FE model agree well with experiment. Choi *et al.* [118] used an efficient 3D FE unit cell model, which employs cyclic symmetrical boundary conditions to simulate an infinite periodic surface [119], to simulate a normal incidence compression wave ultrasonic inspection of a ductile fracture surface and concluded the FE approach was valid by comparison to the experimental results. Dobson *et al.* [120] showed excellent agreement between 3D FE and experimental results for predicting the attenuation of torsional guided wave modes as they pass through a rough corrosion patch machined into a pipe.

This type of validation evidence is crucial for using simulation data to inform the design and qualification of inspections on safety critical components. X-Ray Computed Tomography (XCT) can provide non-destructive measurements of defect surface morphology to a high resolution; using XCT lowers the risk of modifying the defect shape that may be caused in destructive analysis, such as for stylus measurements or optical surface profiling. Through image segmentation, it is possible to convert the XCT data into a 3D digital geometry, such as a Computer Aided Design (CAD) model, which can be used to generate a mesh for the FE simulation. Previously documented uses of XCT data to implement real defect morphology into a simulation has been in the context of stress corrosion cracking, where a slice of the CT data was used in an efficient 2D hybrid model to simulate an array inspection [94]. However, there has been no previous study simulating the ultrasonic response from a full 3D defect morphology measured using XCT.

The work in this chapter presents a methodology for using the hybrid model developed in chapters 3 and 4 to simulate the complex ultrasonic interaction with real defect geometry. The outcome of this work provides a level of validation for using hybrid model simulations to inform the design and justification of inspections carried out on safety-critical components, as well as a methodology to enable further work of this kind to be completed. Section 5.2 discusses the experimental ultrasonic data collection on the defect and section 5.3 discusses the process by which a mesh of the defect was created from an XCT measurement of the defect morphology. The simulation using the defect mesh is presented in section 5.4 and the experimental and

simulated results are compared in section 5.5. Section 5.6 discusses the significance of using a faithful representation of the defect morphology by comparing the tip diffracted response to a typical reference target. Finally, section 5.7 provides a summary of the work in this chapter.

5.2 Experimental Data Collection

Thermal fatigue is a common cracking mechanism on nuclear plant components [121, 122] and occurs as a result of the constrained thermal expansion when a component is subject to repeated heating and cooling, for example, at the mixing of low and high temperature fluids [123]. The morphology of these cracks is known to be complex; the crack surfaces are often rough and commonly initiate at the surface of a component [3]. Although this work will focus on thermal fatigue defects, the general methodology is applicable to any type of defect.

An austenitic stainless steel test piece containing a single thermal fatigue defect was produced by Trueflaw [4]. The samples are subject to repeated heating and cooling through electromagnetic induction and water or air cooling [5] in order to induce thermal fatigue. The through wall height of the induced defect is dependent on the magnitude of the thermal cycles and total number of cycles therefore these parameters were set by the manufacturer, based on destructive and non-destructive analysis of previous samples, to generate a crack with a through wall height of approximately 5 mm. The surface length of the defect is approximately 15.5 mm. The profile of the defect at the surface of the test piece is shown in the stitched optical microscope image in figure 5.1.

A 32-element broadband ultrasonic linear array transducer (IMASONIC 5725A102)



Figure 5.1: Stitched optical microscope images of the defect profile on the surface. No scale is provided on the images however the surface length of the defect is approximately 15.5 mm.

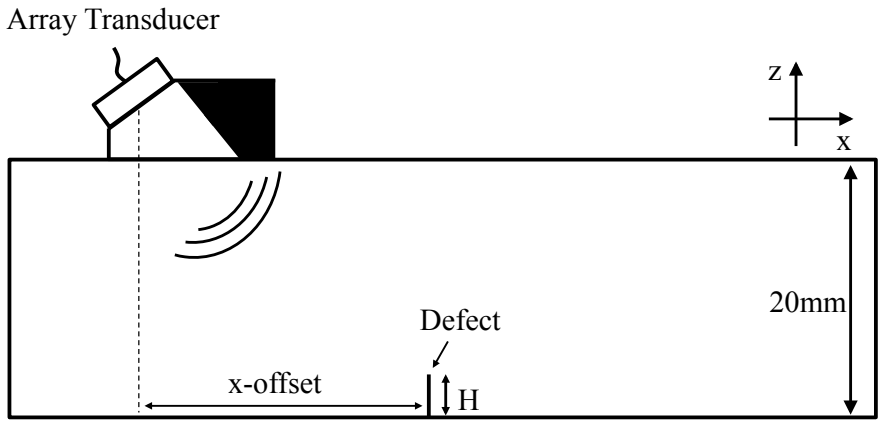


Figure 5.2: A schematic of the inspection setup. The test piece thickness is also given.

with a 4 MHz centre frequency was used to collect the ultrasonic data. The array elements have a length of 10 mm, a pitch of 1 mm and inter-element spacing of 0.15 mm; the array is mounted to a Perspex wedge at angle of 34.7° to the normal. This enables shear waves to be generated within the stainless steel samples. The shear wave speed of the test piece was measured as $2923\,\mathrm{m\,s^{-1}}$.

FMC data were collected using a PeakNDT FMC micropulse system at a sampling frequency of 100 MHz. The array location is illustrated in figure 5.2. The horizontal (x-direction) position of the array was offset from the location of the defect in order to maximise the ultrasonic response for a 45° incident angle. FMC data is acquired at 1 mm increments as the array is scanned along the length of the defect, as shown in figure 5.3. An image of the experimental setup is given in figure 5.4; the array is coupled to the test piece using water and a two-axis manipulator is used to scan the array along the length of the defect. Omitted from the image are a series of other stainless steel plates which are positioned around the test piece under inspection that are used to stop the test piece from moving as the array is scanned.

By collecting FMC data, different methods of post-processing can be used to image the data. A common inspection modality for the detection of surface-breaking defects is the B-scan. As detailed in section 4.4, a typical B-scan consists of recording P-E data as a monolithic transducer is scanned in a single direction. For example, a transducer may be scanned in the x-direction shown in figure 5.2 over the defect location. Using an array, a number of contiguous array elements, referred to as the aperture, can be fired in-phase to generate a plane beam, similar to that generated by monolithic transducer. The aperture can be moved electronically by sequentially

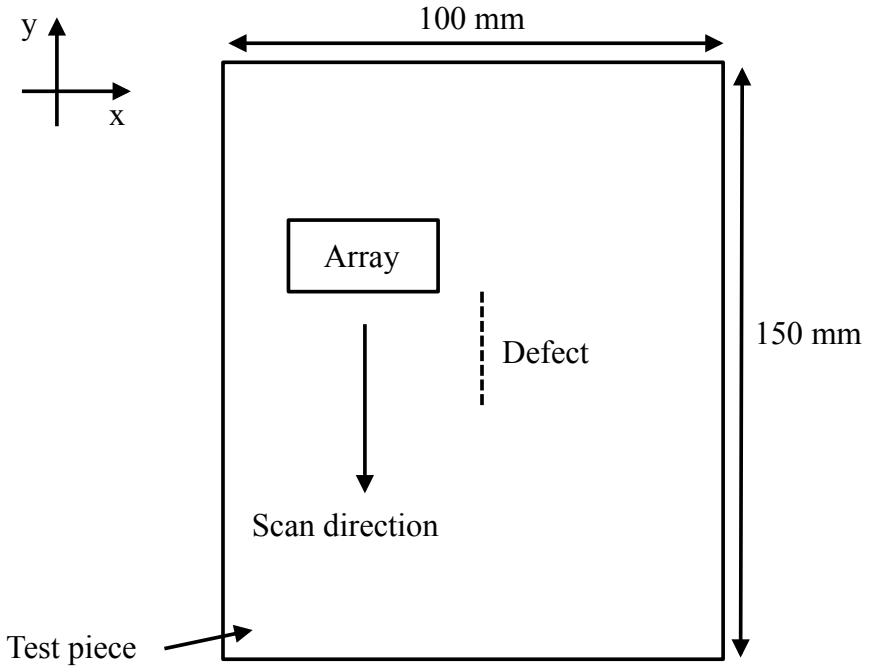


Figure 5.3: A schematic of the ultrasonic array scan path along the length of the defect. The test piece dimensions are also given.

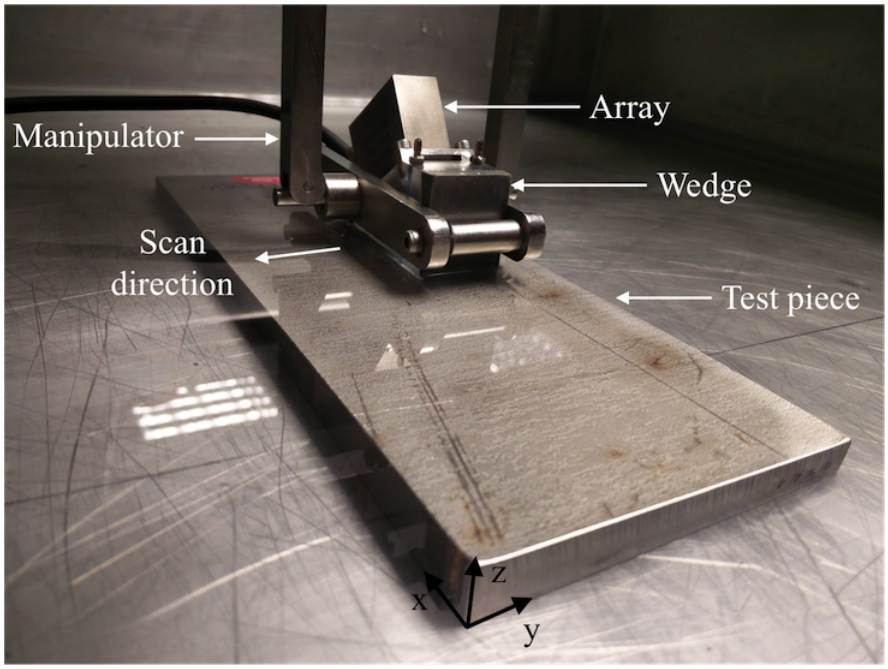


Figure 5.4: Photograph of the experimental setup used to capture the ultrasonic data. The array is coupled with water to the test piece and a manipulator is used to scan the array across the length of the defect.

shifting the set of elements across the array to recreate the scan (figure 5.5), whilst recording P-E data. This is often referred to as an electronic scan (e-scan). In post-

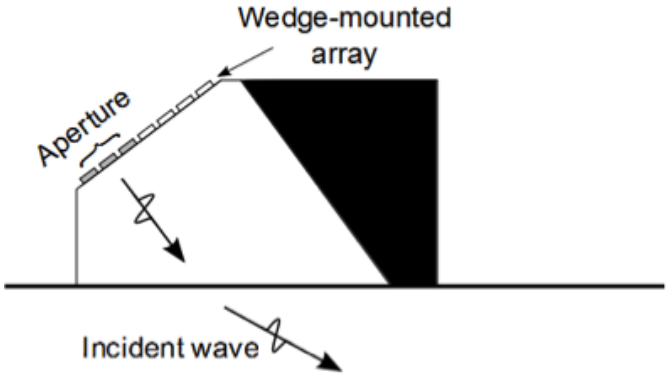


Figure 5.5: Illustration of a B-scan inspection using an array transducer; the aperture is moved electronically across the array elements to perform the scan.

processing, an appropriate subset of the FMC data combined with the appropriate time delays can be used to recreate the same e-scan [44].

5.3 XCT Imaging and Mesh Generation

This section discusses the XCT data collection and the process required to convert output from XCT into a mesh for the hybrid simulation. The XCT data collection was performed in collaboration with Nikon Metrology (Nikon Metrology UK Ltd, Tring, UK) and the image segmentation and mesh generation were performed in collaboration with the Manchester X-ray Imaging Facility (School of Materials, University of Manchester, Manchester, UK).

5.3.1 XCT Imaging

The underlying principles of XCT can be found in reference texts or articles in the literature, for example [124, 125]. A schematic of the setup used to collect the data is shown in figure 5.6; the XCT measurements were performed using the XT H 320 system (Nikon Metrology UK Ltd, Tring, UK). The system contained a 225 kV rotating target X-ray source with a minimum focal spot size of 10 µm and a Perkin Elmer 1611 flat panel detector containing 4096 × 4096 pixels of 16-bit amorphous silicon sensors. The source-to-sample and source-to-detector distances are shown on figure 5.6. As depicted by the figure, a helical scan was performed whereby the sample is rotated and translated through the cone of X-rays produced by the source. Once the rays have passed through the sample they are received by the

detector panel. The scanning parameters are given in table 5.1; the copper-tin filter is used to reduce beam-hardening effects.

To achieve the greatest image resolution, a high magnification was used; however, high magnification can often lead to image blurring. Using the rotating target source, which dissipates heat more efficiently than a static target, it was possible to ensure the focal spot size was small enough to provide a sharp image. To achieve the desired magnification, it was necessary to prepare the test pieces such that the area of interest within the sample could be positioned at the required distance from the source. Therefore, the test pieces were sectioned to remove excess material surrounding the defect.

Consideration was given to the method of material subtraction as it is important for the defect surfaces to remain unaffected by this process. The sectioning was performed using wire-cut Electrical Discharge Machining (EDM) [126]. EDM does not make physical contact with the test piece and therefore does not directly apply a force, minimising the possibility of affecting the defect morphology. A photograph

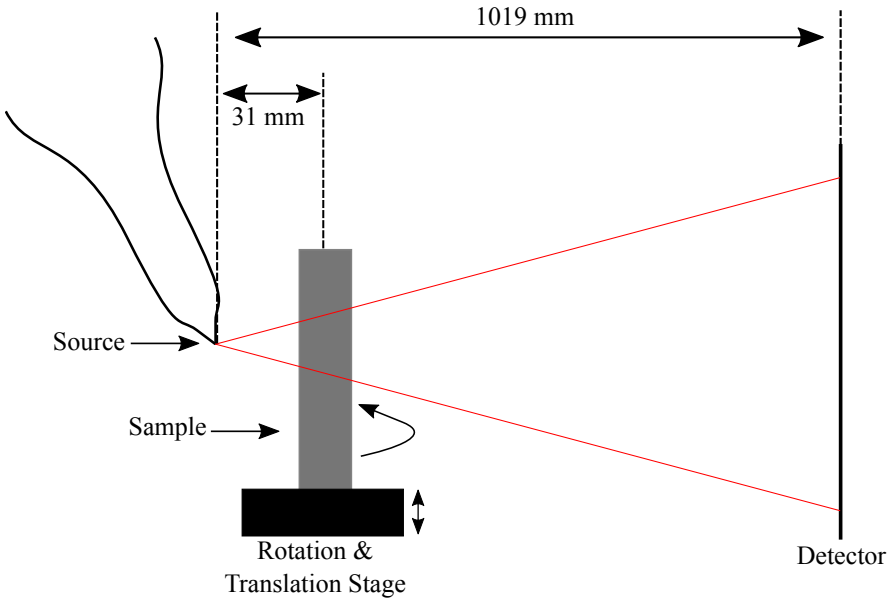


Figure 5.6: Schematic of the XCT setup.

Table 5.1: XCT scan parameters.

Voxel size (µm)	Voltage (kV)	Current (µA)	Acquisition time (mins)	Filters	Number of projections
6.08	200	500	142	1.6 mm Cu + 1mm Sn	6015

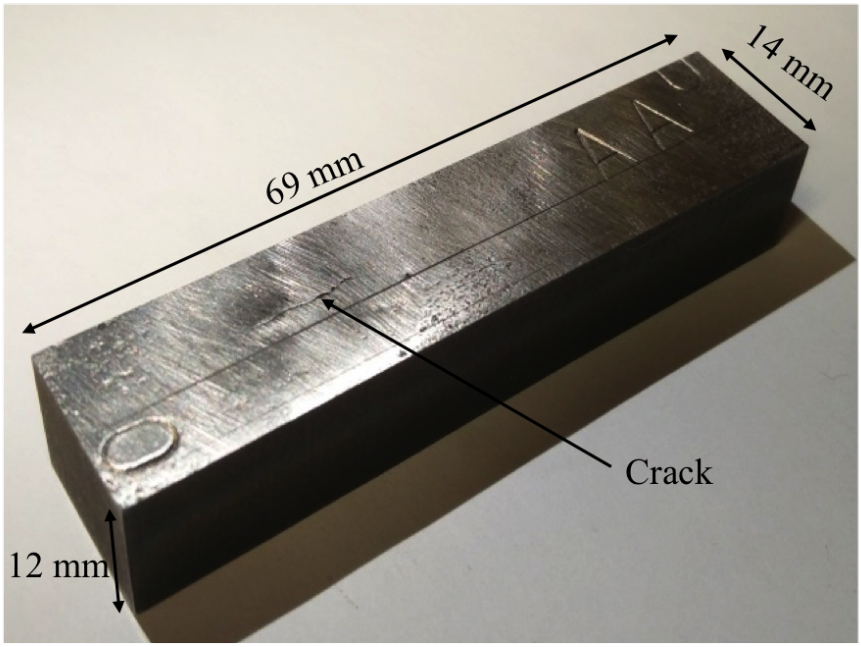


Figure 5.7: Photograph of the CT coupon made from sectioning the test piece.

of the sectioned test piece, herein referred to as the CT coupon, is shown in figure 5.7 and the coupon dimensions are given on the figure. The distances from the EDM cut edges to the edges of the original test piece were measured in order to position the XCT data correctly in the simulation.

A voxel width of 6.08 µm was achieved in the reconstruction of the test pieces. The output from the CT scan was a stack of Tagged Image File Format (TIFF) greyscale images, where each image in the stack represents a 2D slice of the 3D volume. The pixel size in the images is equal to the voxel size and the pixel grey intensity is dependent on the attenuation of the X-rays as they pass through the sample. An example of a TIFF image is shown in figure 5.8, where the stainless steel sample material appears as a lighter grey than the air within the defect due to the increased x-ray attenuation within the sample.

5.3.2 Image Segmentation

The images were imported into Avizo (Thermo Fisher Scientific, Massachusetts, USA) to carry out image segmentation. Image segmentation is the process by which a digital image, or group of images, is partitioned to identify distinct materials within it and provides each pixel with a label. This process is required to identify the boundary of the defect in order to generate the FE mesh. Initially, a bilateral

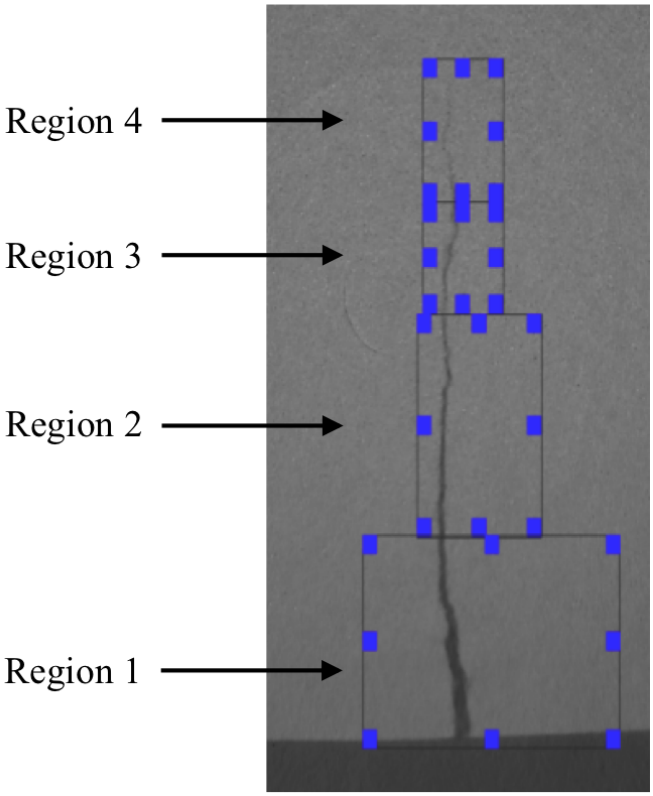
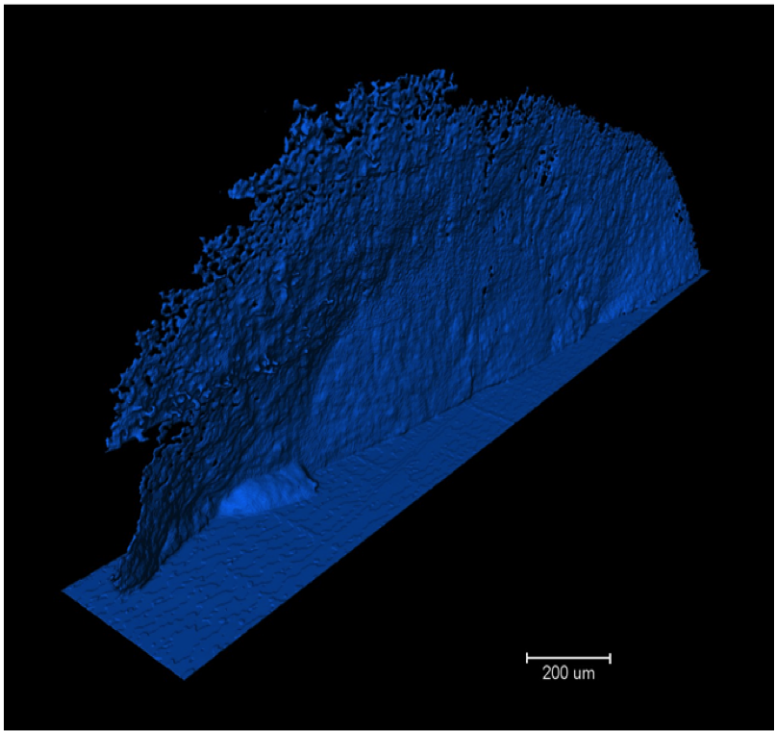


Figure 5.8: An example of the filters applied to the image reconstructed by the CT process. The segmentation was performed by dividing the image into smaller regions.

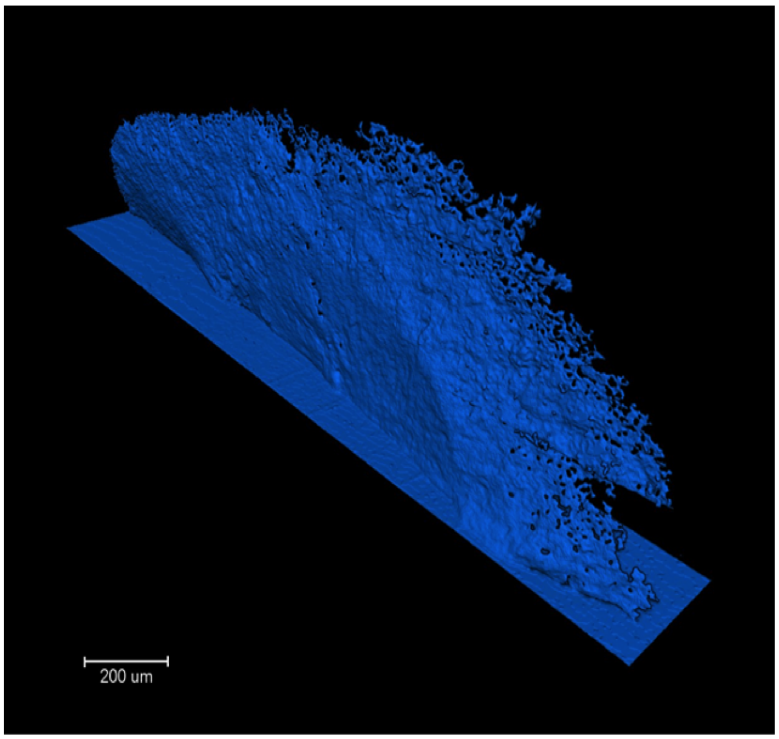
filter was applied to all images to improve the segmentation procedure. The bilateral filter smooths the image whilst preserving edges by calculating a weighted average for each pixel over its neighbouring pixels [127].

As can be seen from figure 5.8, there is significant variation in the contrast of the crack boundary relative to the parent material as the crack penetrates further into the sample. As an X-ray travels through the sample, it will undergo two levels of attenuation, one from the block and the other from the air within the crack, leading to the distinct grey levels seen in the image. In the areas where the crack opening becomes negligible, the resolution of the image blurs the grey levels together reducing the contrast. Due to this contrast variation of the boundary, it was found that applying a single segmentation method to the entire TIFF stack did not achieve an acceptable result. Therefore, the images were divided into multiple smaller regions that had less variation in contrast and more optimal segmentation methods were applied in each region. An example of the division is shown in figure 5.8.

For the regions on the crack that have the largest opening, labelled as region 1 on figure 5.8, the segmentation was performed by thresholding; thresholding is



(a)



(b)

Figure 5.9: Images of the reconstructed defect morphology after segmentation from two different viewing angles.

where a binary image is generated from the greyscale image by comparing each pixel against a single cut-off intensity and labeling it accordingly. For the regions which could not be thresholded effectively but where the crack boundary remained moderately visible, labelled as region 2 on figure 5.8, a top-hat transform was first applied, followed by the thresholding. A top-hat transform [128] can be used to enhance the features that have a low intensity relative to local pixels and therefore enhance the contrast ratio between the sample and the defect.

For region 3, the watershed transform [128, 129] was used to carry out the segmentation. The watershed transform treats the image as a topographic map and determines the peaks and troughs in the image based on pixel intensity. This technique is effective for distinguishing between features of interest that are separated by a small distance, lending itself well to identifying the crack boundary when the opening is small. In region 4 where the crack is least visible due to the tip closure, the segmentation was performed manually slice by slice; although this method is extremely user intensive, there was no automated process that could provide satisfactory results in this region. The resulting segmented defect is shown in figure 5.9.

It is clear from figure 5.9 that the defect follows a semi-elliptical shape, which has been observed by other authors [5] and is a commonly assumed shape for thermal fatigue defects. The general shape of the defect is well defined; however, the tip morphology is seen to become porous and discontinuous. It is difficult to evaluate the accuracy of this representation due to the low contrast ratio of the reconstructed images from the CT data at the crack tip, as observed in figure 5.8. The manual segmentation of this region eliminates the errors of automated segmentation methods but leads to the introduction of human error. Nevertheless, as the crack surfaces come into contact at the tip of the crack, the stress-free boundary condition for wave scattering breaks down and a portion of the wave field will be transmitted across the boundary [130]. The model used here requires the defect to be defined by a distinct stress-free boundary, therefore the porosity provides an approximation to the break down of the stress-free boundary condition.

5.3.3 Mesh Generation

One approach for generating a volume mesh from image data would be to convert the image into a Computer-Aided Design (CAD) file format. Most commercially available meshing programs support the import of CAD files as it is a common industrial requirement. The mesh would then be generated directly from, or after manipulation of, the imported CAD file. However, the conversion to a CAD file can be prone to errors for complex geometries and often requires manual editing, subsequently leading to a loss of accuracy [131]. Nevertheless, this approach is attractive because CAD files are transferable between many engineering computer programs that can be used to visualize and manipulate the defect, which may assist in the interpretation of the ultrasonic data. As a result, this approach was pursued. A stereolithography (STL) file was initially generated from the segmented image of the XCT data. However due to the complexity of the defect geometry, importing the STL file into a selection of meshing programs was unsuccessful. The root cause of the issue proved difficult to decipher, but many CAD programs suggested there were self-intersecting triangular facets and holes in the surface-mesh. As neither the automatic mesh-repair schemes provided by CAD programs nor manual editing of the CAD file provided any improvement, this approach was abandoned.

An alternative approach is to directly convert the image data into a mesh by a process referred to as image-based meshing. A simple yet effective image-based meshing approach is the voxel method [132]. In this method, the discretisation provided by the voxels in the XCT data is directly used to form hexahedral elements. The resulting mesh contains high quality elements throughout and the implementation of this approach is trivial. However, the surface discretisation provided by this type of mesh will be poor because the mesh boundary will be stepped. This approach is not optimal for the simulation of ultrasonic scattering unless the surface discretisation is very fine (i.e. less than 30 elements per wavelength [10]), which leads to extremely large and often infeasible computational requirements, particularly in 3D.

A related approach, known as Volumetric Marching Cubes (VOMACS) [133], is a volumetric meshing technique that is formulated on a similar principle to the marching cubes surface discretisation method [134]. The VOMACS technique uses structured linear tetrahedral elements to discrestise the bulk of the model domain.

At an interface, such as a crack boundary, a triangular surface mesh is generated [134] and the resulting surface triangles are used to form one face of a tetrahedral element that lies on the boundary. Therefore, elements that lie on a boundary are distorted to conform to the boundary, rather than assuming that the boundary conforms to the voxel discretisation.

This approach is attractive in the context of this project as it is desirable for the mesh to be as uniform as possible in the bulk of the material to accurately simulate bulk wave propagation. Furthermore it has been shown that meshes that provide a level of distortion to conform to a scatterer geometry give a more accurate representation of the ultrasonic scattering at lower nodal densities [10]. The VOMACS approach has been implemented in the Simpleware software package (Simpleware, Exeter, UK) in an 'enhanced' version termed EVOMACS [131] or 'FE Grid'. The enhanced Simpleware approach enables the meshing of images containing multiple components, mixed hexahedral and tetrahedral meshes and mesh density control to enable coarsening. As these enhancements are not required here, the mesh controls are set to represent the VOMACS meshing procedure.

The FE Grid algorithm generates a mesh based on the voxel size, therefore the resulting element edge length would be 6.08 µm. This would result in the defect domain of the hybrid model requiring an infeasible amount of computational resource. The spatial sampling of defect geometry was therefore down-sampled to 40 µm ($\approx \lambda_S/20$), such that the mesh size meets the guidelines for FE modelling

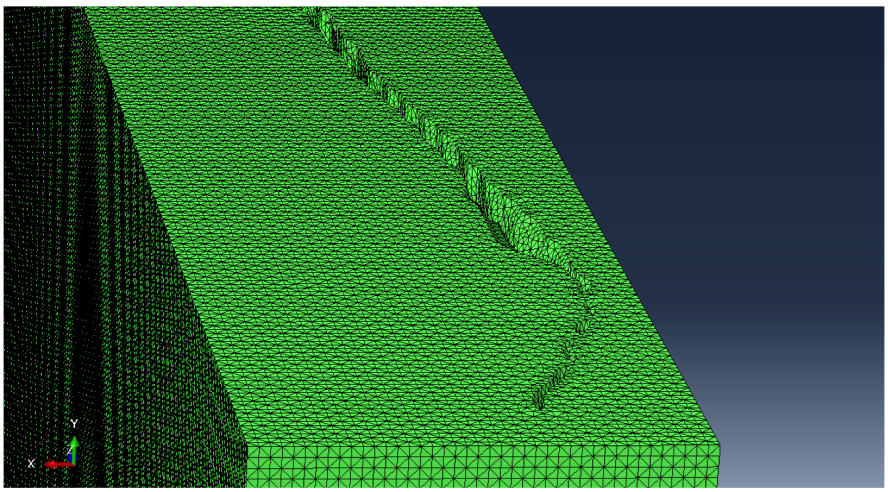


Figure 5.10: A snapshot of the resulting FE mesh of the thermal fatigue defect. Visualised in ABAQUS CAE.

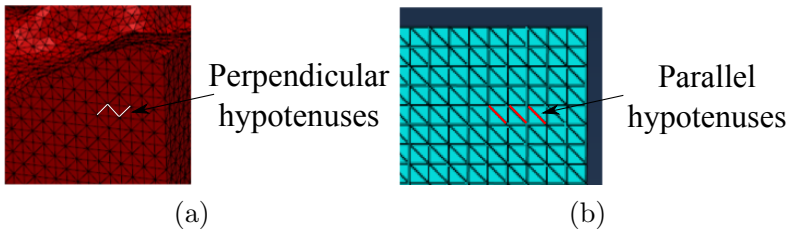


Figure 5.11: Images of the elements that lie on the boundary of the mesh generated by (a) the FE Grid algorithm where the adjacent hypotenuses are perpendicular and (b) the custom mesh appending algorithm where the adjacent hypotenuses are parallel.

(subsection 2.4.4) but can also be executed on the available computational resource. A snapshot of the mesh is given in figure 5.10.

Due to the size of the defect, the mesh was only generated in the local area of the defect. However, the defect domain of the hybrid model also requires a region of the back wall to be present in the FE model, as discussed in sub-section 4.2.1, as well as absorbing layers surrounding the model. Therefore, as used in section 4.3, a structured tetrahedral mesh is appended to the mesh boundary. However it was noted that adjacent hypotenuses of the elements on the boundary of the FE Grid mesh are perpendicular and form a 'criss-cross' pattern, as can be seen from figure 5.11(a). The current implementation of the custom mesh appending algorithm requires the hypotenuses of the boundary tetrahedra to be parallel, as depicted in 5.11(b). This requirement is to ensure that the hypotenuses of the appended tetrahedral mesh do not cross, as this may lead to spurious reflections.

To gauge whether relaxing this requirement is feasible, a model was constructed to test whether a measurable reflection can be detected from the 'crossing' hypotenuses. The model schematic is shown in figure 5.12. A 3-cycle 1 MHz toneburst is applied to 8 neighbouring nodes in a radial direction (see figure 3.8) to generate a longitudinal wave point source at 3 λ from the crossed hypotenuses, depicted by figure 5.12. The signal is monitored over a surface of nodes in the x-y plane with an x-y extent of 2 λ × 2 λ. The entire model is a cube with an edge length of 16 λ; the model is large enough to ensure reflections from the boundary can be separated in time from any reflections of interest and absorbing layers are not used for simplicity. An element size of 300 µm is used and stainless steel material properties are assumed giving a longitudinal velocity, shear velocity and density of 5760 $\mathrm{m\,s^{-1}}$, 3110 $\mathrm{m\,s^{-1}}$ and 7800 $\mathrm{kg\,m^{-3}}$ respectively. The crossed hypotenuses of the tetrahedral

elements do not create a physical boundary in the model however the boundary is visible when the mesh is viewed. Figure 5.13(a) shows an example of a mesh of a single material and figure 5.13(b) shows this same mesh in wire-frame view where the crossed element edges can be seen.

To visualise the results, the displacement-time histories that were recorded along a line of nodes parallel to the y-axis at the centre of the monitoring surface are plotted in figure 5.14. The time histories are presented in the form of an uncorrected B-scan, where time is on the vertical axis and the location of the monitor node in the y-axis is given on the horizontal axis. The displacement amplitudes are normalised to the maximum on the plot and converted to a decibel scale.

The incident wave is clearly visible and is labelled on the figure. Due to the radial spreading of the point source, the amplitude of the incident wave decreases as the distance from the centre of the model increases. The smallest distance from the point source to the model boundary is 5 λ (to the top edge shown in figure 5.12), which corresponds to a round trip path length of 10 λ that would be detected at 10 µs. This reflection is clearly visible and is labelled on figure 5.14. The next wave would be expected to arrive at 16 µs, due to a round trip path length of 16 λ (from the x-axis boundaries), which is also marked on the figure. Due to the symmetry

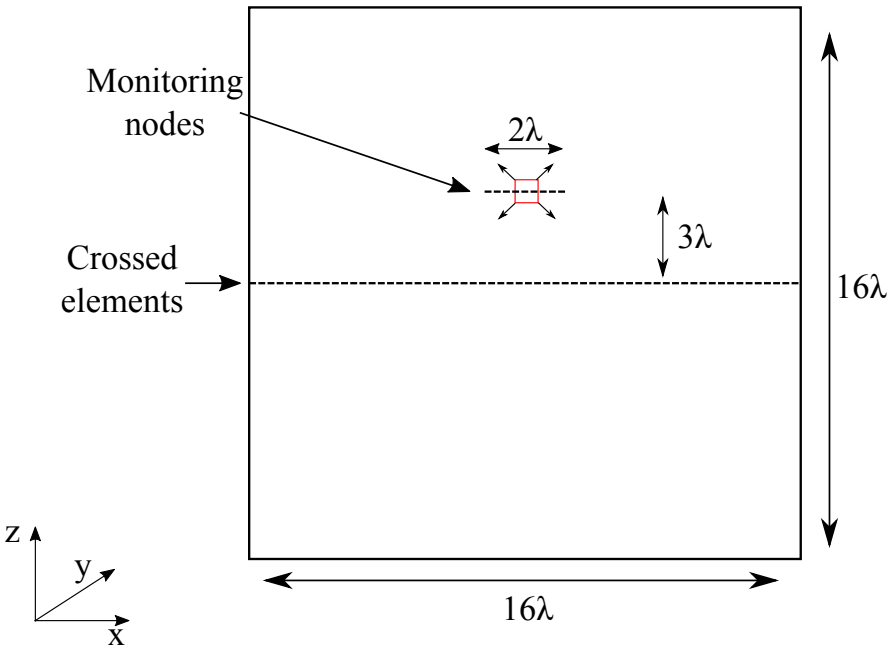
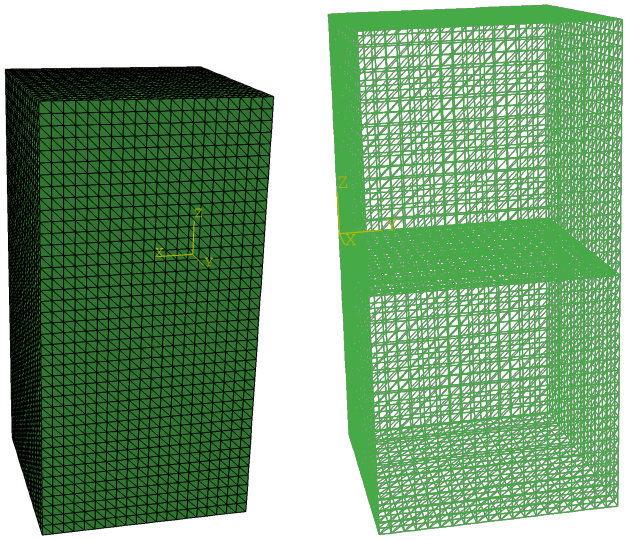


Figure 5.12: A 2D schematic of the 3D model used to measure the reflection from the crossed hypotenuses. The out-of-plane dimension is also 16 λ and the source point depicted in the figure is located in the centre of the x-y plane of the model.



(a) (b)

Figure 5.13: An image of (a) a solid model with only the exterior element boundaries showing and (b) a wire-frame model which shows the crossed hypotenuses on the tetrahedral elements. Images taken in ABAQUS CAE.

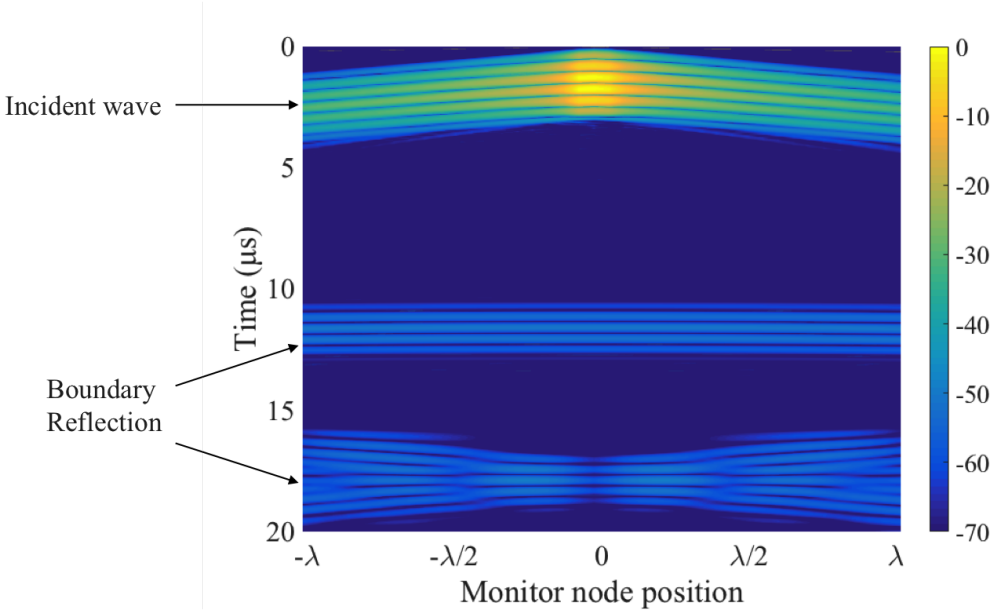


Figure 5.14: An uncorrected B-scan image of the displacement-time histories recorded at along a line of monitor nodes. The line of nodes are parallel to the x-axis and are located at the centre of the monitoring surface.

of the model, the superposition of the reflections from four model boundaries that are equidistant from the point source creates an interference pattern at this point in time. Any reflection from the crossed elements would have a round trip path length

of greater than or equal to 6 λ, corresponding to an arrival time of 6 µs. There is clearly no visible reflection at this arrival time or later with an amplitude greater than −70 dB relative to a single point source incident wave amplitude. From this result, it was concluded that the requirement to have parallel hypotenuses within the mesh could be relaxed.

5.4 Hybrid Simulation

The hybrid simulation follows the methodology outlined in subsection 4.4.2; a schematic of the procedure is given in figure 5.15. The Huygens-Fresnel beam model is employed for the forward process of simulating the propagation of the incident wave to the defect domain. To reduce the number of models, the e-scan (discussed in section 5.2) was simulated directly, as opposed to the FMC mode used in experiment. These two approaches are equivalent when the FMC data is post-processed to produce an e-scan of the same parameters [42]. The array sub-aperture size for the e-scan was 10 array elements and the incident shear wave beam angle was chosen as 45°. In the Huygens model, the appropriate time delays were applied to each element in the sub-aperture to generate a 45° shear wave within the stainless steel sample, calculated according to Snell's law. The array parameters used for the model were the same as the parameters of the array used for the experiment given in section 5.2.

A detailed illustration of the defect domain FE model is given in figure 5.16. The tetrahedral mesh of the defect generated by the Simpleware FE Grid meshing tool is labelled on the figure and along with its dimensions. The mesh surrounding this is appended by the custom mesh appending algorithm. The x-z extent of the hybrid monitoring surface is 16×14 mm and it is located at a height of 4.2 mm above the backwall. The dimensions of the FE defect domain are given on figure 5.16, where the dimensions are inclusive of absorbing layers but they are omitted from the figure for clarity. The time step used in the model was 1.5 ns and optimised SRM absorbing layers surrounded the defect domain model with a thickness of λ_L. As opposed to the model in subsection 4.4.2 where the excitation plane was perpendicular to the incident wave direction, the excitation plane inside the defect domain is now parallel to the backwall to reduce the size of the FE model. Subsection 3.4.2 provides validation that this does not significantly impact the accuracy of the incident wave reconstruction within the defect domain FE model. The excitation

plane extends across the entire x-z extent of the model which ensures that the edge effects are suppressed by the absorbing layers and is located at 4.4 mm above the backwall. The FE models were completed using Pogo.

To correctly position the defect in the simulation, the distance from boundaries of the CT coupon to the edges of the original test piece were measured because the boundaries of the test pieces were used as datum points in the experimental data collection. However, the boundaries of the CT coupon are not present in the resulting mesh of the defect due to the bespoke segmentation process. Therefore, the mesh was positioned within the model by measuring the distance of two distinct features of the defect on the CT coupon to the boundary of the coupon. The equivalent positions on the mesh were located enabling all nodal locations within the mesh to be referenced back to the test piece geometry through a coordinate transform. The distances from the distinct defect features to the boundary of the CT coupon were measured using an Alicona optical microscope; figure 5.17(a) and 5.17(b) show the Alicona measurement. Although the precision of the Alicona is 0.05 µm, a repeat measurement for each result showed agreement to within 0.1 mm. The selected points on the mesh that coincide with the features selected on the CT coupon are shown in figure 5.17(c). There is clearly uncertainty involved in selecting the correct

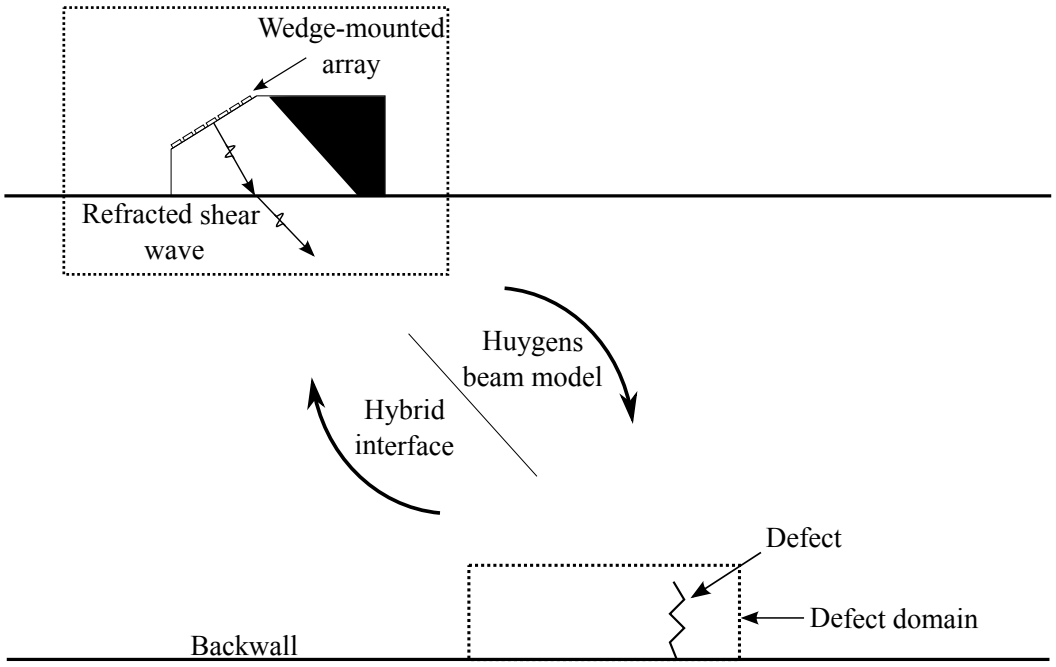


Figure 5.15: A 2D schematic of the 3D hybrid model procedure for simulating the inspection of a surface-breaking defect.

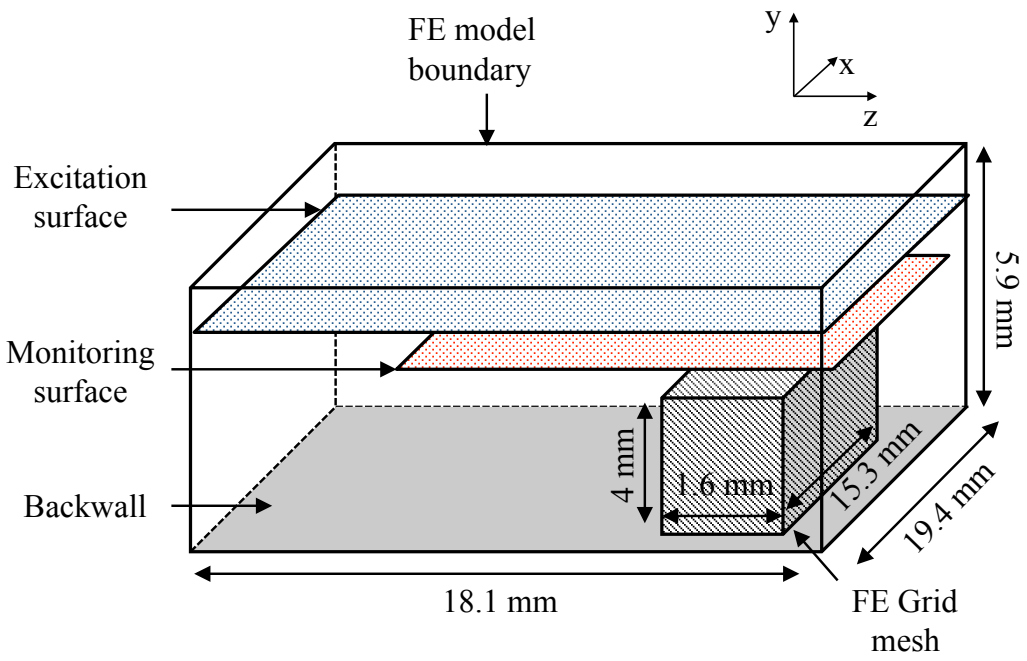
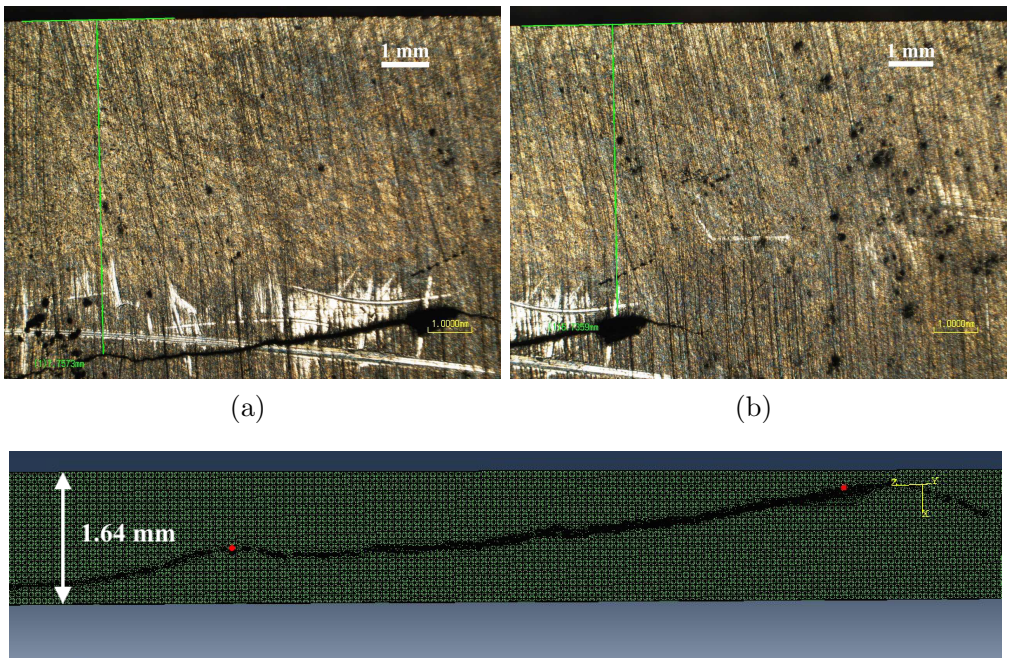


Figure 5.16: A schematic of the defect domain for the hybrid simulation.



(a) (b)

(c)

Figure 5.17: Images (a) and (b) show an Alicona optical microscope measurement of two distinct features on the defect to the boundary of the coupon and (c) shows the corresponding locations on the defect mesh, taken from ABAQUS CAE.

position on the mesh of the defect; the features extend approximately 1 mm, leading to an uncertainty of this order on the positioning of the mesh. On application of the

coordinate transform, the rotation was neglected due to limitations in the custom mesh appending algorithm. As the neglected rotation was 2°, this was viewed as a reasonable approximation.

As before, the hybrid interface is used to propagate the scattered wave field to all points on the bottom surface of the wedge (figure 4.10). The x-z extent of the wedge surface is $20.5 \times 61.5\,\text{mm}$ and it is located at a height of 20 mm above the backwall i.e. on the inspection surface. The Huygens-Fresnel beam model is again employed to propagate the scattered wave back through the wedge, which is again Perspex and has a longitudinal wave speed of $2680\,\text{m}\,\text{s}^{-1}$ and density of $1180\,\text{kg}\,\text{m}^{-3}$. The dimensions of the array element are given in section 5.2. The scattered wave is propagated back to each element in the sub-aperture of the array and the appropriate delay laws were applied, equal to those calculated for transmission.

5.5 Results and Discussion

As detailed in section 5.2, the array transducer was scanned along the length of the defect (figure 5.3) and FMC data was acquired at each scan increment. This enables a B-scan image (described in subsection 4.4.1) to be generated from the FMC data at each scan increment. Due to the size of the defect in the simulation, it was only feasible to simulate a single B-scan from the experimental data collection using the hybrid model. The B-scan selected for simulation was chosen based on the presence of features on the image that were visible above the noise and distinct from the corner trap indication. This enables the relative amplitude of the features on the experimental image to be compared to the simulated image to provide a measure of the model accuracy. A discussion of the origin of these features is given below, however it is noted that the distinct diffraction features used for comparison in subsection 4.4.3 are not visible above the noise in the B-scan images generated from the FMC data. It is suspected that this is a result of the increased complexity of the defect morphology in comparison to the notch simulated in subsection 4.4.2 and has led to the study performed in the next section.

The B-scan generated from the FMC data collected experimentally is plotted in figure 5.18. The FMC data was post-processed to generate a 45° shear wave B-scan with a sub-aperture of 10 array elements. No focusing was applied and an array firing delay of 0.567 µs was accounted for in the image. The data are normalised to the

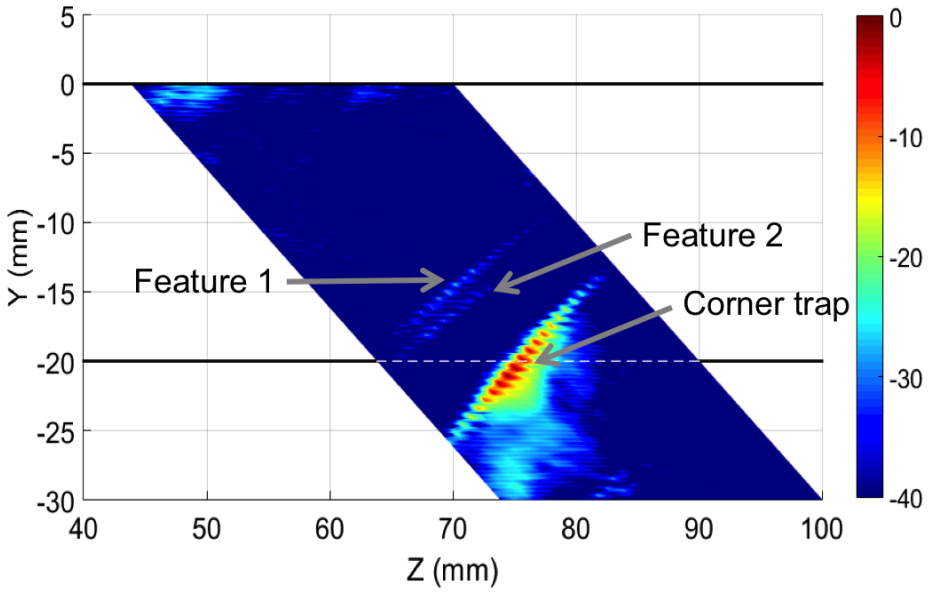


Figure 5.18: The 45° shear wave B-scan generated from the experimental FMC data. The sub-aperture size is 10 elements and no focusing was applied. In addition to the corner trap, two distinct features have been labelled on the image.

maximum on the image and plotted in a decibel scale. The inspection surface and backwall are overlaid on the image at 0 mm and −20 mm in the y-axis, respectively. The corner trap signal clearly appears in the image and has been labelled in the figure; the coordinates of the maximum of the corner trap is given in table 5.2.

There are also two distinct features present in the B-scan that have been labelled in the figure. The origin of these signals is unclear as they occur in a position on the image which is not characteristic of tip diffraction. This highlights some key limitations of the B-scan imaging technique. For example, the B-scan image assumes that the incident wave radiates from the probe or wedge index point and does not incorporate beam width of spreading. In addition, it is assumed that the incident and scattered angles of the ultrasonic wave are constant, which in this case is 45°. For a geometrically simple scatterer, such as an artificial notch, interpretation of the B-scan image is trivial, such as the description given in subsection 4.4.3, which

Table 5.2: Comparison of features on the experimental and simulated B-scan images.

	Corner Trap		Feature One		Feature Two	
	Simulation	**Experiment**	**Simulation**	**Experiment**	**Simulation**	**Experiment**
Coordinates (z,y) (mm)	(74,-20)	(74,-21)	(68,-15)	(70,-14)	(70,-15)	(68,-18)
Amplitude (dB)	N/A	N/A	-31	-27	-30	-29

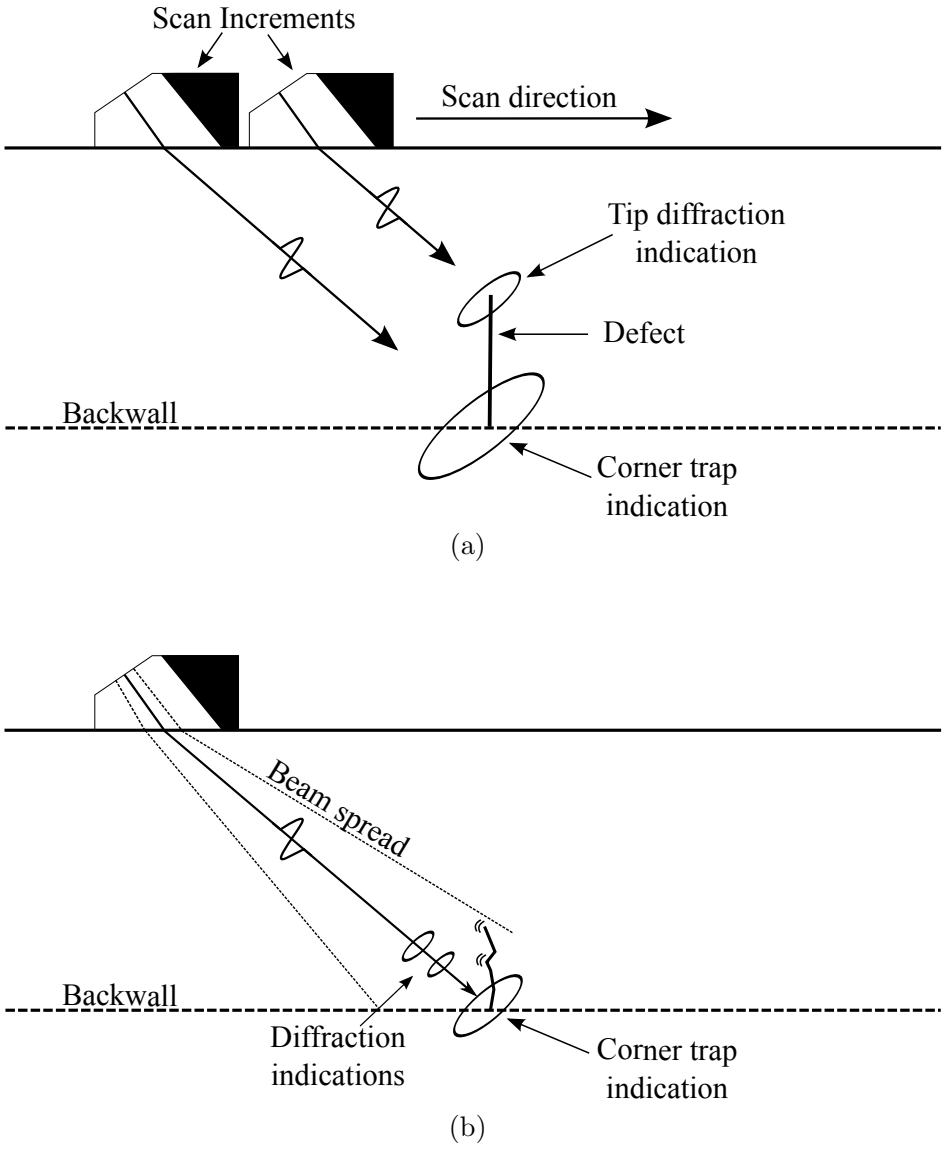


Figure 5.19: A Schematic of the generation of a B-scan image. (a) shows the origin of the corner trap indication and the tip diffraction indication as a transducer is scanned over the defect in a line scan. (b) depicts the effect of the beam width on the B-scan image and shows that signals scattered from complex defect features may be mis-plotted.

is summarised by figure 5.19(a). However, the distinct features which are seen on figure 5.20(b) may be as a result of the finite beam width leading to insonfication of facets on the defect. This is illustrated by figure 5.19(b); due to the limitation of the B-scan imaging technique, these features are plotted along an incorrect ray path causing ambiguity in interpretation.

Regardless of their origin, the features provide a way to compare the accuracy of the hybrid simulation to experiment. The location and amplitude relative to the

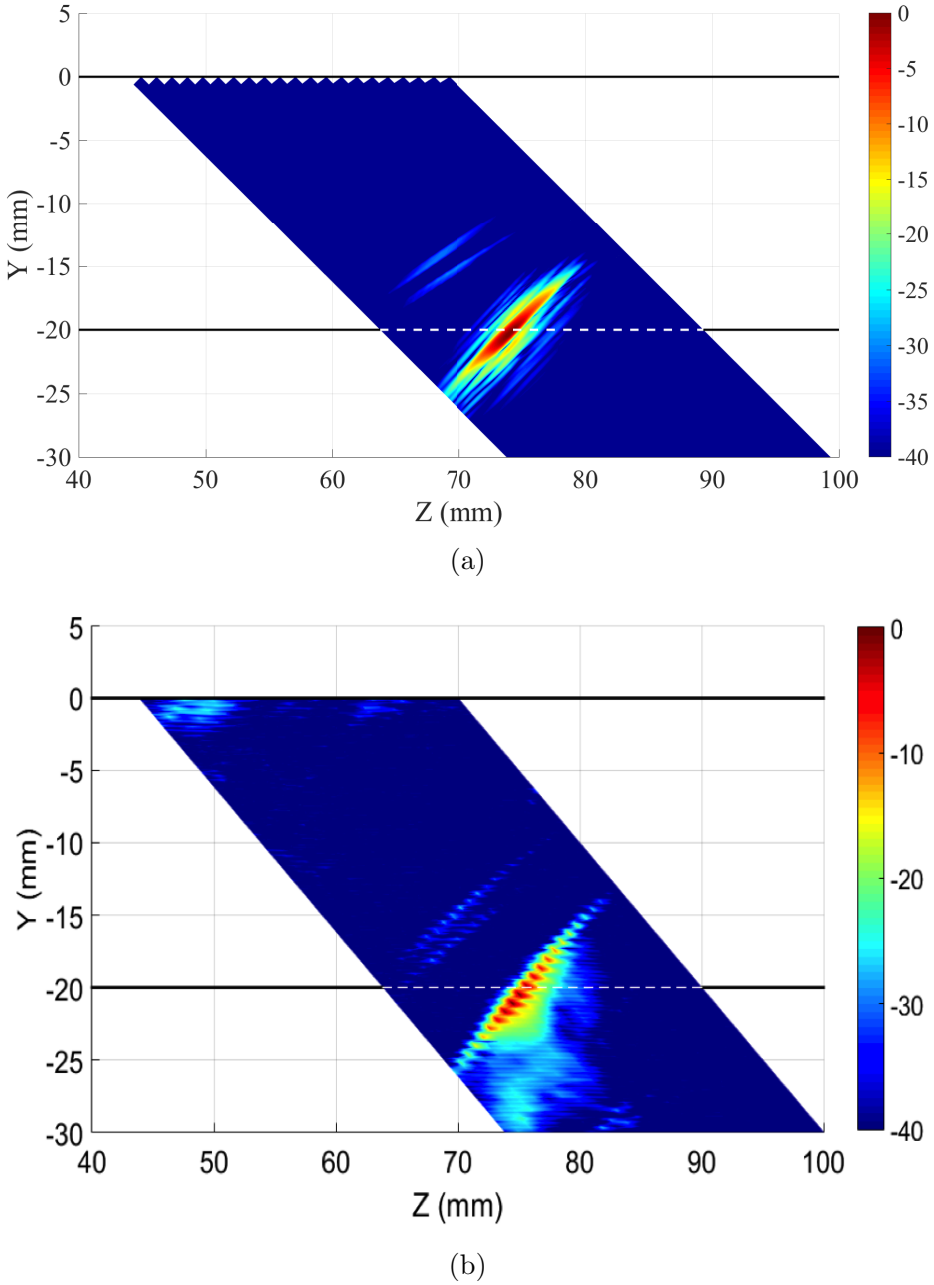


Figure 5.20: The B-scan image generated by the hybrid simulation is shown in (a). The experimental B-scan image has been repeated in (b) for comparison to (a)

corner trap of the features on the experimental B-scan image are given in table 5.2.

The B-scan calculated by the hybrid model for the equivalent scan location is plotted in figure 5.20(a). For reference, the experimental B-scan image is repeated in figure 5.20(b). The data in the image are also normalised to the maximum of the corner trap and converted to a decibel scale. The hybrid simulation has predicted the features on the B-scan image with good accuracy. The location of the maximum

amplitude of the corner trap feature in figure 5.20(a) has been given in table 5.2 and is agreement with experiment to within 1 mm. The amplitude and location of the two distinct features in the B-scan image have also been given in the table. Both features are in good agreement with experiment. An error in the coordinates of feature one of 2 mm and 1 mm in the z and y-directions is observed, respectively. Furthermore, an error of 2 mm and 3 mm in the z and y-directions respectively of feature two is observed which may arise from neglecting the 2° skew of the defect for the hybrid simulation, as well as the from error in referencing the defect mesh to the boundary of the sample. Further experimental errors may also account for the discrepancy, such as an index point offset and incorrect measurement or generation of the 45° beam angle. The 'sawtooth' effect on the experiment data results from the the poor performance of the image interpolation used to create a smoother image, which is due to the reduced sampling frequency of the experimental data (100 MHz) in comparison to the simulated data (320 MHz)

The amplitudes of the features are in good agreement with experiment. An error of 4 dB and 1 dB is observed between hybrid and experiment for feature one and feature two, respectively. Although it is difficult to identify the sources of error for the amplitude discrepancy, if the features are due to diffraction, it is likely that the amplitude is affected by the accuracy of the defect geometry obtained from the CT data. The spatial sampling of the geometry was increased from 6 µm to 40 µm on the basis of increasing the computational efficiency whilst still ensuring the mesh density is small enough for accurate simulation of ultrasonic wave propagation [10]. However, there has been no previous work to understand the effect of surface discretisation on the diffraction from a complex or 'rough' crack tip. It is therefore unclear whether the diffraction is correctly simulated at the spatial sampling used for this model, although the magnitude of error is typical when comparing modelled and experimental data. Surrounding the corner trap feature are a series of low amplitude signals whose origins are unclear. It is suspected that these are as a result of the ultrasonic interaction with the complex defect and may be from discretising the defect geometry or are not visible in the experimental data due to the presence of noise.

By comparing the B-scans in figure 5.20(b) and figure 5.20(a), it is clear that the hybrid model provides a very good estimation of the complex scattering from a true defect.

5.6 Influence of Tip Shape

In the previous section, it was discussed that the typical tip diffraction indication on the B-scan image was not present for the experimental data captured on the thermal fatigue defect. This was confirmed by the hybrid simulation, as well as the appearance of low amplitude features on the image which are suspected to be as a result of diffraction from features of the complex defect morphology that are insonified by the spreading of the incident wave. This is in contrast to the B-scan image obtained from a line scan over the EDM notch, shown in figure 4.11(b) and figure 4.11(a), where the tip diffraction indication is clearly visible with an amplitude of $-25\,\text{dB}$ relative to the corner trap indication in both the experimental and simulated results. It is therefore clear that the tip morphology plays a significant role on the amplitude of the diffracted ultrasound from the crack tip.

The use of an artificial defect, such as an EDM notch, is commonplace for determining the performance of an ultrasonic inspection [6], including for inspections that rely upon diffraction from the crack tip for defect detection or sizing. As discussed by Virkkunen *et al.* [4], it is likely that the radius of the tip of an EDM notch is large compared to a real crack and is therefore not an accurate representation of a true crack tip. In line with this observation, the results presented in section 5.5 also suggest that the amplitude of the diffracted waves is influenced by the tip morphology, however there is little information available in the literature that quantitatively evaluates this. Ravenscroft *et al.* [26] show that the diffraction from an artificial rectangular slot does not agree with predictions from GTD, whereas good agreement is found when comparing theory to the diffraction from the tip of a fatigue crack. It is concluded in the study that the initial disagreement is due to the shape of the slot tip. Chapman and Toft [135] discuss the differences between the diffracted ultrasound from the tip of a sharp crack and the edge of a Flat Bottom Hole (FBH) as FBHs are often used as target reflectors inspection design and qualification. The study employs both experimental and simulated data, including the work from Firth and Gould [136], and concludes that the diffracted wave amplitude from a FBH is higher than that from a sharp crack when considering the 'top tip', which is of interest to inner surface-breaking defects, whereas the the diffracted wave amplitude is smaller than for sharp crack when considering the 'bottom tip'. Chapman *et al.* attribute this to the fact that the FBH diffracting

edge is a 270° vertex, whereas for a sharp crack the diffracting edge is a 360° vertex. It is also noted in this work that the machining process by which the FBH was generated had an effect on the diffraction amplitude as this changed the sharpness of the diffracting vertex, yet this difference was not qualitatively defined.

For EDM notches to provide meaningful amplitude information on defect signals when qualifying an inspection, it is important to quantify any amplitude difference between a notch and a realistic defect morphology. This final section of work utilities 2D FE modelling to provide quantification of the amplitude difference in tip diffraction between an EDM notch and a sharp crack tip for P-E inspection techniques.

5.6.1 Simulation Methodology

A set of 2D FE simulations are used to measure the amplitude of the backscattered diffracted (back-diffracted) ultrasound from a rounded edge and a sharp vertex. Figures 5.21 and 5.22 contain a schematic of the models used to measure the diffraction from a closed tip and a rounded tip, respectively. The defect in figure 5.21 is represented by two inclined smooth stress-free boundaries which meet to create a sharp vertex, with a maximum opening of 10 µm at the mouth of the crack. As the defect

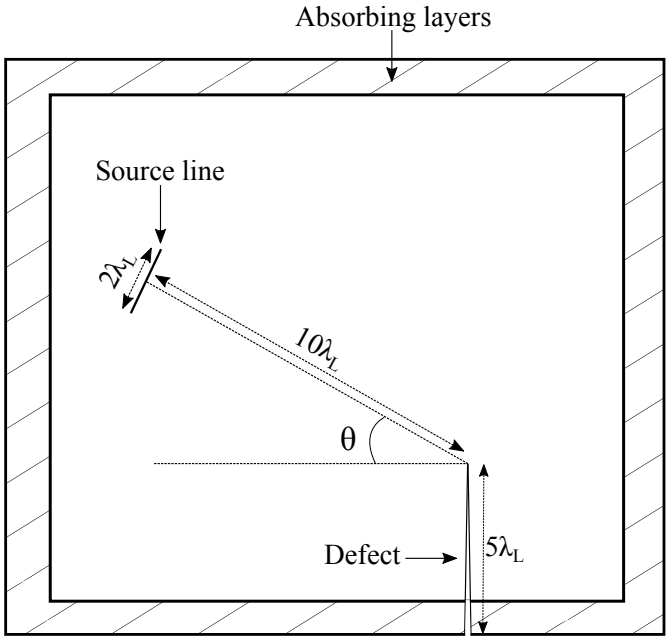


Figure 5.21: A Schematic of the 2D FE model for measuring the diffracted signal from a closed crack tip.

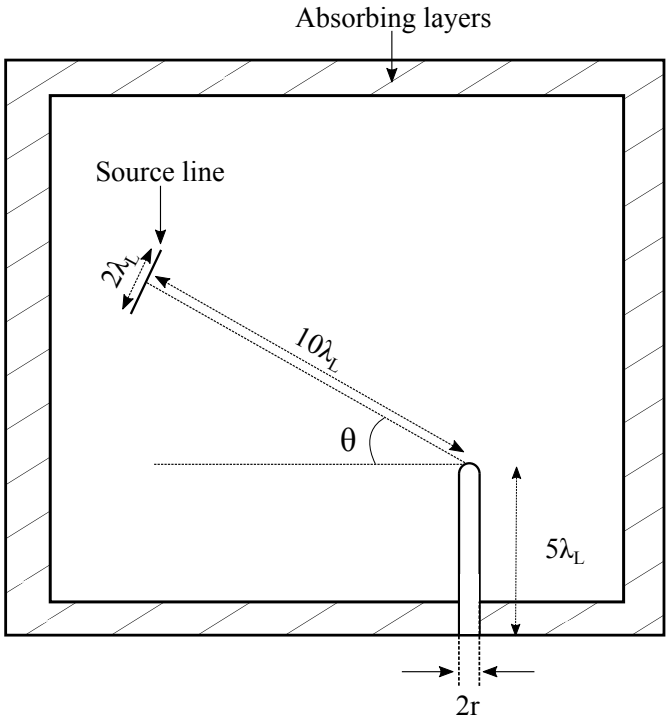


Figure 5.22: A Schematic of the 2D FE model for measuring the diffracted signal from a rounded notch tip.

opening is very small in comparison to the ultrasonic wavelength ($\approx \lambda_L/295$ and $\lambda_S/162$), it is assumed that the results are independent of this parameter. In figure 5.22, the defect is replaced by a notch, which is modelled by two parallel planar stress-free boundaries and the tip is semi-circular with radius, r. In subsection 4.4.2 it was confirmed that the tip of the EDM notch used for the experimental validation was semi-circular; however, it is noted that the tip shape of other artificial defects made by the EDM process or otherwise may vary from the semi-circular profile and therefore may require case specific studies to ensure the applicability of the results gathered here. The plane strain conditions are used in the 2D FE models and therefore the defects have infinite extent in the out-of-plane dimension.

The incident wave is generated by exciting a series of cylindrical point sources along a line of length $2\lambda_L$ at a distance of $10\lambda_L$ from the tip of each defect. Point sources are used to ensure modal purity and the distance from the tip ensures the sources are in the far field, reducing the edge effects of the source line. The source line is incrementally moved around an arc centred on the tip of the defect to investigate how the amplitude of the back-diffracted waves vary with respect to incident angle; the arc of incident angles ranges from 0° (normal to the defect surface) to 90° (parallel

to the defect surface) at increments of 5°.

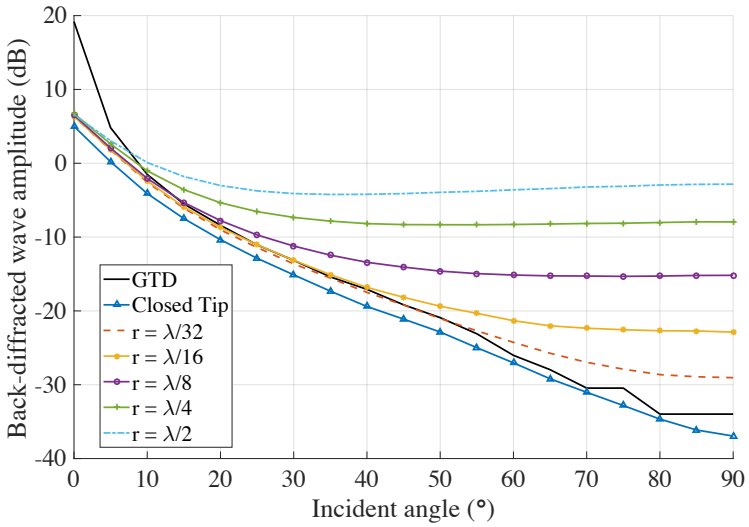
A 3 cycle 2 MHz tone burst excitation signal is applied to the point sources to generate the incident wave. To remove the dependency of the results on the incident wave frequency, the radius of the notch tip is varied; the radius is set as a fraction of the incident wavelength, such that $r = \lambda/2, \lambda/4, \lambda/8, \lambda/16, \lambda/32$. Using stainless steel material properties, this results in a range from 92 µm to 1.5 mm for an incident longitudinal wave and from 50 µm to 0.8 mm for an incident shear wave. This range covers the radius of curvature of the tip of the small notch used for the experimental validation in subsection 4.4.2, where the tip radius of putty replication of the notch was measured to be 150 µm. The models are repeated for both longitudinal and shear incident wave modes and mode conversion of the back-diffracted wave is not considered here.

The FE models were meshed using triangular elements in ABAQUS CAE with an edge length of 100 µm ($\lambda_L/30$) for the incident longitudinal wave model and 75 µm ($\lambda_S/22$) for the incident shear wave model. Within a small area surrounding the crack, an unstructured meshing algorithm was used to ensure conformity to the defect whereas structured right angle triangles were used everywhere else in the model, where the element edge length refers to the shortest side of the triangle. Optimised SRM absorbing layers with a thickness of $1.5\lambda_L$ surround the boundary of the model. The backscattered displacement is measured on a line of nodes extending the same width as the source line and the back-diffracted waves are extracted from the average of the displacement-time histories over all monitor nodes using a time window. The maximum amplitude of the rectified back-diffracted wave for each model is measured relative to the amplitude of the backscattered wave from a 3 mm diameter SDH at a distance of $10\lambda_L$ from the source line of length $2\lambda_L$; two 2D FE models of the SDH are required for each incident wave mode. The FE model properties of the SDH model are equivalent to those used for the diffraction models. Pogo was used to solve the FE models.

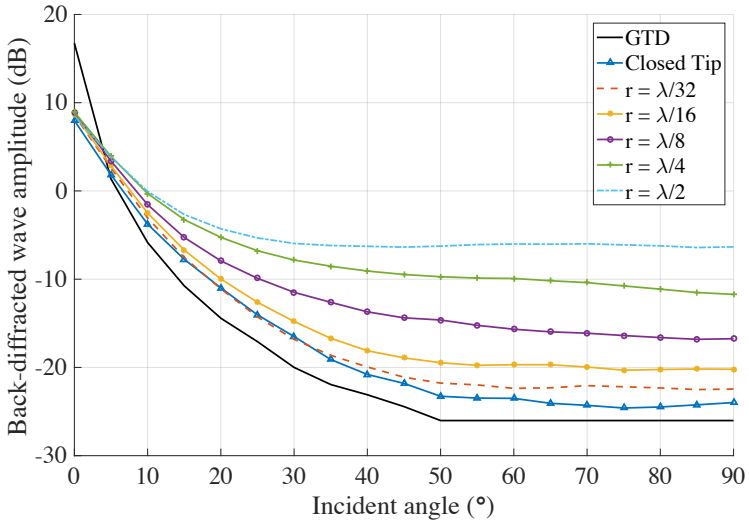
In order to evaluate the validity of this numerical simulation methodology, the results from a GTD simulation are also acquired. The results of the simulation are calculated relative to an approximate analytical SDH model presented by Ermolov [137].

5.6.2 Results and Discussion

The results from the longitudinal wave case are plotted in figure 5.23(a) and the shear wave case in figure 5.23(b). In general, both wave modes follow the same trend; the back-diffracted wave amplitude at 0° is larger than the response from the SDH because it is indistinguishable in time from the direct specular reflection. The



(a)



(b)

Figure 5.23: The back-diffracted wave amplitude relative to a 3 mm SDH for (a) an incident longitudinal wave and (b) an incident shear wave. In the legend, r refers to the radius of the semi-circular tip of of the notch in the FE simulations.

amplitude becomes weaker with increasing angle of incidence as the diffracted wave becomes distinguishable from the specular reflection and falls below 0 dB after an incident angle of approximately 10°. Following this, the back-diffraction amplitude tends to plateau where the amplitude of the plateau is dependent upon the radius of the notch tip, such that the smaller the tip radius the weaker the back-diffracted signal becomes. Furthermore, the amplitude of the back-diffracted wave from the closed tip generally follows the amplitude of the wave diffracted from the tip with a radius of $\lambda/32$ across all angles for the shear wave mode, whereas the curves tend to diverge at higher angles for the longitudinal wave mode. In the longitudinal case, the largest difference between these two cases is 8 dB and occurs at 90°, whereas for the shear wave mode it is 2 dB at 75°.

For both wave modes, the diffracted wave amplitude from the closed defect is in good agreement with the GTD model. For the longitudinal case, agreement with the GTD model is also good for the tip with a radius of $\lambda/32$ from 15° until 55°. In the shear wave case, the GTD model predicts an amplitude that is consistently smaller than that predicted by the closed tip FE model by approximately 3 dB, where the largest discrepancy is 3.5 dB at 30°. Discrepancy between the FE and GTD models is expected and can be attributed to the differences in the assumptions made in the modelling approaches. For example, there will be a small impact of the edge effects of the incident wave in FE as it is of finite width, whereas a plane wave is assumed in the analytical model. Furthermore, the GTD model is a frequency-domain model whereas the FE model employs a broadband signal whose centre frequency matches the single frequency of the GTD model. For the 0° case where the specular reflection is dominant, the GTD model disagrees with the FE results. As discussed in subsection 2.2.2, GTD theory is known to break down when predicting the reflection from the defect surface therefore good agreement is not expected here.

The results clearly show that the radius of curvature of a notch significantly impacts the amplitude of the back-diffracted signal in comparison to the diffraction from a sharp crack tip. A tip radius of 150 µm is equivalent to approximately $\lambda_L/20$ and $\lambda_S/11$. For the incident longitudinal wave, this lies between the smallest two tip radii. In the worst case i.e. $\lambda_L/16$ at 90° incidence, this leads to a difference of 14 dB between the rounded notch and the sharp crack. However, this angle of incidence is rarely used in any ultrasonic inspection setup and a more common angle of incidence for the inspection of surface-breaking defects is 70°, which according to this study

would undergo an amplitude increase of 9 dB of the back-diffracted wave amplitude from a notch with a tip radius of $\lambda_L/16$ in comparison to the diffraction from a sharp crack tip. For the shear wave cases, the tip radius of 150 µm can approximated pessimistically by the $\lambda_S/8$ tip radius, which shows a maximum increase in amplitude of the back-diffracted wave in comparison to the sharp crack of 9 dB at 50°. At the common incident angle of 45°, the amplitude difference is 7 dB. It is likely that the cause of this increase in amplitude results from the scattering mechanism changing from a diffraction to a reflection and therefore as the tip radius is increased, a larger proportion of the wave is reflected back to the transducer. The amplitude difference quantified by this study is not insignificant and may cause already weak diffraction signals to fall below noise thresholds. It is therefore paramount that these amplitude factors are taken into account when using an artificial defect, such as an EDM notch, to design and qualify an inspection that utilises diffraction from the crack tip.

5.7 Conclusions

In this chapter, the hybrid model has been employed to simulate an ultrasonic inspection of a thermal fatigue defect, utilising XCT to measure and implement the morphology of the full defect into the simulation in a way that has not been previously achieved.

FMC data were collected on the test piece containing the thermal fatigue defect before the test piece was sectioned and XCT scanned. A voxel size of 6.08 µm was achieved on the sample and the defect geometry was extracted from the resulting images from the XCT data by a segmentation process which decomposed each image into multiple regions and employed different filters within those regions depending upon the visibility of the crack boundary. A mesh of a small volume surrounding the defect was generated using an algorithm based on the VOMACS meshing procedure; in order to extend the mesh to account for a region of the backwall required to correctly simulate the ultrasonic scattering, a structured tetrahedral mesh was appended to the VOMACS mesh. By running a simulation that included 'crossed' elements hypotenuses, it was found that the usual requirement for the hypotenuses of the tetrahedral elements that lay on the boundary of the VOMACS mesh to align with those on the appended mesh could be relaxed.

From the experimental FMC data, a 45° shear wave e-scan was generated by the

application of the appropriate delay laws to a subset of the data. The experimental results showed that the features resulting from tip diffraction that are typically visible on a B-scan image of a surface-breaking defect were not present in the data. The lack of these features was attributed to the complexity of the defect morphology in comparison to the artificial defect geometry. Furthermore, uncharacteristic features on the B-scan image were attributed to the insonification of complex features on the defect by the divergence of the incident beam.

The hybrid model was then used to simulate the e-scan and demonstrated remarkable accuracy in the estimation of the location and amplitude of the B-scan image features. It was found that the corner trap signal was in agreement to within 1 mm with experiment and a maximum error of 3 mm in the location of the uncharacteristic diffraction features was found. The amplitude of these features were also shown to be within 4 dB of the experimental data.

The validation of modelling tools is paramount to their deployment within industry, especially when the models have the potential to be used to aid in the design and justification of inspections on safety critical components. The result presented in this chapter provides a level of validation that has not previously been established for a modelling technique.

As a result of the observation made from the experimental B-scan image data, a set of 2D FE simulations were performed in order to quantify the difference in amplitude between the diffracted waves from a EDM notch with a semi-circular tip and the diffraction from a sharp crack tip. It was shown that for the 70° P-E longitudinal wave inspection, the back-diffracted wave from a notch with a representative tip radius of $\lambda_L/16$ was higher in amplitude by 9 dB than that from a sharp crack tip. In addition, for the 45° shear wave case the back-diffracted wave from a notch with a representative tip radius of $\lambda_S/8$ was 7 dB higher in amplitude than the back-diffracted wave form a sharp crack. The results from this study confirm the observations found in this chapter in comparison to the experimental results in subsection 4.4.2 that the diffraction from the tip of an artificial reflector is often higher in amplitude than the diffraction from a sharp crack tip and the results presented here can be used to provide an amplitude offset when designing and qualifying inspections.

Chapter 6

Conclusions

6.1 Summary

In this project, a hybrid analytical-FE model has been applied to the inspection of inner surface-breaking defects and validated against full numerical simulation and experimental data for both simple and complex defect morphologies. The benefits of the modelling approach are that the ultrasonic interaction with a complex geometry can be simulated without the need to discretise the entire inspection domain, increasing the computational efficiency. Combining this with recent developments in efficient GPU based solvers, the capability of numerical based simulation can be pushed further than previously possible and computational limits restricting the size of models can be, to some extent, lifted.

Chapter 1 covered the motivation for this work and highlighted the need for an improved inspection modelling technique to assist in the development and justification of ultrasonic inspections performed on safety critical NSRP components, specifically the components that are suspected to contain inner surface-breaking defects. Chapter 2 reviewed common ultrasonic inspection techniques employed for the detection and characterisation of surface-breaking defects, ranging from the angled shear wave inspection to ultrasonic arrays. In addition, the theoretical foundation of the inspection models commonly employed within the nuclear power generation industry were reviewed, such as the Born Approximation, the Kirchhoff Approximation and GTD. Numerical simulations methods were also discussed, focusing on the use of FE for ultrasound simulation before moving on to a discussion of recent hybrid modelling techniques. It was reported that the hybrid model developed by re-

searchers at Imperial College was selected for use within this project; the application of this technique to the simulation of the ultrasonic inspection of surface-breaking defects is the focus of chapters 3, 4 and 5.

In chapter 3, the linkage of a simple Huygens-Fresnel semi-analytical beam model to the FE domain of the hybrid model was reported. The motivation for this was to move away from the use of FE to simulate the transducer, as there are many well established and computationally efficient semi-analytical approaches. Due to the nature of the Huygens model, excitation within the FE domain requires the output of the model to be applied to a series of secondary point sources. Although trivial in 2D, the 3D shear wave model required further investigation; by exploiting the shear wave polarisation, it was found that the approximate FE point source approach provided an acceptable secondary source for generating the incident wave. The validity of this approach for longitudinal and shear waves in 3D was demonstrated by comparison to the commercial software CIVA, where good agreement was found. This technique is attractive as it provides a simple yet versatile way to simulate an incident wave generated by an arbitrary transduction system.

In chapter 4 a methodology was developed to simulate the ultrasonic inspection of surface-breaking defects using the 3D hybrid model. By considering the scattering mechanisms present in an angled beam inspection, it was shown that it is possible to estimate the region of backwall required in the simulation to accurately model the ultrasonic inspection. Good agreement against a full FE simulation of the scattering from both a smooth and rough surface-breaking defect under plane wave incidence was found. Experimental validation was provided by simulating a line scan over a smooth rectangular EDM notch using a monolithic transducer. The corrected B-scan images were compared, with good agreement in both relative amplitude and location of the image features. The hybrid model was then used to perform a Monte Carlo study to investigate the attenuation due to roughness on the ultrasound field scattered from a surface-breaking defect. It was shown that at low levels of roughness, the mean ultrasonic attenuation agreed well with the widely used KA, however at high levels of roughness KA was shown to over-estimate the attenuation, which is in agreement in recent studies in the literature on embedded defects. By analysis of the confidence bands on the Monte Carlo results, it was observed that KA also underestimates the attenuation at low defect roughness for a significant fraction of the defect population, highlighting that care should be taken when using

KA to assess the impact of surface roughness on ultrasonic response.

Chapter 5 reported on the use of the hybrid model to simulate an ultrasonic inspection of a thermal fatigue defect by employing XCT to obtain an accurate representation of the true defect morphology. The test piece containing the defect was scanned using an ultrasonic array before it was sectioned to remove excess material around the defect. An XT H 320 rotating target X-ray CT system was used to take the measurements, resulting in a voxel size of 6 µm. Image segmentation was performed by applying various segmentation methods to different regions on the image to extract the defect surface profile, which was then used to generate a FE mesh at a nodal density of $\lambda_S/20$. The experimental data were processed to generate a B-scan image from a 45° shear wave scan; the hybrid simulation was employed to simulate this scan using the entire 3D FE mesh generated from the XCT measurements. The resulting B-scan images were compared and, in general, excellent agreement was found. Features on the image which are uncharacteristic of a 45° shear wave B-scan were observed on both the experimental and the simulated data and were attributed to diffraction from complex features on the defect. The location of the corner trap signal was in agreement to within 1 mm with experiment and a maximum error of 3 mm in the location of the uncharacteristic diffraction signals was found. The amplitude of these features predicted by the simulation was also shown to be within 4 dB of the experimental data. As a result of the observation made from the experimental B-scan image data, a set of 2D FE simulations were performed in order to quantify the difference in amplitude between the diffracted waves from a EDM notch with a semi-circular tip and the diffraction from a sharp crack tip. It was found that there is an amplitude difference on the order of 9 dB between the backscattered diffracted wave from a typical notch tip radius and a sharp crack tip.

In summary, this work has extended the functionality of a hybrid technique to simulate the inspection of surface-breaking defects. In addition, an arbitrary transduction system has been incorporated, enabling the model to be more broadly applied to the simulation of ultrasonic inspections of plant components. Validation evidence demonstrates that the hybrid model accurately predicts the ultrasonic scattering from a well-characterised reflector. Furthermore, validation on a real defect provides a high level of confidence that the model can be used to assess and quantify the performance of inspections where qualification becomes challenging. This work

has made a clear step forward in the use of simulation for inspection qualification.

6.2 Further Work

This work has extended the functionality of a hybrid modelling approach in both the transduction and the defect interaction modules of the model. In both areas, there are multiple ways in which the model could be extended to cover a wider range of inspection and defect types.

As discussed in section 3.5, the semi-analytical beam model is limited to the simulation of a single wave mode. However since no mode conversion can occur in the free space of the component material, the wave modes can be treated separately and the beam model could be run multiple times to consider multiple wave modes, with the excitation of the secondary sources for all wave modes in the FE model superposed. Furthermore, the beam model could be extended to account for the excitation through a curved component surface, such as a pipe, or to account for focused beams. In addition to these extensions, it would also be beneficial to investigate the ability of the secondary sources to re-excite the incident wave around a curved surface, rather than over a planar surface, and how the accuracy of the re-excited wave is dependent on the radius of curvature of the excitation surface. This would allow for the model size to be reduced, especially when a reflection from the component backwall is required.

The work in chapter 4 provided a methodology to simulate the angled shear wave inspection using the hybrid model. It would be beneficial to evaluate the accuracy of this methodology to other inspection techniques and to provide experimental validation, such as for the ToFD and creep wave inspections. It is suspected that the methodology proposed in chapter 4 would be suitable, however further investigation would be necessary to determine the region of backwall required in the simulation. The application of this simulation technique could also be extended to other areas of interest within the nuclear sector, such as Stress Corrosion Cracking (SCC) and water-filled defects. The complexity of SCC would impact on the ultrasonic interaction with the defect and the back wall and may impact on the validity of the hybrid model methodology proposed in this work, therefore presenting a valuable area of research. Furthermore, as the study into the attenuation due to roughness performed in section 4.5 has been carried out for a specific inspection frequency and defect size,

it would be beneficial to develop a more general methodology for surface-breaking defects and compare the result to the embedded defect case to understand whether the presence of the backwall influences the result.

Finally, the work in chapter 5 pushed the capability of current modelling techniques to simulate an ultrasonic inspection of a thermal fatigue defect using an accurate representation of the real defect morphology. It is recommended that validation of this type should be repeated for multiple different defects and inspection techniques to build the confidence in this modelling approach and to enable a regime of validity to be established for the techniques required to simulate increasingly complex inspection scenarios. Further work is suggested on the investigation into the influence of tip morphology on the diffracted ultrasonic waves; the work carried out in section 5.6 could be extended to the 'bottom tip' case, where it has been found in previous experimental work [7] that the diffraction rounded tip is weaker in comparison to a sharp tip. Furthermore, 3D simulations could be used to quantify the effect of out-of-plane defect features on the diffraction signal, such as skew and semi-elliptical geometry. In figure 5.8, the thermal fatigue defect morphology was presented and discussion on the complexity of the defect tip was given. Although the effect of roughness on the scattering from a defect surface has been the subject of much research, it would beneficial to understand and quantify the effect of the complex tip morphology on tip diffraction signals in order to better inform the design and justification of ultrasonic inspections that rely on the tip diffraction signal.

References

[1] R. Halmshaw. *Non-Destructive Testing*. Arnold, 2nd edition, 1991.

[2] Institute for Energy and Transport. European Methodology for Qualification of Non-destructive Testing Third Issue. Technical report, European Network for Inspection Qualification, 2008.

[3] J. Wåle and P. Ekström. Crack Characterisation for In-service Inspection Planning. Technical report, Swedish Nuclear Power Inspectorate (SKI), 1995.

[4] I. Virkkunen, M. Kempainen, H. Ostermeyer, R. Paussu, and T. Dunhill. Grown cracks for NDT development and qualification. *Insight: Non-Destructive Testing and Condition Monitoring*, 51(5):271–275, 2009.

[5] M. Kemppainen, I. Virkkunen, J. Pitkänen, R. Paussu, and H. Hänninen. Advanced flaw production method for in-service inspection qualification mock-ups. *Nuclear Engineering and Design*, 224(1):105–117, 2003.

[6] Institute for Energy and Transport. ENIQ Recommended Practice 5: Guidelines for the Design of Test Piece and Conduct of Test Piece Trials. Technical report, European Network for Inspection and Qualification, 2011.

[7] R. K. Chapman. A system model for the ultrasonic inspection of smooth planar cracks. *Journal of Nondestructive Evaluation*, 9(2-3):197–210, 1990.

[8] J. A. Ogilvy and I. D. Culverwell. Elastic model for simulating ultrasonic inspection of smooth and rough defects. *Ultrasonics*, 29:490–496, 1991.

[9] F. Shi. *Elastic wave scattering from randomly rough surfaces*. PhD thesis, Imperial College London, 2016.

[10] M. Drozdz. *Efficient finite element modelling of ultrasound waves in elastic media*. PhD thesis, Imperial College London, 2008.

[11] J. Pettit. *Modelling the Ultrasonic Response From Rough Defects Using Efficient Finite Element Modelling Techniques*. PhD thesis, Imperial College London, 2015.

[12] S. Mahaut, N. Leymarie, C. Poidevin, T. Fouquet, and O. Dupond. Study of complex ultrasonic NDT cases using hybrid simulation method and experimental validations. *Insight - Non-Destructive Testing and Condition Monitoring*, 53(12):664–667, 2011.

[13] A. Velichko and P. Wilcox. A generalized approach for efficient finite element modeling of elastodynamic scattering in two and three dimensions. *The Journal of the Acoustical Society of America*, 128(3):1004–14, 2010.

[14] P. Rajagopal, E. Skelton, W. Choi, M.J.S. Lowe, and R. V. Craster. A generic hybrid model for bulk elastodynamics, with application to ultrasonic nondestructive evaluation. *IEEE Transactions on Ultrasonics, Ferroelectrics and Frequency Control*, 59(6):1239–1252, 2012.

[15] J. L. Rose. *Ultrasonic Waves in Solid Media*. Cambridge University Press, 2004.

[16] J. D. Achenbach. *Wave propagation in elastic solids*. North Holland Pub. Co., Amsterdam, 1973.

[17] P. P. Milella. *Fatigue and corrosion in metals*. Springer Milan, Milano, 2013.

[18] J. Schijve. *Fatigue of structures and materials*, volume 25. Elsevier, 2nd edition, 2009.

[19] F. Cattant, D. Crusset, and D. Féron. Corrosion issues in nuclear industry today. *Materials Today*, 11(10):32–37, 2008.

[20] K. H. Grote and E. K. Antonsson. *Springer Handbook of Mechanical Engineering*. Springer, 2009.

[21] A. S. Birks and R. E. Green. Ultrasonic testing. In *Handbook of Non Destructive Testing*. American Society for Nondestructive Testing, 2nd edition, 1991.

[22] B. A. Auld. General electromechanical reciprocity relations applied to the calculation of elastic wave scattering coefficients. *Wave Motion*, 1(1):3–10, 1979.

[23] J. Krautkrämer and H. Krautkrämer. *Ultrasonic Testing of Materials*. Springer Berlin Heidelberg, Berlin, Heidelberg, 1990.

[24] J. B. Keller. Diffraction by an Aperture. *Journal of Applied Physics*, 28(4):426, 1957.

[25] M. G. Silk and B. H. Lidington. The potential of scattered or diffracted ultrasound in the determination of crack depth. *Non-Destructive Testing*, 8(3):146–151, 1975.

[26] F. Ravenscroft, K. Newton, and C. Scruby. Diffraction of ultrasound by cracks: comparison of experiment with theory. *Ultrasonics*, 29(1):29–37, 1991.

[27] J. A. Ogilvy and J. A. G. Temple. Diffraction of elastic waves by cracks: application to time-of-flight inspection. *Ultrasonics*, 21(6):259–269, 1983.

[28] R. K. Chapman and J. M. Coffey. A theoretical model of ultrasonic examination of smooth flat cracks. *Review of Progress in Quantitative Nondestructive Evaluation*, pages 151–162, 1984.

[29] J. D. Achenbach, A. K. Gautesen, and H. McMaken. *Ray Methods For Waves in Elastic Solids: with Applications to Scattering by Cracks*. Pitman Advanced Pub. Program, London, 1982.

[30] J. D. Achenbach and A. K. Gautesen. Geometrical theory of diffraction for three D elastodynamics. *The Journal of the Acoustical Society of America*, 61(2):413–421, 1977.

[31] A. K. Gautesen, J. D. Achenbach, and H. Mcmaken. Surface-wave rays in elastodynamic diffraction by cracks. *Journal of Acoustical Society of America*, 63:1824–1831, 1978.

[32] J. M. Coffey and R. K. Chapman. Aplication of elastic scattering theory for smooth flat cracks to the quantative prediction of ultrasonic defect detection and sizing. *Nuclear Energy*, 22(5):319–333, 1983.

[33] K. J. Langenberg, P. Fellinger, and R. Marklein. On the nature of the so-called subsurface longitudinal wave and/or the surface longitudinal "creeping" wave. *Research in Nondestructive Evaluation*, 2(2):59–81, 1990.

[34] D. E. Bray. Stress measurement using critically refracted longitudinal waves. *The Journal of the Acoustical Society of America*, 108(5):2594–2594, 2000.

[35] I. N. Ermolov. Progress in the theory of ultrasonic flaw detection. Problems and prospects. *Russian Journal of Nondestructive Testing*, 40(10):655–678, 2004.

[36] BS EN 2285:2017 Non-destructive testing of welds Ultrasonic Testing Testing of welds in austenitic steels and nickel-based alloys, 2017.

[37] M. Cerri and R. Cusolito. Experiences in capability assessment of manual ultrasonic examination techniques for planar flaw detection and sizing in austenitic stainless steel joints. *NDT International*, 22(4):229–239, 1989.

[38] S. Baby, T. Balasubramanian, and R. J. Pardikar. Ultrasonic study for detection of inner diameter cracking in pipeline girth welds using creeping waves. *International Journal of Pressure Vessels and Piping*, 80(2):139–146, 2003.

[39] ASTM E2192-13, Standard Guide for Planar Flaw Height Sizing by Ultrasonics, 2013.

[40] P. B. Nagy, M. Blodgett, and M. Golis. Weep hole inspection by circumferential creeping waves. *NDT & E International*, 27(3):131–142, 1994.

[41] S. R. Seshadri. Leaky Rayleigh waves. *Journal of Applied Physics*, 73(8):3637–3650, 1993.

[42] B. W. Drinkwater and P. D. Wilcox. Ultrasonic arrays: A comparison between medical and NDE requirements. In *AIP Conference Proceedings*, volume 975, pages 770–777. AIP, 2008.

[43] E. Ginzel. *Phased Array Ultrasonic Technology.* Eclipse Scientific Products Inc, 2nd edition, 2013.

[44] B. W. Drinkwater and P. D. Wilcox. Ultrasonic arrays for non-destructive evaluation: A review. *NDT & E International*, 39(7):525–541, 2006.

[45] C. Holmes, B.W. Drinkwater, and P. D. Wilcox. Post-processing of the full matrix of ultrasonic transmitreceive array data for non-destructive evaluation. *NDT & E International*, 38(8):701–711, 2005.

[46] M. V. Felice, A. Velichko, and P. D. Wilcox. Accurate depth measurement of small surface-breaking cracks using an ultrasonic array post-processing technique. *NDT and E International*, 68:105–112, 2014.

[47] C. Zhang, P. Huthwaite, and M. Lowe. The Application of the Factorization Method to the Subsurface Imaging of Surface-Breaking Cracks. *IEEE Transactions on Ultrasonics, Ferroelectrics, and Frequency Control*, 65(3):497–512, 2018.

[48] P. M Morse and K. U. Ingard. *International Series in Pure and Applied Physics: Theoretical Acoustics.* McGraw-Hill, Inc., New York, 1968.

[49] J. E. Gubernatis. Long-wave approximations for the scattering of elastic waves from flaws with applications to ellipsoidal voids and inclusions. *Journal of Applied Physics*, 50(4046), 1979.

[50] J. E. Gubernatis, E. Domany, J. A. Krumhansl, and M. Huberman. The Born approximation in the theory of the scattering of elastic waves by flaws. *Journal of Applied Physics*, 48, 1977.

[51] J. A. Ogilvy. Computer simulation of acoustic wave scattering from rough surfaces. *Journal of Physics D: Applied Physics*, 21(2):260–277, 1988.

[52] J. J. Bowman, T. Senior, and P. Uslenghi. *Electromagnetic and Acoustic Scattering by Simple Shapes.* North Holland, Amsterdam, 1969.

[53] J. A. Ogilvy. Theoretical comparison of ultrasonic signal amplitudes from smooth and rough defects. *NDT International*, 19(6):371–385, 1986.

[54] J. Zhang, B. Drinkwater, and P. Wilcox. Longitudinal wave scattering from rough crack-like defects. *IEEE Transactions on Ultrasonics, Ferroelectrics and Frequency Control*, 58(10):2171–2180, 2011.

[55] F. G. Bass and I. M. Fuks. Wave scattering from statistically rough surfaces. *Oxford Pergamon Press International Series on Natural Philosophy*, 93, 1979.

[56] E. I. Thorsos. The validity of the Kirchhoff approximation for rough surface scattering using a Gaussian roughness spectrum. *The Journal of the Acoustical Society of America*, 83(1):78, 1988.

[57] F. Shi, W. Choi, M. J.S. Lowe, E. A. Skelton, and R. V. Craster. The validity of Kirchhoff theory for scattering of elastic waves from rough surfaces. *Proceedings of the Royal Society A: Mathematical, Physical and Engineering Sciences*, 471(2178), 2015.

[58] J. D. Achenbach, A. K. Gautesen, and D. A. Mendelsohn. Ray Analysis of Surface-Wave Interaction with an Edge Crack. *IEEE Transactions on Sonics and Ultrasonics*, SU-27(3):124–129, 1980.

[59] J. D. Achenbach and A. N. Norris. Interference of corner reflected and edge diffracted signals for a surface breaking crack. *The Journal of the Acoustical Society of America*, 70(165), 1981.

[60] R .K. Chapman, J. E. Pearce, S. F. Burch, L. Fradkin, and M. W. Toft. Recent in-house developments in theoretical modelling of ultrasonic inspection. *Insight - Non-Destructive Testing and Condition Monitoring*, 49(2):93–97, 2007.

[61] J. H. Ferziger and M. Peric. *Computational Methods for Fluid Dynamics*. Springer, 3rd editio edition, 2002.

[62] C. L. Scandrett and J. D. Achenbach. Time-domain finite difference calculations for interaction of an ultrasonic wave with a surface-breaking crack. *Wave Motion*, 9(2):171–190, 1987.

[63] E. Dormy and A. Tarantola. Numerical simulation of elastic wave propagation using a finite volume method. *Journal of Geophysical Research*, 100:2123–2133, 1995.

[64] D. Beskos. Boundary element methods in dynamic analysis. *Applied Mechanics Reviews*, 40(1), 1987.

[65] D. Beskos. Boundary element methods in dynamic analysis: Part II (1986-1996). *Applied Mechanics Reviews*, 50(3), 1997.

[66] M. Kitahara, K. Nakagawa, and J. D. Achenbach. Boundary-integral equation method for elastodynamic scattering by a compact inhomogeneity. *Computational Mechanics*, 5(2-3):129–144, 1989.

[67] Younho Cho and Joseph L. Rose. A boundary element solution for a mode conversion study on the edge reflection of Lamb waves. *The Journal of the Acoustical Society of America*, 99(4):2097–2109, apr 1996.

[68] Y. Cho and J. L. Rose. An elastodynamic hybrid boundary element study for elastic guided wave interactions with a surface breaking defect. *International Journal of Solids and Structures*, 37(30):4103–4124, 2000.

[69] M. H. Aliabadi. *The Boundary Element Method, Applications in Solids and Structures*. John Wiley & Sons, 2002.

[70] L. E. Alsop and A. S. Goodman. Numerical model for propagation of Rayleigh waves around corners. *Eos, Transactions American Geophysical Union*, 53(4), 1972.

[71] W. D. Smith. The application of finite element analysis to body wave propagation problems. *Geophysical Journal International*, 42(2):747–768, 1975.

[72] R. J. Blake. *Numerical models for Rayleigh wave scattering from surface features*. PhD thesis, University of London (University College), 1988.

[73] Z. You and W. Lord. Finite element study of elastic wave interaction with cracks. *Review of Progress in Quantitative Nondestructive Evaluation*, 8:109–116, 1989.

[74] R. Ludwig and W. Lord. A finite element formulation for the study of ultrasonic NDT systems. *IEEE Transactions on Ultrasonics, Ferroelectrics and Frequency Control*, 35(6), 1987.

[75] R. Cook. *Finite Element Modelling For Stress Analysis*. Wiley, 1995.

[76] S. D. Gedney and U. Navsariwala. An unconditionally stable finite element time-domain solution of the vector wave equation. *IEEE Microwave and Guided Wave Letters*, 5(10):332–334, 1995.

[77] R. D. Cook, D. S. Malkus, and M. E. Plesha. *Concepts and applications of finite element analysis*. John Wiley and Sons, 1989.

[78] M. Frehner, S. M. Schmalholz, E. H. Saenger, and H. Steeb. Comparison of finite difference and finite element methods for simulating two-dimensional scattering of elastic waves. *Physics of the Earth and Planetary Interiors*, 171(1-4):112–121, 2008.

[79] P. Rajagopal, M. Drozdz, and M. J. S. Lowe. Towards improved finite element modelling of the interaction of elastic waves with complex defect geometries. *AIP Conference Proceedings*, 1096:49–56, 2009.

[80] P. Huthwaite. Accelerated finite element elastodynamic simulations using the GPU. *Journal of Computational Physics*, 257:687–707, 2014.

[81] P. Rajagopal, M. Drozdz, E. Skelton, M. J. S. Lowe, and R. V. Craster. On the use of absorbing layers to simulate the propagation of elastic waves in unbounded isotropic media using commercially available Finite Element packages. *NDT & E International*, 51:30–40, 2012.

[82] J. R. Pettit, A. Walker, P. Cawley, and M. J. S. Lowe. A Stiffness Reduction Method for efficient absorption of waves at boundaries for use in commercial Finite Element codes. *Ultrasonics*, 54(7):1868–79, 2014.

[83] G. A. Deschamps. Ray techniques in electromagnetics. *Proceedings of the IEEE*, 60(9):1022–1035, 1972.

[84] P. Calmon, A. Lhemery, I. Lecoeur-Taibi, R. Raillon, and L. Paradis. Models for the computation of ultrasonic fields and their interaction with defects in realistic NDT configurations. *Nuclear Engineering and Design*, 180(3):271–283, 1998.

[85] E. Becache, P. Joly, and C. Tsogka. Fictitious domains, mixed finite elements and perfectly matched layers for 2-D elastic wave propagation. 9(3):1175–1201, 2001.

[86] N. Gengembre. A Semi-Analytic-FEM Hybrid Model for Simulating UT Configurations Involving Complicated Interactions of Waves with Defects. *AIP Conference Proceedings*, 700(2004):74–80, 2004.

[87] J. Zhang, B. W. Drinkwater, and P. D. Wilcox. Defect characterization using an ultrasonic array to measure the scattering coefficient matrix. *IEEE Transactions on Ultrasonics, Ferroelectrics, and Frequency Control*, 55(10):2254–2265, 2008.

[88] J. Zhang, B. W. Drinkwater, and P. D. Wilcox. Effect of roughness on imaging and sizing rough crack-like defects using ultrasonic arrays. *IEEE Transactions on Ultrasonics, Ferroelectrics and Frequency Control*, 59(5):939–948, 2012.

[89] P. D. Wilcox and A. Velichko. Efficient frequency-domain finite element modeling of two-dimensional elastodynamic scattering. *The Journal of the Acoustical Society of America*, 127(1):155–65, 2010.

[90] L. W. Schmerr. *Fundamentals of Ultrasonic Nondestructive Evaluation*. Springer US, Boston, MA, 1998.

[91] L. Bai, A. Velichko, and B. W. Drinkwater. Ultrasonic characterization of crack-like defects using scattering matrix similarity metrics. *IEEE Transactions on Ultrasonics, Ferroelectrics, and Frequency Control*, 62(3):545–559, 2015.

[92] A. Velichko and P. D. Wilcox. Efficient finite element modeling of elastodynamic scattering with non-reflecting boundary conditions. *AIP Conference Proceedings*, 1430(31):142–149, 2012.

[93] A. Velichko and P. D. Wilcox. Efficient Finite Element Modeling of Elastodynamic Scattering From Near Surface and Surface-Breaking Defects. In *Review of Progress in Quantitative Nondestructive Evaluation*, volume 59, pages 59–66, 2011.

[94] M. V. Felice, A. Velichko, P. D. Wilcox, T. Barden, and T. Dunhill. Obtaining geometries of real cracks and using an efficient finite element method to simulate their ultrasonic array response. *Insight - Non-Destructive Testing and Condition Monitoring*, 56(9):492–498, 2014.

[95] W. Choi, E. A. Skelton, J. Pettit, M. J. S. Lowe, and R. V. Craster. A generic hybrid model for the simulation of three-dimensional bulk elastodynamics for use in nondestructive evaluation. *IEEE Transactions on Ultrasonics, Ferroelectrics, and Frequency Control*, 63(5):726–736, 2016.

[96] Prabhu Rajagopal and Elizabeth Skelton. Finite element based hybrid models for ultrasonic NDE using commercial packages. *Review of Quantitative Nondestructive Evaluation*, 29:1887–1894, 2010.

[97] W. Choi, E. Skelton, M. J.S. Lowe, R. Craster, and P. Rajagopal. Generic hybrid models for three-dimensional ultrasonic NDE. In *AIP Conference Proceedings*, volume 1430, pages 126–133. American Institute of Physics, may 2012.

[98] P. Rajagopal, E. Skelton, M. J. S. Lowe, R. Craster, and J. Russell. Generic time-domain hybrid models for ultrasonic NDE. In *Review of Progress in Quantitative Nondestructive Evaluation*, volume 67, pages 67–74, 2011.

[99] P. R. Stepanishen. The timedependent force and radiation impedance on a piston in a rigid infinite planar baffle. *The Journal of the Acoustical Society of America*, 49(3B):841–849, 1971.

[100] J. A. Jensen and N. B. Svendsen. Calculation of pressure fields from arbitrarily shaped, apodized, and excited ultrasound transducers. *IEEE Transactions on Ultrasonics, Ferroelectrics, and Frequency Control*, 39(2):262–267, 1992.

[101] A. Lhémery, P. Calmon, I. Lecœur-Taïbi, R. Raillon, and L. Paradis. Modeling tools for ultrasonic inspection of welds. *NDT and E International*, 33(7):499–513, 2000.

[102] D. Duxbury, J. Russell, and M. J. S. Lowe. The effect of variation in phased array element performance for Non-Destructive Evaluation (NDE). *Ultrasonics*, 53(6):1065–1078, 2013.

[103] T. P. Lerch, L. W. Schmerr, and A. Sedov. The wavefield of an ultrasonic angle beam shear wave transducer: an elastodynamic approach. In *Review of Progress in Quantitative Nondestructive Evaluation*, pages 885–892. Springer US, Boston, MA, 1997.

[104] A. Schuster. *An Introduction to the Theory of Optics*. London, E. Arnold, 1909.

[105] J. A. Johnson, N. M. Carlson, and D. M. Tow. Ray trace calculations of ultrasonic fields. *Research in Nondestructive Evaluation*, 3(1):27–39, 1991.

[106] David Duxbury. *Calibration and control of advanced ultrasonic array technology*. PhD thesis, Imperial College London, 2013.

[107] C. P. Griffice and J. A. Seydel. Spherical wave decomposition approach to ultrasonic field calculations. *Journal of Nondestructive Evaluation*, 2(3):241–247, 1981.

[108] O. Coutant, J. Virieux, and A. Zollo. Numerical source implementation in a 2D finite difference scheme for wave propagation. *Bulletin of the Seismological Society of America*, 85(5):1507–1512, 1995.

[109] T. Teng and T. Kuo. Finite Element Source Simulation for Elastodynamics. *Inverse modeling in exploration geophysics : proceedings of the 6th International Mathematical Geophysics Seminar*, pages 277–298, 1988.

[110] P. Renteln. *Manifold Tensors and Forms An Introduction for Mathematicians and Physicists*. Cambridge University Press, 214.

[111] B. D. Steinberg. Digital beamforming in ultrasound. *IEEE Transactions on Ultrasonics, Ferroelectrics, and Frequency Control*, 39(6):716–721, 1992.

[112] P. Calmon, S. Mahaut, S. Chatillon, and R Raillon. CIVA: an expertise platform for simulation and processing NDT data. *Ultrasonics*, 44:975–979, 2006.

[113] BS EN 12668-2:2010 Non-destructive testing Characterization and verification of ultrasonic examination equipment Part 2: Probes, 2010.

[114] BS EN ISO 16827:2014 Non-destructive testing Ultrasonic Testing Characterisation and sizing of discontinuities, 2014.

[115] J. Dobson, A. Tweedie, G. Harvey, R. O'Leary, A. Mulholland, K. Tant, and A. Gachagan. Finite element analysis simulations for ultrasonic array NDE inspections. In *AIP Conference Proceedings*, volume 1706, page 040005. AIP Publishing LLC, 2016.

[116] W. Ke, M. Castaings, and C. Bacon. 3D finite element simulations of an air-coupled ultrasonic NDT system. *NDT & E International*, 42(6):524–533, 2009.

[117] J. Pettit, A. E. Walker, and M. J.S. Lowe. Improved detection of rough defects for ultrasonic nondestructive evaluation inspections based on finite element modeling of elastic wave scattering. *IEEE Transactions on Ultrasonics, Ferroelectrics, and Frequency Control*, 62(10):1797–1808, 2015.

[118] W. Choi, E. A. Skelton, F. Shi, M. J. S. Lowe, and R. V. Craster. Rough surface reconstruction for ultrasonic NDE simulation. In *AIP Conference Proceedings*, volume 1581, pages 587–594. American Institute of Physics, 2014.

[119] W. Choi, E. Skelton, M. J. S. Lowe, and R. Craster. Unit cell finite element modelling for ultrasonic scattering from periodic surfaces. In *AIP Conference Proceedings*, volume 1511, pages 83–90. American Institute of Physics, 2013.

[120] J. Dobson and P. Cawley. The scattering of torsional guided waves from Gaussian rough surfaces in pipework. *The Journal of the Acoustical Society of America*, 141(3):1852–1861, 2017.

[121] A. Fissolo, S. Amiable, O. Ancelet, F. Mermaz, J. M. Stelmaszyk, A. Constantinescu, C. Robertson, L. Vincent, V. Maillot, and F. Bouchet. Crack initiation under thermal fatigue: An overview of CEA experience. Part I: Thermal fatigue appears to be more damaging than uniaxial isothermal fatigue. *International Journal of Fatigue*, 31(3):587–600, 2009.

[122] M. F. Cipière and J. A. Le Duff. Thermal fatigue experience in French piping: Influence of surface condition and weld local geometry. *Welding in the World*, 46(1-2):23–27, 2002.

[123] D. A. Spera. What is Thermal Fatigue? In *Thermal Fatigue of Materials and Components*, Pennsylvania, 1976. ASTM International.

[124] S. Carmignato, W. Dewulf, and R. Leach. *Industrial X-ray computed tomography*. Springer International Publishing, Cham, Switzerland, 2017.

[125] L. W Goldman. Principles of CT and CT Technology. *Journal of Nuclear Medicine Technology*, 35(3):115–128, 2007.

[126] E. C. Jameson. *Electrical Discharge Machining*. Society of Manufacturing Engineers, Machining Technology Association, 2001.

[127] C. Tomasi and R. Manduchi. Bilateral filtering for gray and color images. In *Sixth International Conference on Computer Vision*, pages 839–846. Narosa Publishing House, 1998.

[128] S. Birchfield. *Image Processing and Analysis*. Cengage Learning, 2016.

[129] F. Meyer. Topographic distance and watershed lines. *Signal Processing*, 38(1):113–125, 1994.

[130] A. Boström and G. Wickham. On the boundary conditions for ultrasonic transmission by partially closed cracks. *Journal of Nondestructive Evaluation*, 10(4):139–149, 1991.

[131] P. G. Young, T. B. H Beresford-West, S. R. L Coward, B. Notarberardino, B. Walker, and A. Abdul-Aziz. An efficient approach to converting three-dimensional image data into highly accurate computational models. *Philosophical Transactions of the Royal Society A: Mathematical, Physical and Engineering Sciences*, 366(1878):3155–3173, 2008.

[132] J. H. Keyak, J. M. Meagher, H. B. Skinner, and C. D. Mote. Automated three-dimensional finite element modelling of bone: a new method. *Journal of Biomedical Engineering*, 12(5):389–397, 1990.

[133] R. Müller and P. Rüegsegger. Three-dimensional finite element modelling of non-invasively assessed trabecular bone structures. *Medical Engineering and Physics*, 17(2):126–133, 1995.

[134] W. E. Lorensen and H. E. Cline. Marching cubes: A high resolution 3D surface construction algorithm. In *Proceedings of the 14th annual conference on Computer graphics and interactive techniques - SIGGRAPH '87*, volume 21, pages 163–169, New York, New York, USA, 1987. ACM Press.

[135] R. K. Chapman and M. W. Toft. Handbook of evidence on NDT capability, chapter 3 ultrasonic inspection: responses from single smooth defects. Technical report, Nuclear Electric, 1993.

[136] D. Firth and R. F. Gould. A hybrid finite difference/helmholtz integral scheme for ultrasonic scattering. *Journal of Nondestructive Evaluation*, 9(2-3):167–179, 1990.

[137] I. N. Ermolov. The reflection of ultrasonic waves from targets of simple geometry. *Non-Destructive Testing*, 5(2):87–91, 1972.

List of Publications

[P1] R. Phillips, D. Duxbury, P. Huthwaite and M. Lowe. Simulating the Ultrasonic Scattering from Complex Surface-breaking Defects using a Three Dimensional Hybrid Model, *NDT&E International*, vol. 97, pp. 32-41, July 2018.

[P2] R. Phillips, D. Duxbury, P. Huthwaite and M. Lowe. Efficient Three Dimensional Simulation of the Ultrasonic Scattering from Fatigue Defects using X-ray Computed Tomography Data, *In preparation*.